ISTANBUL TECHNICAL UNIVERSITY ★ GRADUATE SCHOOL

SENSORLESS SPEED CONTROL OF A PM ASSISTED SYNCHRONOUS RELUCTANCE MOTOR FROM ZERO TO RATED SPEED

M.Sc. THESIS

Kadir AKGÜL

Department of Electrical Engineering

Electrical Engineering Programme

JULY 2023

ISTANBUL TECHNICAL UNIVERSITY ★ GRADUATE SCHOOL

SENSORLESS SPEED CONTROL OF A PM ASSISTED SYNCHRONOUS RELUCTANCE MOTOR FROM ZERO TO RATED SPEED

M.Sc. THESIS

Kadir AKGÜL
(504191077)

Department of Electrical Engineering

Electrical Engineering Programme

Thesis Advisor: Prof. Dr. Lale Tükenmez ERGENE

JULY 2023

ISTANBUL TEKNİK ÜNİVERSİTESİ ★ LİSANSÜSTÜ EĞİTİM ENSTİTÜSÜ

DM DESTEKLİ BİR SENKRON RELÜKTANS MOTORUN SIFIRDAN ANMA HIZINA KADAR ALGILAYICISIZ HIZ KONTROLÜ

YÜKSEK LİSANS TEZİ

Kadir AKGÜL
(504191077)

Elektrik Mühendisliği Anabilim Dalı

Elektrik Mühendisliği Programı

Tez Danışmanı: Prof. Dr. Lale Tükenmez ERGENE

TEMMUZ 2023

Kadir AKGÜL, a M.Sc. student of ITU Graduate School student ID 504191077, successfully defended the thesis entitled "SENSORLESS SPEED CONTROL OF A PM ASSISTED SYNCHRONOUS RELUCTANCE MOTOR FROM ZERO TO RATED SPEED", which he prepared after fulfilling the requirements specified in the associated legislations, before the jury whose signatures are below.

Thesis Advisor : **Prof. Dr. Lale Tükenmez ERGENE** ....
Istanbul Technical University

Jury Members : **Assoc. Prof. Dr. Murat YLMAZ** ....
Istanbul Technical University

Prof. Dr. Mehmet Timur AYDEMİR ....
Kadir Has University

Date of Submission : 26 May 2023
Date of Defense : 05 July 2023

To the people I value,

FOREWORD

This thesis and the research behind it would not have been possible without the support of my supervisor, Prof. Dr. Lale Tükenmez ERGENE. Her knowledge, motivation, and exacting attention to detail have been an inspiration of the planning and development of this thesis and kept my work on track.

I also would like to thank to Assoc. Prof. Dr. Murat YILMAZ and Assoc. Prof. Dr. Ali Fuat ERGENÇ for their valuable and constructive suggestions during the project meetings. Their willingness to give their time so generously has been greatly appreciated.

I would also like to thank my dear colleagues at Computational Electromechanical Systems Research Laboratory (CEMSys Lab.), especially Res. Asst. Turan Alp SARIKAYA, Electrical Engineer Alper TAP, M.Sc., and Electrical Engineer Caner KOREL whom I sweated and worked together with countless hours during our project work.

And I would like to express my deepest gratitude to my family, my brother Bilal Berke AKGÜL, my mother Şükran AKGÜL, and my father Ebuzer AKGÜL for their unwavering support and trust throughout my life.

This thesis work is a part of TÜBİTAK 1001 project which has grant number 120E375. I would also like to thank the Scientific and Technological Research Council of Turkey (TÜBİTAK) for their support of this project.

This project is also supported by the ITU BAP unit as the MYL-2021-43142 project. I would like to thank the ITU BAP unit for their support.

July 2023

Kadir AKGÜL
(Electrical and Control Engineer)

TABLE OF CONTENTS

Page

ABBREVIATIONS

ALA	: Axially Laminated Anisotropic
EMF	: Electromotive Force
EEMF	: Extended Electromotive Force
FOC	: Field-Oriented Control
HF	: High-Frequency
HFI	: High-Frequency Injection
HFCI	: High-Frequency Current Injection
HFVI	: High-Frequency Voltage Injection
IM	: Induction Motor
IPMSM	: Interior Permanent Magnet Synchronous Motor
MTPA	: Maximum Torque Per Ampere
PMaSynRM	: Permanent Magnet-Assisted Reluctance Motor
PMSM	: Permanent Magnet Synchronous Motor
PLL	: Phase-Lock Loop
PWM	: Pulse-Width Modulation
SMO	: Sliding Mode Observer
SNR	: Signal to Noise Ratio
SVPWM	: Space Vector Pulse-Width Modulation
SynRM	: Synchronous Reluctance Motor
THD	: Total Harmonic Distortion
TLA	: Transversally Laminated Anisotropic

SYMBOLS

DAC	: Digital-analog converter
$\mathbf{d_d}$	: Duty cycle of d-axis voltage
$\mathbf{d_n}$	: Duty cycle of n^{th} adjacent voltage space vector
$\mathbf{d_q}$	: Duty cycle of q-axis voltage
$\mathbf{e_{ext}}$	: Amplitude of EEMF components
$\mathbf{e_\alpha}$	: EEMF α-axis component
$\mathbf{e_\beta}$	: EEMF β-axis component
$\mathbf{f_0}$	: Centre frequency of band-pass filter
$\mathbf{f_g}$	: Bandwidth frequency of band-pass filter
$\mathbf{f_{hf}}$	: HFI components frequency
$\mathbf{f_{sw}}$	: Switching frequency
I	: Identity matrix
$\mathbf{I_{i0}}$	: Positive sequence component of HF currents
$\mathbf{I_{i1}}$	: Negative sequence component of HF currents
$\mathbf{i_{dc}}$	: d-axis iron losses current
$\mathbf{i_{dm}}$	: d-axis magnetizing current
$\mathbf{i_{dm_{ref}}}$	: Reference d-axis current
$\mathbf{i_{ds}}$	: d-axis stator current
$\mathbf{i_{qc}}$	: q-axis iron losses current
$\mathbf{i_{qm}}$	: q-axis magnetizing current
$\mathbf{i_{qm_{ref}}}$	: Reference q-axis current
$\mathbf{i_{qs}}$	: q-axis stator current
$\mathbf{i_{sm}}$	: Magnetizing stator current
$\mathbf{i_{\alpha m}}$	: Thevenin α-axis stator current
$\mathbf{i_{\beta m}}$	: Thevenin β-axis stator current
$\mathbf{K_{slide}}$	: Sliding-mode observer gain
$\mathbf{L_0}$	: Average inductance
$\mathbf{L_1}$	: Difference inductance
$\mathbf{L_d}$	: d-axis inductance
$\mathbf{L_q}$	: q-axis inductance

$\mathbf{L(\theta_e)}$	: Inductance matrix
m	: Modulation index
n	: Sector number of space vector plane
p	: Pole pair numbers
$\mathbf{R_c}$	: Iron losses resistance
$\mathbf{R_s}$	: Stator resistance
$\mathbf{R_t}$	: Thevenin resistance
$\mathbf{S_n}$	: n^{th} switching state
s	: Laplace operator
$\mathbf{T_e}$	: Induced torque of motor
$\mathbf{T_{e_{ref}}}$	: Reference induced torque
$\mathbf{T_n}$	: Switching timing of n^{th} voltage space vector
$\mathbf{T_s}$	: Switching period
t	: Time
$\mathbf{U_{s_{ph}}}$	: Stator phase voltage
$\mathbf{u_{ds}}$	: d-axis stator voltage
$\mathbf{u_{dt}}$	: Thevenin d-axis stator voltage
$\mathbf{u_{qs}}$	: q-axis stator voltage
$\mathbf{u_{qt}}$	: Thevenin q-axis stator voltage
$\mathbf{u_{\alpha t}}$	: Thevenin α-axis stator voltage
$\mathbf{u_{\beta t}}$	: Thevenin β-axis stator voltage
$\mathbf{V_{DC}}$	: DC bus voltage
$\mathbf{V_{hf}}$	: Amplitude value of HFI voltages
$\mathbf{V_n}$	: n^{th} voltage space vector
$\mathbf{V_{ref}}$	: Reference voltage amplitude
$\mathbf{x^{hf}}$	: High-frequency parameter
$\mathbf{x^{lf}}$	: Low-frequency parameter
$\hat{\mathbf{x}}$	: Estimated parameter
$\Delta\hat{\boldsymbol{\theta}}_e$	: Position estimation error
$\boldsymbol{\delta_s}$	: Load angle
$\boldsymbol{\varepsilon_{\theta_{sin}}}$	: Sine expression of position estimation error
$\boldsymbol{\theta}$	: The angle of reference voltage vector
$\boldsymbol{\theta_e}$	: Rotor electrical position
$\boldsymbol{\kappa}$	: Current angle
$\boldsymbol{\lambda_{dm}}$	: d-axis flux linkage

λ_{pm}	: Flux linkage of permanent magnet
λ_{qm}	: q-axis flux linkage
λ_s	: Stator flux linkage
ω_e	: Electrical angular speed of motor
ω_h	: Angular frequency of high-frequency components
ω_m	: Mechanical angular speed of motor
ω_s	: Stator angular frequency

LIST OF TABLES

LIST OF FIGURES

Page

SENSORLESS SPEED CONTROL OF A PM ASSISTED SYNCHRONOUS RELUCTANCE MOTOR FROM ZERO TO RATED SPEED

SUMMARY

Recently, permanent magnet synchronous motors (PMSMs) with high-energy magnets are proposed to replace the variable speed drives of some induction motors (IMs) to increase power factor and efficiency. However, the high price of high-energy rare earth permanent magnets, especially for applications with upfront cost constraints, calls into question this solution. Permanent magnet assisted synchronous reluctance motor (PMaSynRM), which has a high-efficiency standard and high torque and power density, where rare earth magnets' usage is not preferred, is expected to replace IMs, which is currently the most used motor type. In this study, a PMaSynRM designed for a washing-machine appliance is used to apply a sensorless speed control approach from zero speed to rated speed.

The working principle of PMaSynRM is based on the reluctance torque beside the electromagnetic torque. The dominant one is the reluctance torque, and this is the subject where it differs from an interior permanent magnet synchronous motor (IPMSM). In a PMaSynRM, the reluctance torque is provided by rotor air barriers and the electromagnetic torque is provided by permanent magnets placed on the q-axis of the rotor. The mathematical model of PMaSynRM can be derived simply in the rotating reference frame according to rotor. The variables and parameters of stator axes are transformed into the d&q reference frame by using the Clarke and Park reference frame transformations.

Amplitude and angle of stator current vector are controlled separately by performing field-oriented control (FOC). Different control strategies are implied to the motor applications in literature taking advantage of FOC. The main one for a PMaSynRM is maximum torque per ampere (MTPA) control because of its simplicity. Another advantage is that the output power is also maximized for a specific speed value besides the output torque. Thus, the motor torque and power density are increased.

A two-level inverter is sufficient for a three-phase PMaSynRM driver. The amplitudes and frequencies of phase voltages and currents are adjusted to the desired value by using inverter and FOC technique together. The space vector pulse-width modulation (SVPWM) technique becomes prominent among pulse-width modulation (PWM) techniques for inverters.

Sensorless control is based on obtaining the rotor position and speed information not from the position sensor. In this study, the extended electromotive force (EEMF) and high-frequency injection (HFI) models are preferred. The HFI model is applied below a certain speed due to the inadequacy of the EEMF model at lower and zero speeds.

In the first step, the PMaSynRM state space model includes EEMF components is obtained on the α&β stationary reference frame. The EEMF components containing rotor position information cannot be obtained directly by measurement. Therefore, EEMF components need to be estimated using an observer structure. In this study, the

sliding-mode observer (SMO) structure is used. The estimation errors of α&β-axis currents are used for estimating EEMF components.

As a result of simulations, sensorless speed control of PMaSynRM is realized from 300 to 3000 rpm (rated) and also under rated load conditions. For rated speed where efficiency is high and critical, the electrical position estimation error is around 2°, which is acceptable.

In the second stage, the HFI technique is applied for the PMaSynRM. High-frequency voltage injection (HFVI) is preferred, since the injected signals are not regulated by the current controllers. As a result of the injected high-frequency voltages, high-frequency signals are formed in the phase currents of the motor. These current signals contain rotor position information. However, the signals must be subjected to some signal processing to obtain this rotor position information. These signals are separated from the motor fundamental current, and position information. A smoother position information is provided with the designed phase-locked loop (PLL) technique.

In simulation environment, PMaSynRM sensorless speed control is carried out from zero to 300 rpm speed. In addition, sensorless speed control is also provided for the rated load condition. As a result, the electrical position error is less than 2° for the entire speed range, which is reasonable level for a sensorless operation.

In the final stage, the experiments of sensorless control of PMaSynRM are carried out. With the EEMF technique, both rotor position and speed are successfully estimated and the motor is driven from 300 rpm to rated speed. The noise of estimations increases at low speeds because of lower values of EEMF components as expected. For lower speeds, the HFVI technique is tested. The motor is driven under rated load at 30 rpm. Then, the 100 rpm step responses of motor are obtained under rated load. Finally, the motor is tested to be rotated in the opposite direction.

With the designed speed control algorithm, PMaSynRM is provided to operate sensorless from zero speed to rated speed. The efficiency value obtained with the sensor is approximately kept, thus avoiding the concern of efficiency loss.

DAİMİ MIKNATIS DESTEKLİ SENKRON RELÜKTANS MOTORUN SIFIRDAN ANMA HIZINA KADAR ALGILAYICISIZ HIZ KONTROLÜ

ÖZET

Sabit olmayan yük altındaki elektrik motoru tahriklerinde verimi artırmak ve enerji tasarrufu sağlamak için değişken hızlı tahrikler gereklidir. Son yıllarda yüksek enerjili mıknatıslara sahip daimi mıknatıslı senkron motorlar (DMSM, ing: PMSM), güç faktörü ve verim avantajlarından dolayı piyasada asenkron motorların değişken hızlı tahriklerine bir alternatif olmaktadırlar. Fakat yüksek enerjiye sahip nadir toprak elementli daimi mıknatısların yüksek fiyatı, özellikle ön maliyet kısıtlamaları bulunan uygulamalar için çözüm olmamaktadır. Nadir toprak elementi mıknatısların kullanılmasının tercih edilmediği ve aynı zamanda yüksek verim, çıkış momenti ve güç yoğunluğuna sahip daimi mıknatıs destekli senkron relüktans motorlar (DMDSRM, ing: PMaSynRM), hâlihazırda en çok kullanılan motor olan asenkron motora güçlü alternatif olarak karşımıza çıkmaktadır. Bu çalışmada, çamaşır makinesi uygulaması için tasarlanmış olan bir DMDSRM kullanılmıştır. Seçilen bu DMDSRM'nin sıfır hızdan anma hızına kadar algılayıcısız hız kontrolünün gerçekleştirilmesi amaçlanmıştır.

DMDSRM tarafından hem relüktans momenti hem de elektromanyetik moment üretilebilmektedir. Bu momentlerden daha baskın olanı relüktans momentidir ve bu özelliği ile gömülü mıknatıslı senkron motorlardan (GMSM, ing: IPMSM) ayrışmaktadır. Relüktans momenti, manyetik olarak anizotropik olan bir manyetik malzemenin manyetik alan yönünde hizalanma eğiliminden meydana gelmektedir. DMDSRM'de bu anizotropiklik rotorda oluşturulan akı bariyerleri ile sağlanmaktadır. Elektromanyetik moment ise geleneksel motorlardan da bilindiği üzere stator ve rotorun oluşturduğu iki manyetik alanın etkileşiminden meydana gelmektedir. DMDSRM'de bu moment rotor q-eksenine yerleştirilen daimi mıknatıslar ile sağlanmaktadır. Böylece toplam momente artış sağlanırken ayrıca güç faktöründe de iyileşme elde edilir. DMDSRM'nin matematiksel modeli, en sade şekli ile rotor referans eksen takımında çıkarılmaktadır. Bunun için stator büyüklükleri ve parametreleri, Clarke ve Park dönüşümleri ile d&q eksen takımı üzerine indirgenirler. Elde edilen elektriksel dinamik denklemler kullanılarak d-ekseni ve q-ekseni olarak iki ayrı eşdeğer devre oluşturulabilir. Ayrıca bakır kayıplarının yanında demir kayıpları da göz önüne alındığında eşdeğer devrelere demir kayıplarına karşılık gelen paralel bir direnç eklenir. Son olarak eşdeğer devrelerin Thevenin eşdeğerleri alınarak devreler daha basit hale getirilirler.

DMDSRM için alan yönlendirmeli kontrol (AYK, ing: FOC) uygulanarak stator akımı genliği ve açısı ayrı ayrı kontrol edilebilmektedir. Bu yüzden AYK, vektör kontrolü olarak da isimlendirilmektedir. AYK tekniği ile motor için oluşturulmuş kontrol stratejileri gerçekleştirilebilir. DMDSRM'ye uygulanan başlıca kontrol stratejileri akım başına maksimum moment (ABMM, ing: MTPA) kontrolü, en hızlı moment cevabı kontrolü, maksimum güç faktörü kontrolü ve maksimum verim kontrolüdür. Bu çalışmada, sağladığı birtakım avantajlarından dolayı ABMM kontrolü kullanılmıştır. Bu yöntem öncelikle basit olan algoritması ile öne çıkmaktadır. Diğer bir avantajı ise ABMM kontrolü ile motorun bir hız değeri için motorun çıkış momentinin yanında çıkış gücünün de mümkün olan en yüksek değeri elde edilmektedir. Böylece motor tasarımı değiştirilmeden motorun moment ve güç yoğunluğu arttırılır. Bu avantajlarından dolayı ABMM kontrolü endüstride de yaygın olarak tercih edilmektedir.

Üç fazlı bir DMDSRM sürücüsü için iki seviyeli bir evirici yeterli olmaktadır. Evirici sayesinde istenilen genlikte ve frekansta motor faz gerilimleri oluşturulabilmektedir. Dolayısıyla AYK tekniği kullanımı ile de motor faz akımları genlikleri ve frekansları da kontrol edilebilir. Eviricide doğru akım (DA) gerilimden sinüzoidal alternatif akım (AA) gerilimlerin üretilmesi için çeşitli darbe genişlik modülasyonu (DGM, ing: PWM) teknikleri geliştirilmiştir. Bu teknikler arasında uzay vektör DGM (UVDGM, ing: SVPWM) tekniği öne çıkmaktadır. UVDGM tekniği ile DA bara tarafından sağlanan kazanç yükseltilir. Ayrıca daha az anahtarlama gerçekleştirilerek hem anahtarlama kayıpları azaltılıp sistem verimde artış sağlanır hem de toplam harmonik bozunum (THB, ing: THD) azaltılır. UVDGM tekniği gerilim-zaman dengesi prensibine dayanmaktadır. Bu prensipten yararlanılarak üretilmek istenen referans gerilim vektörü, uzay vektör düzleminde bu vektöre komşu iki anahtarlama gerilim vektörü ile elde edilir.

Algılayıcısız kontrol, vektör kontrolünde gerekli olan konum bilgisinin ve kapalı çevrim hız kontrolünde gerekli olan hız bilgisinin konum algılayıcısından alınmayıp çeşitli teknikler ile elde edilmesine dayanmaktadır. Son yıllarda algılayıcısız kontrol, endüstriyel uygulamalarda oldukça popüler hale gelmiştir. Algılayıcının sistemden çıkarılması ile daha düşük sistem maliyeti, azaltılmış donanım karmaşıklığı ve boyutu, kontrol sisteminin güvenilirliğinde artış ve sistem bakım gereksiniminde azalma sağlanır. Bu çalışmada algılayıcısız kontrol yöntemlerinden genişletilmiş elektromotor kuvveti (GEMK, ing: EEMF) tekniği ve yüksek frekans enjeksiyonu (YFE, ing: HFI) tekniği tercih edilmiştir. Bu algılayıcısız kontrol tekniklerinin kullanılması ile motorun rotor konumu ve hızı kestirilebilmektedir. Düşük ve sıfır hızlarda GEMK modelinin yetersiz kalması nedeniyle belli bir hız değerinin altında yüksek frekans enjeksiyonu tekniğine başvurulmaktadır.

Çalışmanın ilk aşamada GEMK tekniği ele alındı. GEMK tekniğinin uygulanması için öncelikle motorun α&β durağan eksen takımındaki GEMK bileşenlerini içeren durum uzay modeli elde edilir. Rotor konum bilgisini içeren bu GEMK bileşenleri ölçüm yolu ile doğrudan elde edilememektedirler. Bu yüzden GEMK bileşenlerinin bir gözleyici yapısı kullanılarak kestirilmeleri gerekmektedir. Bu kestirim işlemi için literatürde çeşitli gözleyici yapıları bulunmaktadır. Bu çalışmada hızlı yanıt vermesi, kararlı yapısı ve kolay uygulanması gibi avantajlarından dolayı kayan kipli gözleyici (KKG, ing: SMO) yapısı kullanılmıştır. Oluşturulan KKG'li durum uzay modelinde, α&β-ekseni akımlarının kestirim hataları kullanılarak GEMK bileşenleri kestirimleri gerçekleştirilir. Bir KKG katsayısı ile çarpılan bu akım kestirim hatalarının işaretleri GEMK bileşenlerini oluştururlar.

Yapılan benzetişimler sonucunda DMDSRM'nin algılayıcısız hız kontrolü 300 rpm'den anma hızı olan 3000 rpm'e kadar gerçekleştirildi. Ayrıca motorun anma yük değerinde yüklendiği durumlar için de algılayıcısız kontrol başarıldı. Verimin yüksek ve kritik olduğu anma hızı için elektriksel konum kestirim hatası 2° civarındadır ve bu değer kabul edilebilir sınırlar içindedir.

İkinci aşamada ise DMDSRM için YFE tekniği ele alınmıştır. Bu teknik, akım enjeksiyonu ve gerilim enjeksiyonu olmak üzere ikiye ayrılmaktadır. Yüksek frekanslı akım enjeksiyonu (YFAE, ing: HFCI) yerine sağladığı avantajlardan dolayı bu çalışmada yüksek frekanslı gerilim enjeksiyonu (YFGE, ing: HFVI) tekniği tercih edilmiştir. Gerilim enjeksiyonunda enjekte edilecek yüksek frekanslı işaretler akım kontrolörleri tarafından ayar edilmezler. Ayrıca yüksek frekanslı işaretlerin genlik ve frekans seçiminde akım kontrolörleri tarafından bir kısıtlama yoktur. Kullanılan tekniklerdeki başka bir ayrım ise, yüksek frekanslı işaretlerin darbeli veya dönen gerilim şeklinde olması noktasındadır. Bu çalışmada dönen gerilim enjeksiyonu tercih edilmiştir. Darbeli enjeksiyon yöntemi, rotor konum bilgisini gerektiren dönen referans eksen takımında gerçekleştirilir. Bu nedenle, bu yöntem doğrudan konum tahmini başarımına bağlıdır. Bu tekniğin diğer bir dezavantajı ise motor parametrelerine bağlı olmasıdır.

YFGE algılayıcısız kontrol tekniğinde enjekte edilen yüksek frekanslı gerilimler sonucunda motorun faz akımlarında yüksek frekanslı işaretler oluşmaktadır. Bu akım işaretleri rotor konum bilgisini içermektedirler. Fakat bu işaretlerin motor temel akım bileşeninden ayrıştırılarak konum bilgisinin alınabilecek hale getirilmesi gerekmektedir. Ek olarak faz-kilitlemeli çevrim (FKÇ, ing: PLL) yöntemine başvurularak daha düzgün bir konum bilgisi alınması sağlanır.

DMDSRM’nin YFGE uygulaması için oluşturulan benzetim modelinde sıfır hızdan GEMK tekniğine geçilen 300 rpm hız değerine kadar algılayıcısız hız kontrolü gerçekleştirilmiştir. Ayrıca, motorun anma yük değeri altında da algılayıcısız hız kontrolü sağlanmıştır. Sonuç olarak, elektriksel konum kestirim hatası tüm hız aralığı için 2°’den düşüktür. 2°’lik hata verim açısından 50 rpm için %0,04 ve 300 rpm için %0,56'ya karşılık gelmektedir. Bu verim değerleri düşük hızlardaki algılayıcısız çalışma için kabul edilebilir seviyelerdedir.

Son aşamada, PMaSynRM'nin algılayıcısız kontrolü deneysel ortamda test edildi. GEMK tekniği ile hem rotor konumu hem de hızı başarılı bir şekilde kestirildi ve motor 300 rpm hız değerinden anma hızına kadar sürüldü. Beklendiği gibi düşük hızlarda EEMF bileşenlerinin düşük değerleri nedeniyle, kestirimler üzerindeki gürültü artmıştır. Daha düşük hızlardaki çalışma için YFGE tekniği test edildi. Motor, 30 rpm hız değerinde ve nominal yük altında sürülmesi başarıldı. Daha sonra, motorun anma yükü altında 100 rpm değerindeki basamak cevapları test edildi. Son olarak algoritmada herhangi bir ayarlama yapılmadan motorun ters yönde döndürülmesi sağlandı.

Çalışmanın sonucunda tasarlanan hız kontrolü algoritması ile DMDSRM’nin sıfır hızdan anma hızına kadar algılayıcısız bir şekilde çalışması sağlanmıştır. Aynı zamanda algılayıcılı kontrol durumunda elde edilen verim değeri yaklaşık olarak korunmuştur.

1. INTRODUCTION

1.1 Purpose of Thesis

First of all, the purpose of the thesis is to raise awareness for permanent magnet assisted synchronous reluctance motor (PMaSynRM), which is advantageous in terms of cost and competitive in terms of efficiency. In addition, to create an easy-to-apply algorithm using a closed-loop sensorless speed control for a certain speed range is another purpose of the thesis.

1.2 Literature Review

Even though there are many resources for sensorless control of synchronous reluctance motor (SynRM) and permanent magnet synchronous motor (PMSM), the resources about the sensorless control of a PMaSynRM in the literature are limited. The techniques applied to SynRMs and PMSMs can be applied to PMaSynRMs with some modifications. Because, the only difference of PMaSynRM from SynRM is the electromotive force (EMF) voltage caused by the magnet flux on the d-axis if we consider the mathematical models. Also, the difference of interior permanent magnet synchronous motor (IPMSM) from PMaSynRM is that only the magnet flux EMF voltage is on the q-axis [1]. Therefore, a literature review is also carried out for studies on PMSMs and SynRMs.

Sensorless control methods are divided into two categories for medium to high speed and zero to low speed. These two categories have different needs for observer design. In general, in medium to high-speed range model-based observers perform well as there is a good signal-to-noise ratio and measured variables are high enough to excite the observer. One drawback of these methods is sensitivity to parameter variations or uncertainties. For the zero to low-speed region, since the exciting features of the measured electrical variables are low due to low speed, combined with the measurement noise, model-based observers do not perform very well. For this speed region, additional identifying signal injection is often required. This signal injection is in the form of either voltages or currents [2]. Response to these injected signals often contains the position information of the anisotropic rotor. With a proper demodulation rotor position provided that the response to the injected signals is sufficient in the sense of amplitude and signal to noise ratio (SNR) [3]. Because of these reasons, two methods are commonly combined to account for the whole speed range [4].

In literature, the sensorless control techniques for medium and high speeds can be listed as estimation of the rotor position by using the fundamental components of the motor phase variables [5-9], the voltage/current difference [10-13], high-frequency signal injection [14-17], a specific form of inverter switching [18], triple harmonics caused by motor design [19], and so on. Sensorless control schemes based on the fundamental components are preferred because of the disadvantage of sensor noises at higher frequencies.

Extended flux or extended EMF models of the motor at fundamental frequency are commonly used for sensorless control of motors operating at medium and high speeds. In these methods, different d&q-axis reluctances of IPMSM and reluctance motors are utilized due to the magnetically anisotropic rotor [20]. Extended flux or extended EMF components of the model in the α&β stationary reference frame contain rotor position information. It is possible to make position and speed estimations with these components obtained by an observer method [21].

Position estimation can be realized by using extended flux models created through the motor torque equation based on the same principle as Hasegawa and Matsui (2008) and Shinke and et al. (2009) [22, 23]. Zang and Zhou (2016) carried out sensorless control of PMaSynRM with using equivalent EMF model and SMO [24]. When, Chen and et al. (2003) studied sensorless control of IPMSM with using extended EMF model and disturbance observer [21], Liu and et al. (2011) used SMO as observer [25]. Scalcon and et al. (2019) and Ichikawa and et al. (2007) used a Luenberger observer for same extended EMF model principle in sensorless control of SynRM [26, 27]. Since the motor models created for sensorless control can be derived from each other, their performance will be similar. The success of chosen observer becomes a more decisive factor in this regard.

Various types of observers are used by researchers for rotor position estimation such as the Luenberger observer [26, 27], the sliding-mode observers [28-34], and adaptive observer structures [33, 35]. There are many studies on SMOs particularly in the literature for the sensorless control of electric motors because of their robust structure, fast convergence, low sensitivity to disturbance and parameter variations [28-30]. In this study, it is not vital to use adaptive observer which has more complex structure since the drive process is carried out up to the rated speed of motor [36].

The position and speed estimations become difficult at low speeds since flux and EMF values are directly proportional to speed [20]. Therefore, other techniques such as high-frequency injection (HFI) method are preferred as sensorless control at low speeds and zero speed. Zero and low speed position sensorless operation of the electric machine has always been an active field of study, especially within competitive markets where cost reduction is an important driving factor. The literature is teeming with methods such as signal injection methods, third harmonic observers, zero crossing detection algorithms, current rate of change (switching transient) algorithms [37] some of them being parameter dependent and some of them are parameter free. Parameter independency is also another important aspect of the position estimation methods as parameters might be uncertain at extremum operating points such as very light and very heavy loads for highly nonlinear machines like SynRMs or machines with heavy slotting effects and concentrated windings.

Injected signals are either voltages or currents hence the names high-frequency voltage injection (HFVI) and high-frequency current injection (HFCI). HFVI is straightforward since no additional hardware to a conventional field-oriented control (FOC) scheme is required. In HFVI, high-frequency components of suitable magnitude and frequency are superimposed on the current controller outputs. The current response of the system to these superimposed components are then analysed and position information contained within them is extracted since the current response of the anisotropic machines will be modulated with the rotor position. HFVI has advantageous since high-frequency impedance of the machine allows reduced amplitude high-frequency current response. This also will result in low torque ripples. If the amplitude is not enough to provide a good estimate, high-frequency voltage component magnitude can always be regulated to provide a converging estimate, a feature being not so easy to implement in the HFCI methods [2].

In the HFCI method, high-frequency current components superimposed to the speed controller outputs are regulated with the current controllers. This is often a problem in terms of bandwidth with the conventional FOC current regulators, so some adjustments to the controllers might be necessary such as increasing the bandwidth or using separate or modified controllers for each component [2]. Good spectral separation of the current components is inevitable for a better estimation of the rotor position. This will mean a further increase of the current controller bandwidths, and if the current controllers fail to regulate the fundamental and high-frequency components at the same time, there will be loss of information on the negative sequence voltages, thus poor estimation [2]. Since this current will be regulated, the selection of amplitude and frequency is important so that the torque ripple is not an issue. Also, when high-frequency (HF) models are not used, some methods may require to measure HF voltage components. This either requires estimating voltages from the current controller outputs and using dead-time compensation methods, or voltage sensors [16].

Voltage injection is the popular method, considering its ease of implementation on the current hardware and software that is the bare minimum for a FOC method. Among the voltage injection methods, most popular two are sinusoidal rotating voltage injection or pulsating voltage injection method. The rotating HFI method is usually applied for sensorless control of IPMSM having large saliency values. On the other hand, the pulsating HFI method is preferred for the IPMSMs having small saliencies [38].

In pulsating HFI method, the injection is carried out in the d&q rotating reference frame. Although the injected voltage signal is sinusoidal, it is in the form of pulsating in the stationary reference frame [38]. A pulsating voltage vector of distinctly higher frequency than the fundamental frequency is superimposed on either d-axis or q-axis [39]. This results in a complex part in the current response. With driving the complex part in the current response to zero, actual position can be estimated. This method is also susceptible to multiple saliencies mentioned before. Voltages or currents can be injected considering the stationary reference frame or the estimated frame [4, 40].

Besides, the rotating HFI method is also widely used for sensorless control of all AC machines. The high-frequency signals are generally superimposed with two-phase stationary voltages and they are sinusoidal with constant amplitude. The decomposed high-frequency currents from the motor phase currents contain the rotor position information and it can be obtained with various signal processing techniques [41].

The injection in the stationary reference frame becomes more advantageous because the knowledge of the position information is needed for injection in the rotating reference frame. In the injection methods carried out in the d&q-axis, the estimated rotating reference frame is used according to estimated position and these methods are directly related to the estimation success. Another disadvantage is that the pulsating HFI technique is dependent of motor parameters which is not for rotating HFI technique [41].

Saliencies may be affected by saturation factors such as magnet flux and loading. Off-line calculation of the compensation function and on-line compensation is also possible [40].

HFI methods track spatial saliencies. These saliencies are created either by distinct geometries or saturated regions. Since these saliencies can be multiple, the type of saliencies should also be considered when comparing these methods. Saliencies can be sinusoidal, more distorted, etc. There can be more than one harmonic component due to the rotor geometry and stator structure for sinusoidal saliencies. For sinusoidal saliencies, current or voltage response are modulated sinusoidally and require proper demodulation and position extraction. HFI methods are affected by all types of saliencies, including single and harmonic saliencies, rotor slotting, magnetic anisotropy, magnet flux, loading, saturation, and cross saturation [39, 40]. Rotors with multiple saliencies should be analyzed carefully. Position tracking accuracy can be reduced where multiple and varying saliencies exist. The complete erroneous detection of d-axis is also possible.

High-frequency voltage injection methods can be performed successfully on SynRMs, PMaSynRMs and IPMSMs due to d&q-axis inductances those are noticeably different from each other [39]. As d-axis inductance is much higher than the q-axis inductance, high-frequency response during rotor rotation is varied considerably, leading to easier demodulation and position determination of these motors. Compensations methods are proposed that are created via off-line tests to account for offsets and position independent errors [39].

A few problems are associated with the HFI in PMaSynRMs like the selection for correct injected voltage amplitude and frequency, the magnet polarity detection, filter computing burden. For the determination of the injected frequency, a clear spectral separation is required. There are various algorithms for magnet polarity detection of PM motors. A most popular one is the stationary current response for PMSMs. The current time response method has some drawbacks and especially for PMaSynRMs, which have much lower number of magnets compared to PMSM. Magnitude of the voltage is another concern as the high-frequency currents may cause some acoustic noise. Variable HF voltage component amplitude and frequency is suggested using larger amplitudes during speed transients and lower voltage amplitudes during steady state so as to reduce acoustic noise during steady state [39]. Inverter switching distortions and analog/digital filtering of the carrier signals should also be considered [42].

1.3 Synchronous Reluctance Motor History

The concept of a synchronous reluctance motor has a long history because it is in principle the same as a salient rotor synchronous motor without rotor excitation [43]. The basic concepts and theory of the development of the reluctance torque in salient pole synchronous machines, the analysis of this type of synchronous machine on the d&q-axis were carried out by Blondel in 1913. In the Journal of AIEE, the first paper specifically about this motor was published by J.K. Kostko in 1923 [46]. It was recognized by Kostko that the performance of synchronous reluctance machines would be quite poor in terms of efficiency and power factor unless the machine was designed to achieve a high magnetic saliency. As a solution to this problem, they divided the rotor into multiple sections that act as flux routing to increase the difference in inductances of the d&q-axis. More specifically, Doherty and Nickle [47] published a classic paper in 1926 deriving the relationship between power per torque and load angle for salient pole synchronous machines without field excitation [48].

Despite its long history, the evolution of the synchronous reluctance motor towards high performance and its consequent industrial applications grew very slowly and only become a mature technique in the last decade of the 20th century [43]. There are two reasons for this delay. The first reason is that the search for a highly anisotropic rotor design was quite late since it began in the late 1950s [49] and they have generally concentrated on caged starting machines for special purposes [50]. These investigations led to many studies, especially the axially laminated anisotropic rotor structure [51, 52]. Unfortunately, the axially laminated structure is disadvantageous in terms of high iron losses in rotor laminations close to the air gap. This situation limits the efficiency advantages of the machine. Moreover, the significant manufacturability challenges associated with these axially laminated rotor structures have severely hindered their commercialization opportunities [48].

In the 1960s and 1970s, when solid-state inverter technology matured, commercial interest in the development of synchronous reluctance machines for adjustable speed drive applications increased [48]. The synchronous reluctance motor was developed especially in the 1960s as a line-start synchronous AC motor for use in applications with synchronous speed requirements [53]. Such motors were used as an example in the textile industry and were supplied by a common voltage source [54]. These variable speed machines had a great deal of attention as they operated in synchronization with the stator frequency, so they were an effective substitute for speed-regulated direct current motors and induction motors to produce higher quality fibers in the fiber-spinning factories [55]. The motors were obviously not individually controlled and there were no strict requirements on efficiency. The motor performance was poor in terms of power density or efficiency, but it was a cost-effective motor running at synchronous speed [54].

SynRMs were operated in open loop, similar to the switched reluctance motor drives of those days. The open loop control adjusts the inverter voltage and frequency independently of rotor speed and position. Continuous progress in induction motor drives and speed control techniques caused these motors to lose the market. However, improvements in rotor structure configurations have drawn a very positive outlook for this machine in the future market [55].

On the other hand, the widespread application of synchronous motors was unthinkable at that time without closed-loop operation, which requires a power-electronic supply. This power supply concept was applied in the field in BLDC and PMSM motors in the 1980s. At the same time, it gave a major impetus to research on high-performance synchronous reluctance motors and drives [53, 56, 57]. This paved the way for a mature design technique and then industrial application, first in the field of servo drives

[43]. The sensorless control trend is towards general purpose applications due to the suitability of such motors [43]. While permanent magnet synchronous machines have attracted significant interest from researchers for high-performance drive applications since the 1980s, there has also been high interest in the development of synchronous reluctance machines that do not require magnets or any field excitation [49].

In recent years, the commercialization of this technology has begun. One of the most important has been the series of SynRMs and PMaSynRMs and also drives, first presented by ABB in 2012 and now available in powers ranging from 5.5 to 315 kW for industrial applications. The key features for a 90 kW machine in this series are 96.1% efficiency at full load and a power factor of 0.73, demonstrating both the strengths and challenges of this technology [58].

1.4 Comparision of PMaSynRM with Other Motors and Its Application Areas

At the point we have come so far, induction motors have almost reached the limit of their structural and technological usefulness. Further increase in the efficiency of these motors is possible only by using solutions such as using more copper and steel material and using the copper squirrel cage of the rotor. The main disadvantages of such solutions are growth in the motor volume and increased costs. In addition, the use of copper squirrel cages causes a significant increase in the cost of production technology due to the high melting point of copper. Cost-acceptable induction motors only correspond to efficiency class IE2 [59, 60].

Currently, leading European manufacturers sell a SynRM with frequency converter for use in areas where the application of a frequency regulated motor can have a significant energy saving effect (e.g. for fan load, elevators and elevator drives). These areas account for more than 70% of all adjustable electric drive applications [49, 60].

Three-phase SynRMs and PMaSynRMs stand out from permanent magnet motors because of their simplicity in design and manufacturing. It is advantageous by the lack of permanent magnets, which are difficult to maintain and repair. In addition, the induction motor production technology has the highest agreement with SynRM among other motors [60].

Compared to other types of machines, SynRM is quite new in the industrial market, so it is not used widely yet. Companies like ABB are replacing induction machines mainly with synchronous reluctance machines due to their higher efficiency and better power densities for ventilation and pump applications such as heating and air conditioning [61]. SynRM motors show a higher torque density (approximately 15-20%) and an increased average efficiency (5-10%) compared to a conventional induction motor [62]. The efficiency and power density comparison between a traditional induction machine and a modern SynRM shown in Figure 1.1 highlights these differences obviously [61].

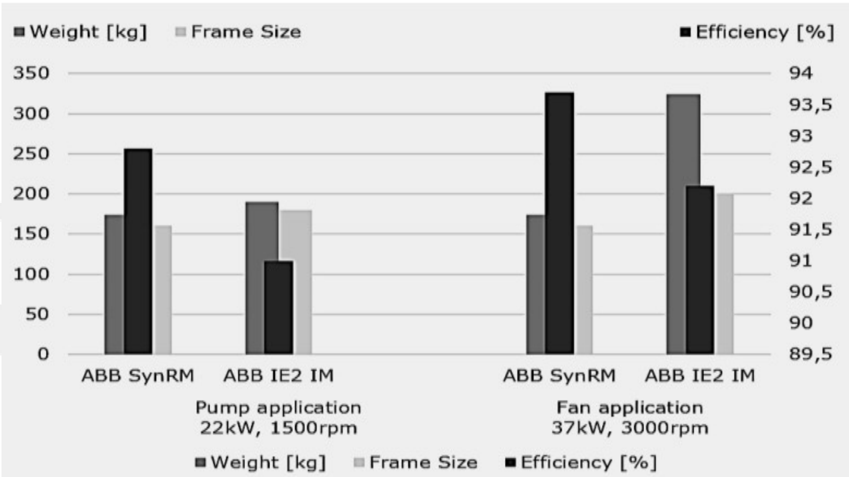

Figure 1.1 : Comparison of induction motor and SynRM for pump and fan application. (black: yield, white: size, grey: weight) [61].

Around the world, many electrical appliances are operating with electric motors, such as air conditioners, refrigerators, and washing machines. Single-phase induction motors, permanent magnet synchronous motors, and universal motors dominate the market in these applications. The design objectives of these motors are smaller dimensions, high power density, high efficiency, low maintenance, and cost. PMaSynRMs are also becoming an alternative to these motors in the home appliances industry [1].

The need for high efficiency motors in centrifugal machines, conveyor systems, fans and pumps, cranes, compressors, elevators, crushers and general machinery (winders, extruders and servo pumps) can be met by SynRM. PMaSynRM is an interesting choice, especially in electric aircraft applications [63].

The price of PMaSynRMs is much lower than traditional PMSM, making the motor preferable. The fact of using cheaper ferrite permanent magnets than rare earth permanent magnets provides a significant cost reduction. Although PMSMs are popular in electric and hybrid vehicles today, PMaSynRM is the most promising machine for next generation vehicles without rare earth permanent magnets [64].

As SynRM is a new motor topology, it is not yet used in electrified railway applications. In this field, induction motors and brushed direct current motors, which are more mature topologies, are mostly preferred [65]. SynRMs are designed with closed cooling to increase the reliability of the motor. This type of cooling is the criterion of choice in railway applications. Since SynRM does not have relatively high rotor losses as in an induction motor, closed cooling for SynRMs is sufficient. In addition, the machine volume can be further reduced because the rotor temperature is lower [65].

One of the US Navy's key principles for future ships and submarines is that electric machines should replace hydraulic and pneumatic fluid power systems that currently support operating equipment. The main component needed for both existing ships and future electric ships and submarines is the electric motor and generator. In the last few years, due to the growth in the electrification of ships, automobiles, etc., the need to develop inexpensive, flexible and reliable motor and generator systems has increased. The development of a universal stator lamination design that can be used in a variety of motors and generators is one way to reduce production, and maintenance costs. In this situation, PMaSynRM not only fulfills these requirements but also reduces machine costs with its cheap permanent magnets and winding free rotor [66].

2. PERMANENT MAGNET ASSISTED SYNCHRONOUS RELUCTANCE MOTOR

Variable speed drives are required at variable loads to increase efficiency and save energy. Pumps, fans, refrigerator compressors etc. can all benefit from variable speed. Recently, PMSMs with high-energy magnets have been proposed to replace the variable speed drives of some induction motors to increase power factor and efficiency. However, the high price of high-energy permanent magnets makes this solution questionable, especially for applications with upfront cost constraints. At this point, synchronous reluctance motor and synchronous reluctance motor with less magnets become advantageous in terms of cost [67].

2.1 Operating Principle

The SynRM operating principle is based on the torque of reluctance which is dependent on the saliency ratio. This value is defined as the ratio between the inductances in the d&q-axis. The SynRM working principle can be explained with a simple example. Consider the two objects presented in Figure 2.1. The object on the left has anisotropic geometry, while the object on the right has isotropic geometry. The object on the left has two axes. These are the d-axis along the path of maximum magnetic conductivity (low reluctance) and the q-axis along the path of minimum magnetic conductivity (high reluctance). The object on the right has a constant magnetic conductivity along any axis. When an external magnetic field is applied, the object on the left tends to lower magnetic resistance of the magnetic circuit. This is why a force arises that turns this object. However, the object on the right remains motionless due to its structure [68].

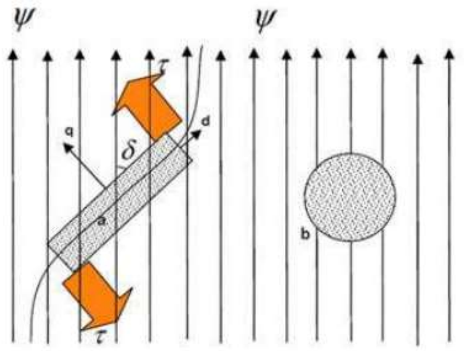

Figure 2.1 : Reluctance torque generation: anisotropic object on the left; right isotropic object [68].

As shown in Figure 2.2, SynRM also has a magnetically anisotropic rotor structure. It does not contain any permanent magnets or excitation windings in its rotor. On the other hand, the stator is the same structure as synchronous and induction motors, so the distributed winding type is preferred. A rotating magnetic field is created by currents flowing through the stator windings fed with three-phase sinusoidal voltages. The rotor tends to align with the stator rotating field. In other words, it tends to minimize the reluctance due to the principle of reluctance force described. This force causes a reluctance torque induced in the rotor. Thus, the rotor rotates synchronously with the stator rotating magnetic field [69].

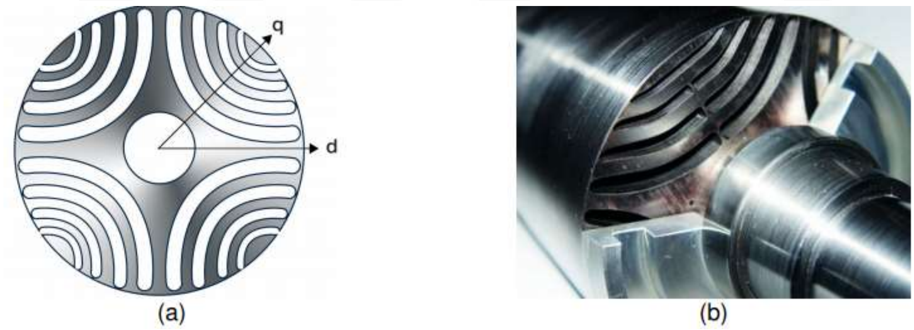

Figure 2.2 : SynRM rotor: (a) schematic representation of cross-section; (b) an example of a manufactured rotor [69].

2.2 Motor Construction

There are two main structures of SynRM and PMaSynRM as rotor construction. One of them is transversally laminated anisotropic (TLA) structure with transverse lamination, while the other is axially laminated anisotropic (ALA) structure with axial lamination. In TLA, the anisotropic structure is provided by the gaps created in the laminations, that is, by air barriers, while in ALA, the insulating laminations are used

[70]. Positioning and sizing of air canals directly affect the output torque, torque ripple, and other electrical and magnetic parameters [59].

A reluctance machine does not provide sufficient saliency with the concentric winding that has become popular in PMSMs. Due to the fact that efficiency and power factor are directly proportional to the saliency ratio, the SynRM stator must use a distributed winding configuration [71]. In addition, leakage inductances are lower in the distributed winding configuration since the space harmonic component of the stator EMF is lower in the distributed winding. The leakage inductance in addition to the winding inductance lowers the power factor which is also at low values in the reluctance machines [67]. Power factor of a SynRM is usually lower than that of an induction machine [71]. The reduction in power factor means more inverter current and power, hence more drive cost. SynRM rotor structures are shown in Figure 2.3.

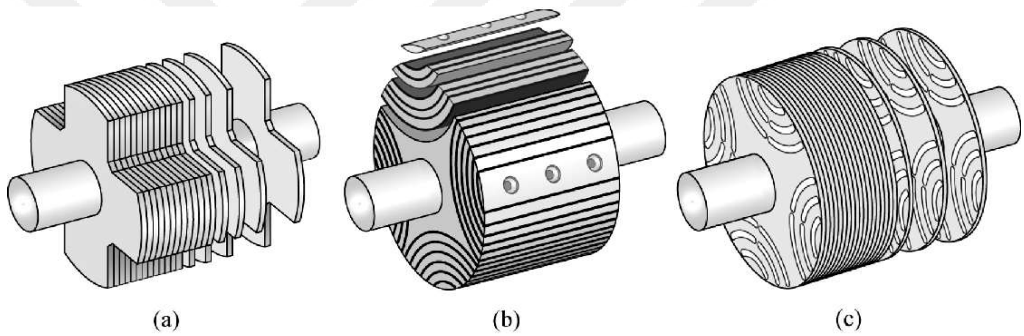

Figure 2.3 : SynRM rotor constructions (a) simple 4-pole salient rotor construction (b) ALA 4-pole rotor construction and (c) TLA 4-pole rotor construction [70].

The production cost for the TLA type SynRM can be competitive with the induction motor or even cheaper due to the elimination of the cage in the rotor and the casting process in the production line. If the same stator size is selected as the induction motor, SynRM can be produced on the same production line by simply changing the drilling tools for the rotor geometry. In addition, the TLA type rotor can be tilted easily in order to reduce the torque ripple as in an induction motor [70].

Since there is no cage in the rotor in SynRM, total copper losses are reduced. Therefore, the rated current can be taken higher in the SynRM for both machines at the same power dissipation or for the same temperature rise. This shows that SynRM can produce up to 20% to 40% higher torque compared to an induction motor. At the same stator current, the SynRM for a saliency ratio of about 10, produces about 90%

to 100% of the torque of the induction motor with about 50% lower overall loss and 5% to 8% higher efficiency [70].

The saliency ratio should be between 3.5 and 5 for PMaSynRM where ratio of magnet EMF voltage to stator voltage is lower than 0.3 so as to it have reasonable performance relative to an induction motor in the case of magnet support. Despite the magnet, the motor continues to compete on price. The usage of magnets is essential for a wide constant power region speed range (higher than 2.5 value) and for a high-power factor (higher than 0.8 value) [67]. The saliency ratio of 6 to 10 is necessary to maintain competition in the absence of magnet use [71].

The cross-coupling and cross-magnetization effect, which is called the dependence of each axis flux to the current in the other axis, is not linear and is also present in SynRM and PMaSynRM. Especially, the large q-axis currents cause the demagnetizing of the d-axis, known as the armature reaction. The cross-coupling effect is mainly caused by the iron portion of the rotor shared between the d&q-axis. Rotor bridges also increase this effect. The cross-coupling effect also effectively reduces the q-axis flux. The machine torque is reduced by both saturation and armature reaction effects via reducing d-axis inductance [70].

The absence of rotor current in a SynRM provides both benefits and harms. The advantage is that there are no copper losses in the rotor as mentioned above. The disadvantage is that compared to the induction motor, there is no rotor current to compensate for the armature reaction in the q-axis. This situation easily reduces the power factor in the SynRM drive. There is a simple but costly way to improve the power factor of a SynRM drive. The way is that magnets can be added to the q-axis to compensate for the q-axis armature reaction. The machine is called permanent magnet assisted SynRM as long as the torque produced by the magnets is smaller than the reluctance torque [71].

2.3 Equivalent Circuits and Modeling of SynRM

The synchronous reluctance motor can be modelled with two separate equivalent circuits. The one is for the d-axis and the other is for the q-axis in the rotating reference frame [72, 73]. The equivalent circuits of SynRM and the Thevenin equivalent circuits of these circuits are shown in Figure 2.4.

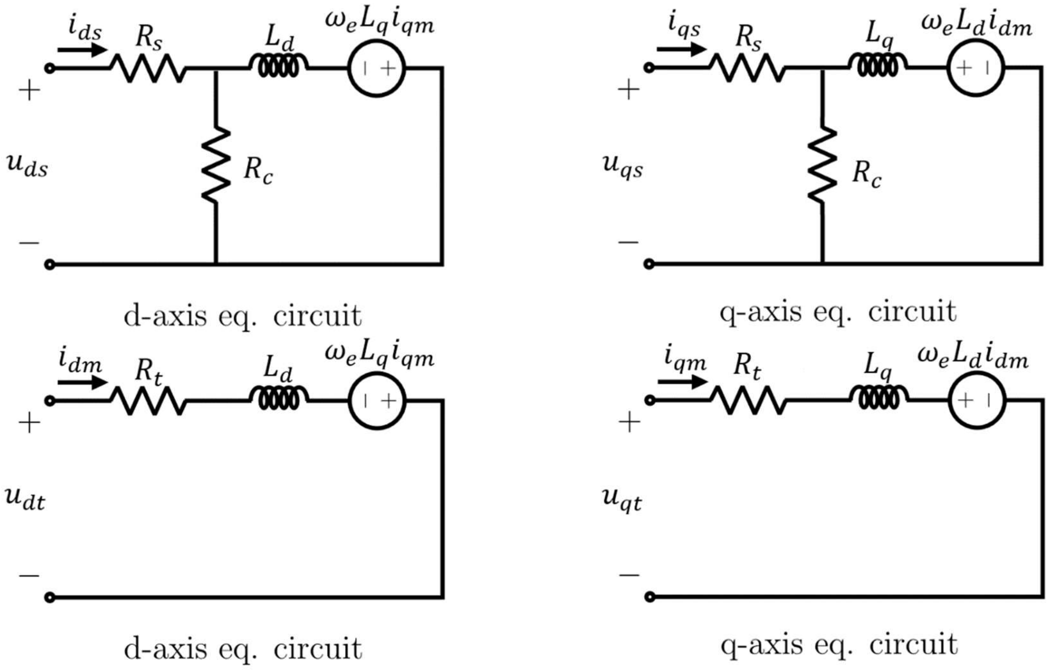

Figure 2.4 : The upper two circuits are the d&q-axis SynRM equivalent circuits containing iron losses, the lower two circuits are the Thevenin equivalent circuits of the upper circuits [74].

In the circuits, R_s and R_c represent the stator resistance and iron losses resistance, respectively, while L_d and L_q represent the stator winding inductances along the d&q-axis, respectively. $\omega_e L_q i_{qm}$ and $\omega_e L_d i_{dm}$ are rotational voltages due to cross-coupling. u_{ds}, u_{qs}, i_{ds} and i_{qs} are the d&q-axis stator voltages and currents, while u_{dt} and u_{qt} are Thevenin equivalent voltages. i_{dm} and i_{qm} are magnetization currents while i_{dc} and i_{qc} are iron losses currents.

The Thevenin resistance expression is given in equation 2.1.

$$R_t = \frac{R_c R_s}{R_c + R_s} \tag{2.1}$$

The Thevenin voltages are obtained with the voltage divider rule are shown in equation 2.2.

$$u_{dt} = u_{ds}\frac{R_c}{R_c + R_s}\ ;\ u_{qt} = u_{qs}\frac{R_c}{R_c + R_s}\ ; \tag{2.2}$$

The new d&q-axis voltage equations of the Thevenin equivalent circuit are obtained as in equations 2.3 and 2.4.

$$u_{dt} = R_t i_{dm} + \frac{d\lambda_{dm}}{dt} - \omega_e \lambda_{qm} = R_t i_{dm} + L_d \frac{di_{dm}}{dt} - \omega_e L_q i_{qm} \quad (2.3)$$

$$u_{qt} = R_t i_{qm} + \frac{d\lambda_{qm}}{dt} + \omega_e \lambda_{dm} = R_t i_{qm} + L_q \frac{di_{qm}}{dt} + \omega_e L_d i_{dm} \quad (2.4)$$

The voltage equations for the left loop of the equivalent circuits are obtained as in equation 2.5 in order to find the relationship between the iron losses current and the magnetizing current.

$$i_{dc} = \frac{v_{ds} - i_{ds} R_s}{R_c} = \frac{v_{ds} - (i_{dm} + i_{dc}) R_s}{R_c} \; ; \; i_{qc} = \frac{v_{qs} - i_{qs} R_s}{R_c} = \frac{v_{qs} - (i_{qm} + i_{qc}) R_s}{R_c} \quad (2.5)$$

Thus, the relationship between the iron losses current and the magnetizing current is as in equation 2.6.

$$i_{dc} = \frac{v_{ds} - i_{dm} R_s}{R_c + R_s} \; ; \; i_{qc} = \frac{v_{qs} - i_{qm} R_s}{R_c + R_s} \quad (2.6)$$

Equation 2.7 obtained by substituting equation 2.6 in equation 2.5 can be used for the transition from magnetizing current to stator current.

$$i_{ds} = \frac{v_{ds} + i_{dm} R_c}{R_c + R_s} \; ; \; i_{qs} = \frac{v_{qs} + i_{qm} R_c}{R_c + R_s} \quad (2.7)$$

As a result, the matrix form in equation 2.8 is created by using the voltage equations of Thevenin equivalent circuits. Thus, the mathematical model of SynRM including iron losses is created. The expression p in equation 2.8 corresponds to the derivative operation.

$$\begin{bmatrix} u_{dt} \\ u_{qt} \end{bmatrix} = \begin{bmatrix} R_t + pL_d & -\omega_e L_q \\ \omega_e L_d & R_t + pL_q \end{bmatrix} \begin{bmatrix} i_{dm} \\ i_{qm} \end{bmatrix} \quad (2.8)$$

2.4 Equivalent Circuits and Modeling of PMaSynRM

In case of magnet assist, the magnets added to the q-axis of rotor provide an increase in both torque and power factor as mentioned above. The equivalent circuits of PMaSynRM and the Thevenin equivalent circuits of these circuits are shown in Figure 2.5.

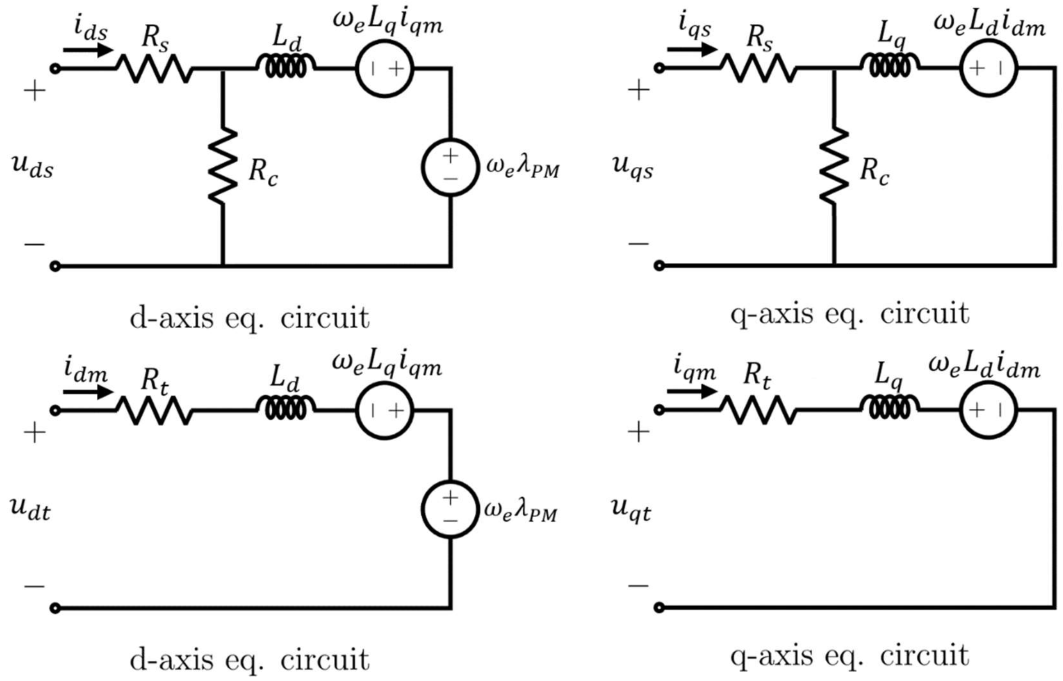

Figure 2.5 : The upper two circuits are the d&q-axis PMaSynRM equivalent circuits containing iron losses, the lower two circuits are the Thevenin equivalent circuits of the upper circuits [74].

Unlike SynRM mathematical modeling, only the effect of magnet-induced voltage is added to the d-axis equivalent circuit in PMaSynRM mathematical modeling. Thus, the matrix system obtained in equation 2.8 takes the form in equation 2.9 [64, 74].

$$\begin{bmatrix} u_{dt} \\ u_{qt} \end{bmatrix} = \begin{bmatrix} R_t + pL_d & -\omega_e L_q \\ \omega_e L_d & R_t + pL_q \end{bmatrix} \begin{bmatrix} i_{dm} \\ i_{qm} \end{bmatrix} + \begin{bmatrix} \omega_e \lambda_{PM} \\ 0 \end{bmatrix} \tag{2.9}$$

The torque equation takes form in equation 2.10. In addition to the reluctance torque, a magnet-induced electromagnetic torque is produced by the motor as seen in the torque equation.

$$T_e = \frac{3}{2} p \left[\lambda_{PM} i_{dm} + \left(L_d - L_q \right) i_{dm} i_{qm} \right] \tag{2.10}$$

3. CONTROL STRATEGIES OF PMaSynRM

Motor phase currents must be directly controlled to apply the control strategies developed for the motor. In addition to the amplitudes and frequencies, the phase angles of the currents should also be controlled. For this reason, the FOC technique is used for the current control loop of the PMaSynRM drive.

The main control strategies for PMaSynRM are given as maximum torque per ampere control (MTPA), fastest torque response control, maximum power factor control and maximum efficiency control. In this study, MTPA control is preferred for some advantages such as its simple algorithm, maximizing the output power beside the output torque for a specific speed value, etc.

The control strategies used for IPMSM and SynRM can also be adapted to PMaSynRM. Therefore, it is useful to first understand the MTPA control for SynRM which is simpler than MTPA control of PMaSynRM.

3.1 Field-Oriented Control of PMaSynRM

As for the current control side of the PMaSynRM, unlike scalar control, motor phase currents are directly controlled with the FOC technique. Not only frequency control but also amplitudes and phase angles of currents are controlled. The flux and torque are controlled separately as in a separately excited DC motor [75]. Thus, FOC provides the opportunity to control both the electromagnetic torque and the reluctance torque separately. This situation gives full control over the torque induced by the motor. The motor is controlled as desired control strategies with the FOC technique. The current control block scheme of field-oriented control for PMaSynRM is given in Figure 3.1.

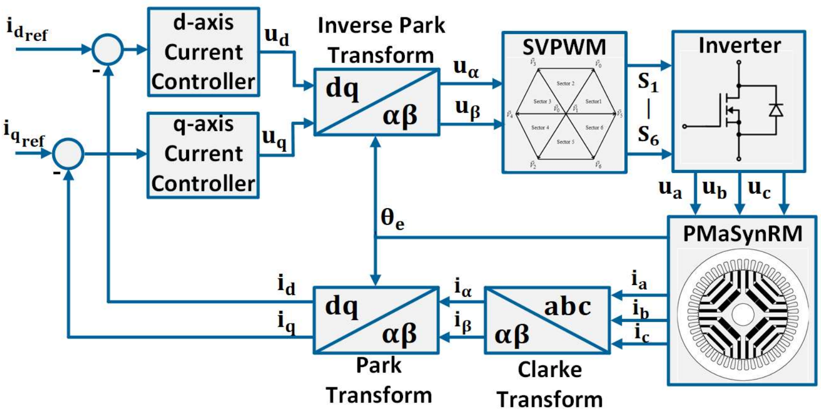

Figure 3.1 : Current control block scheme of field-oriented control.

The current control is carried out at a rotating d&q reference frame which is much easier than a stationary reference frame. Thus, Clarke and Park reference axis transformations are used for the control at the rotating reference frame. Besides, the Park transformation requires rotor position information as given in Figure 3.1. Therefore, rotor position information is essential and requires the use of sensors or uses sensorless control techniques [76].

The Clarke transformation and its inverse transformation are given in equation 3.1.

$$\begin{bmatrix}\alpha\\ \beta\\ 0\end{bmatrix}=\frac{2}{3}\begin{bmatrix}1 & -1/2 & -1/2\\ 0 & \sqrt{3}/2 & -\sqrt{3}/2\\ 1/2 & 1/2 & 1/2\end{bmatrix}\begin{bmatrix}a\\ b\\ c\end{bmatrix};\ \begin{bmatrix}a\\ b\\ c\end{bmatrix}=\begin{bmatrix}1 & 0 & 1\\ -1/2 & \sqrt{3}/2 & 1\\ -1/2 & -\sqrt{3}/2 & 1\end{bmatrix}\begin{bmatrix}\alpha\\ \beta\\ 0\end{bmatrix} \tag{3.1}$$

The Park transformation and its inverse transformation are given in equation 3.2.

$$\begin{bmatrix}d\\ q\\ 0\end{bmatrix}=\begin{bmatrix}cos(\theta_e) & sin(\theta_e) & 0\\ -sin(\theta_e) & cos(\theta_e) & 0\\ 0 & 0 & 1\end{bmatrix}\begin{bmatrix}\alpha\\ \beta\\ 0\end{bmatrix};\ \begin{bmatrix}\alpha\\ \beta\\ 0\end{bmatrix}=\begin{bmatrix}cos(\theta_e) & -sin(\theta_e) & 0\\ sin(\theta_e) & cos(\theta_e) & 0\\ 0 & 0 & 1\end{bmatrix}\begin{bmatrix}d\\ q\\ 0\end{bmatrix} \tag{3.2}$$

In the outer loop of the current control loop, the d&q axis reference currents are generated according to desired control strategy and reference speed.

3.2 Maximum Torque Per Ampere Control of SynRM

The active power equation depending on the synchronous machine load angle can be expressed in the form in equation 3.3.

$$P=3U_{s_{ph}}^2\frac{L_d-L_q}{2\omega_s L_d L_q}sin(2\delta_s)=3\,U_{s_{ph}}^2\frac{1-\dfrac{L_q}{L_d}}{2\omega_s L_q}\,sin(2\delta_s) \tag{3.3}$$

Equation 3.3 states that the difference of d&q-axis synchronous inductances should be as large as possible and product of d&q-axis synchronous inductances should be as small as possible in order to generate maximum power. In practice, the goal is to maximize the d-axis inductance and minimize the q-axis inductance. In principle, the machine can deliver its maximum torque at a load angle (δ_s) of 45°. Saturation and other situations may cause a significant deviation from this angle value [71].

Equation 3.4 contains the torque equation of SynRM. As can be seen here, the large difference of d&q-axis synchronous inductances as possible provides increase in the torque.

$$T_e = \frac{3}{2} p\left(L_d - L_q\right) i_{dm} i_{qm} \tag{3.4}$$

The main torque equation in equation 3.5 is used in order to obtain the torque equation depending on the current angle. The expressions in equation 3.6 are written instead of the quantities in the main torque equation.

$$|T_e| = p\left|\frac{3}{2}\lambda_s \, x \, i_{sm}\right| = \frac{3}{2} p\left(\lambda_{dm} i_{qm} - \lambda_{qm} i_{dm}\right) \tag{3.5}$$

$$i_d = I_{sm} cos\kappa \; ; \;\; i_q = I_{sm} sin\kappa \; ; \; \lambda_{dm} = L_d I_{sm} cos\kappa \; ; \; \lambda_{qm} = L_q I_{sm} sin\kappa \tag{3.6}$$

Thus, the structure in equation 3.7 is obtained.

$$T_e = \frac{3}{2} p\left(L_d I_{sm} cos\kappa I_{sm} sin\kappa - L_q I_{sm} sin\kappa I_{sm} cos\kappa\right) \tag{3.7}$$

The structure in equation 3.8 is obtained by placing equation 3.7 in common factor brackets.

$$T_e = \frac{3}{2} p\left(\left(L_d - L_q\right). I_{sm}^2. cos\kappa. sin\kappa\right) = \frac{3}{2} p\left(\left(L_d - L_q\right) I_{sm}^2 \frac{1}{2} sin(2\kappa)\right) \tag{3.8}$$

As a result, equation 3.9 is obtained depending on the current angle of the torque equation.

$$T_e = \frac{3}{4} p I_{sm}^2 \left(L_d - L_q\right) sin(2\kappa) \tag{3.9}$$

As can be seen here, the maximum torque is obtained when the current angle is 45° as in the power equation in equation 3.3.

Therefore, the reference d&q-axis currents are chosen in such a way that their ratio to each other is one, that is, they are equal to each other.

$$i_{qm_{ref}} = i_{dm_{ref}} \tag{3.10}$$

The magnitude value of the currents is obtained from the reference torque value. When the d&q-axis currents are taken equal as in equation 3.10, the torque equation takes its form in equation 3.11.

$$T_{e_{ref}} = \frac{3}{2}p\left(L_d - L_q\right)i_{dm_{ref}}i_{qm_{ref}} = \frac{3}{2}p\left(L_d - L_q\right)i_{dm_{ref}}^2 \tag{3.11}$$

As a result, the d-axis reference current is obtained as in equation 3.12.

$$i_{dm_{ref}} = \sqrt{\frac{2T_{e_{ref}}}{3p\left(L_d - L_q\right)}} \tag{3.12}$$

If the control is desired for a different current angle value against the saturation or other situations, the expression in equation 3.13 is used.

$$tan(\kappa) = \frac{i_{qm_{ref}}}{i_{dm_{ref}}} \tag{3.13}$$

The d-axis reference current is found depending on both the current angle and the reference torque by substituting expression of equation 3.13 in the torque equation.

$$T_{eref} = \frac{3}{2}p\left(L_d - L_q\right)i_{dref}i_{dref}\,tan(\kappa) = \frac{3}{2}p\left(L_d - L_q\right)i_{dref}^2\,tan(\kappa) \tag{3.14}$$

Finally, the d-axis reference current is expressed as in equation 3.15.

$$i_{dref} = \sqrt{\frac{2T_{eref}}{3p\left(L_d - L_q\right)tan(\kappa)}} \tag{3.15}$$

The q-axis reference current is also obtained from equation 3.16.

$$i_{qm_{ref}} = i_{dm_{ref}}\,tan(\kappa) \tag{3.16}$$

3.3 Maximum Torque Per Ampere Control of PMaSynRM

If equation 2.10 is expressed depending on the current angle and it takes the form in equation 3.17 [74].

$$T_e = \frac{3}{4} p\left(2\lambda_{PM} I_{sm} \cos(\kappa) + I_{sm}^2 (L_d - L_q) \sin(2\kappa)\right) \tag{3.17}$$

Then, equation 3.18 is formed to give the expression torque per stator current.

$$\frac{T_e}{I_{sm}} = \frac{3}{4} p\left(2\lambda_{PM} \cos(\kappa) + I_{sm} (L_d - L_q) \sin(2\kappa)\right) \tag{3.18}$$

As in equation 3.18, the current angle that will give the maximum torque per ampere is a different angle than 45°, and it does not have a certain value depending on the magnet flux, the difference in d&q-axis inductances and stator current value.

$$\frac{d\left(\frac{T_e}{I_{sm}}\right)}{d\kappa} = -\frac{3}{2I_s} p\left[\lambda_{PM} I_{sm} \sin\kappa + (L_d - L_q) I_{sm}^2 \cos(2\kappa)\right] = 0 \tag{3.19}$$

The current angle for MTPA is not also constant due to changes in the d&q-axis inductances or magnet flux during operation. Therefore, the current angle is not chosen as a fixed value, but it is written as a function. The current angle function for MTPA is shown in equation 3.20.

$$\kappa = asin\left(\frac{-\lambda_{PM} + \sqrt{\lambda_{PM}^2 + 8(L_d - L_q)^2 I_{sm}^2}}{4(L_d - L_q) I_{sm}}\right) \tag{3.20}$$

The MTPA trajectory obtained for the PMaSynRM used in the study and it is given in Figure 3.2 in d&q-axis currents plane. Besides, the voltage limit ellipse for the rated speed and the rated current limit circle of the motor are seen in the figure.

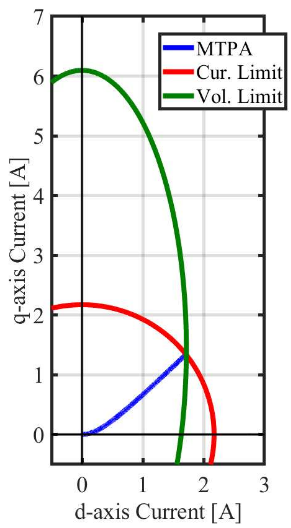

Figure 3.2 : The MTPA trajectory with voltage and current limits for the PMaSynRM.

4. SPACE VECTOR PWM TECHNIQUE FOR TWO-LEVEL INVERTERS

Space vector pulse-width modulation (SVPWM) technique is based on the principle of volt-second balance rule. The reference voltage vector can be obtained by two switching voltage vectors adjacent to this vector in the space vector plane. The reference voltage vector expression obtained from the volt-second balance rule for a switching period is given in equation 4.1 [77].

$$V_{ref} \,.\, T_s = V_1 \,.\, T_1 + V_2 \,.\, T_2 + V_0 \,.\, T_0 \tag{4.1}$$

In the equation, V_1 and V_2 represent switching vectors adjacent to the reference voltage vector. V_0 (or V_7) represents the zero-voltage vector. T_1, T_2 and T_0 are the switching timing of these adjacent vectors and the zero-voltage vector in one switching period. As an example, the production of a reference voltage in the first sector by neighbour vectors is shown in Figure 4.1.

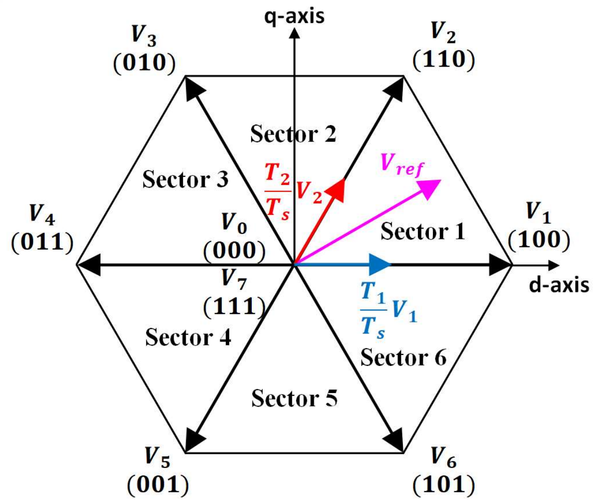

Figure 4.1 : Voltage space plane of three-phase inverter [78].

The switching timing of switching vectors expressions adjacent to the reference voltage vector for different sectors (n) are given in equations 4.2 and 4.3 [79].

$$T_1 = \frac{\sqrt{3}T_s\left|V_{ref}\right|}{V_{DC}} sin\left(n\frac{\pi}{3} - \theta\right) \tag{4.2}$$

$$T_2 = \frac{\sqrt{3}T_s|V_{ref}|}{V_{DC}} sin\left(\theta - (n-1)\frac{\pi}{3}\right) \tag{4.3}$$

The switching period is obtained by including the switching timing of the zero-voltage vector. Thus, the remaining time in the switching period is allocated to the zero-voltage vector.

$$T_0 = T_s - T_1 - T_2 \tag{4.4}$$

An example of the switching pattern of the SVPWM technique given in Figure 4.2 where the first sector [80]. When the figure is examined, it will be seen that only two switch states are changing at the same time thanks to this switching pattern. This situation ensures the minimum number of switching.

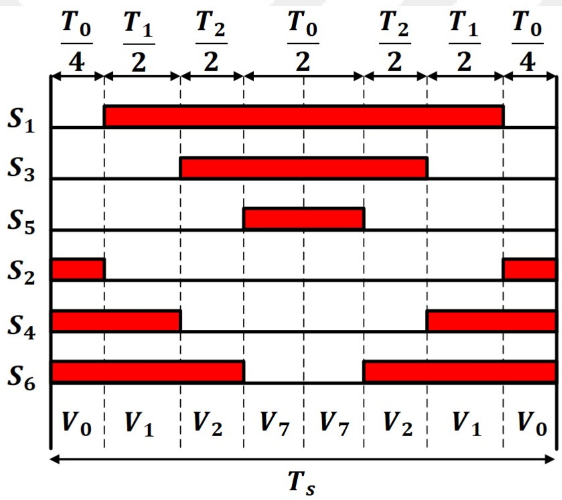

Figure 4.2 : A switching pattern example of SVPWM technique for the first sector [78].

The duty cycles of the neighbour space voltage vectors are obtained based on equations 4.2, 4.3 and 4.4. The duty cycles are as shown in equations 4.5, 4.6 and 4.7 [81].

$$d_1 = \frac{\sqrt{3}|V_{ref}|}{V_{DC}} sin\left(n\frac{\pi}{3} - \theta\right) \tag{4.5}$$

$$d_2 = \frac{\sqrt{3}|V_{ref}|}{V_{DC}} sin\left(\theta - (n-1)\frac{\pi}{3}\right) \tag{4.6}$$

$$d_0 = 1 - d_1 - d_2 \tag{4.7}$$

The expression of the reference voltage in terms of duty cycles is obtained as in equation 4.8. Figure 4.3 illustrates obtaining the voltage by using the duty cycles.

$$V_{ref} = d_1 . V_1 + d_2 . V_2 + d_0 . V_0 \tag{4.8}$$

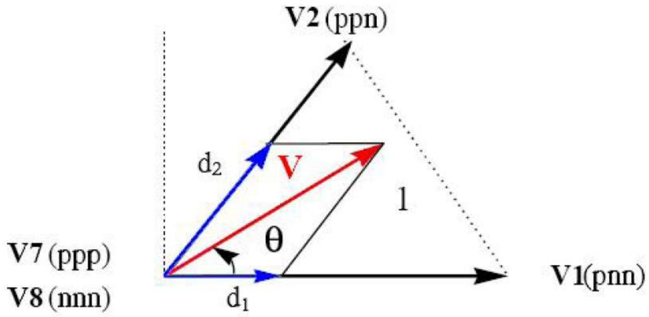

Figure 4.3 : Obtaining the reference voltage in terms of duty cycles [81].

The amplitude value of reference vector corresponds to the peak value of the reference phase-neutral voltage. √3 times this value gives the peak value of the reference phase-to-phase voltage and the maximum phase-to-phase voltage is equal to DC bus voltage in a two-level inverter. Hence, the modulation index is expressed as in equation 4.9 [82].

$$m = \frac{\sqrt{3}\left|V_{ref}\right|}{V_{DC}} \ , \ \ 0 \leq m \leq 1 \tag{4.9}$$

As a result, the duty cycles of neighbour vectors take their form in equations 4.10 and 4.11.

$$d_1 = m\,.\,sin\left(n\frac{\pi}{3} - \theta\right) \tag{4.10}$$

$$d_2 = m\,.\,sin\left(\theta - (n-1)\frac{\pi}{3}\right) \tag{4.11}$$

The phase voltages corresponding to each space vector for each switching state are given in Table 4.1.

Table 4.1 : Phase voltages formed by space voltage vectors corresponding to different switching states [77].

Space Voltage Vector	Switching States			Phase Voltages		
	S1	**S3**	**S5**	V_a	V_b	V_c
V_1	1	0	0	$2V_{dc}/3$	$-V_{dc}/3$	$-V_{dc}/3$
V_2	1	1	0	$V_{dc}/3$	$V_{dc}/3$	$-2V_{dc}/3$
V_3	0	1	0	$-V_{dc}/3$	$2V_{dc}/3$	$-V_{dc}/3$
V_4	0	1	1	$-2V_{dc}/3$	$V_{dc}/3$	$V_{dc}/3$
V_5	0	0	1	$-V_{dc}/3$	$-V_{dc}/3$	$2V_{dc}/3$
V_6	1	0	1	$V_{dc}/3$	$-2V_{dc}/3$	$V_{dc}/3$
V_7	1	1	1	0	0	0
V_0	0	0	0	0	0	0

The average phase voltages obtained for each sector according to Table 4.1 are passed to the d&q reference frame. As a result, the voltages in the d&q reference frame are obtained for each sector as shown in equations 4.12 and 4.13. The angle α here represents the angle difference between the reference voltage vector and the d&q reference frame.

$$u_{ds} = m\,.\frac{V_{dc}}{\sqrt{3}}cos(\alpha) \tag{4.12}$$

$$u_{qs} = m\,.\frac{V_{dc}}{\sqrt{3}}sin(\alpha) \tag{4.13}$$

Consequently, the switching function matrix in the d&q reference frame is obtained as in equation 4.14.

$$\begin{bmatrix} d_d \\ d_q \end{bmatrix} = \begin{bmatrix} \frac{m}{\sqrt{3}}cos(\alpha) \\ \frac{m}{\sqrt{3}}sin(\alpha) \end{bmatrix} \tag{4.14}$$

Finally, the d&q-axis voltages in terms of d&q-axis switching functions are obtained as shown in equations 4.15 and 4.16.

$$u_{ds} = d_d V_{dc} \tag{4.15}$$

$$u_{qs} = d_q V_{dc} \tag{4.16}$$

The sum of the squares of the d and q axis voltages cannot be greater than the square of the DC voltage value considering the voltage limit.

$$u_{ds}^2 + u_{qs}^2 \leq V_{dc}^2 \tag{4.17}$$

Therefore, the expression of equation 4.18 is obtained for d&q-axis switching functions.

$$d_d^2 + d_q^2 \leq 1 \tag{4.18}$$

5. SENSORLESS CONTROL OF PERMANENT MAGNET ASSISTED SYNCHRONOUS RELUCTANCE MOTOR WITH THE EXTENDED EMF MODEL

The position information is needed for vector control and speed information is needed for closed-loop speed control for AC motor control. The speed and position information are usually obtained through position sensors such as encoder and resolver. However, sensorless vector control is very popular in industrial applications where these position sensors are not used. In these applications, the position and speed information are obtained by various estimation methods. The motivation in choosing sensorless control instead of control with a sensor is low cost, reduced hardware complexity and size, improved robustness of the control system and less maintenance. Figure 5.1 shows the block diagram of a typical sensorless AC motor control [20].

When model-based position estimation algorithms are considered, similar results are obtained in terms of performance since they can be derived from each other. Thus, extended EMF model is preferred in this study for its basic structure. In this stage, the decisive effect on estimation performance is observer selection. A sliding mode observer (SMO) for estimation of EEMF components is preferred because of its quick response, robust structure and easy implementation [83].

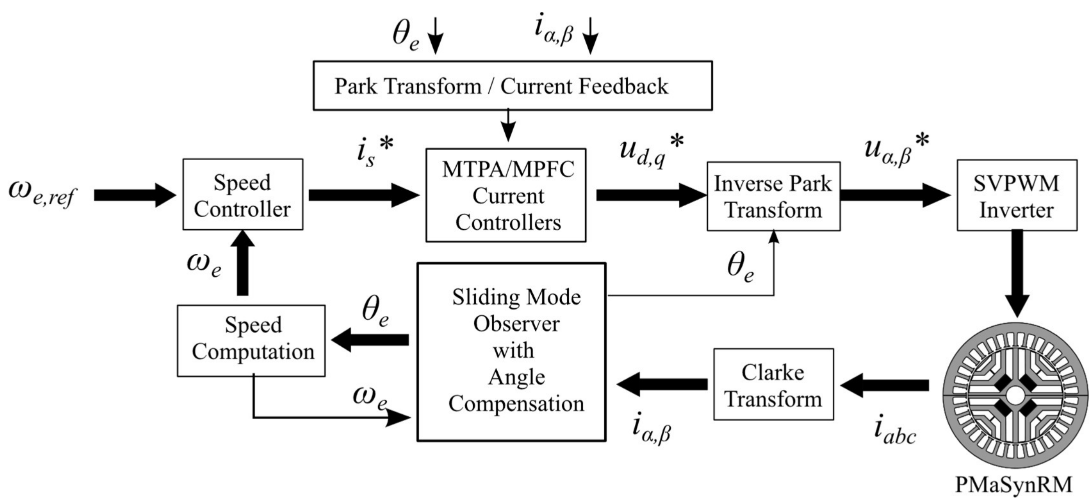

Figure 5.1 : A typical AC motor drive block diagram [83].

The EEMF technique is used for higher speed from a tested medium speed which changes according to the drive system hardware and the motor. The performance of this technique is directly related to the estimation performance of EEMF components whose amplitudes decrease with the motor speed [83]. Besides, the EEMF technique is also suitable for higher speed from the rated speed at the flux-weakening operation region. A fixed gained observer design is insufficient for wide-range sensorless speed control. In this stage, the adaptive observer structures are used and adjusted according to change of motor speed in the flux-weakening regions [36].

5.1 Motor Mathematical Model with Extended EMF Expression

The mathematical model of the PMaSynRM in the d&q reference frame is given in equation 2.9. The mathematical model of the motor in the d&q reference frame is transformed to the α&β reference frame. The current coefficient matrix in the d&q reference frame is decomposed to obtain the extended EMF expression before the reference frame transformation. The decomposition is performed from the first row of the current coefficient matrix as seen in equation 5.1 [26].

$$\begin{bmatrix} u_{dt} \\ u_{qt} \end{bmatrix} = \begin{bmatrix} R_t + pL_q & -\omega_e L_d \\ \omega_e L_d & R_t + pL_q \end{bmatrix} \begin{bmatrix} i_{dm} \\ i_{qm} \end{bmatrix} + \begin{bmatrix} (L_d - L_q) p i_{dm} \\ 0 \end{bmatrix} + \begin{bmatrix} \omega_e (L_d - L_q) i_{qm} \\ 0 \end{bmatrix} + \begin{bmatrix} \omega_e \lambda_{PM} \\ 0 \end{bmatrix} \tag{5.1}$$

The model transformed to α&β reference frame is given in equation 5.2.

$$\begin{bmatrix} u_{\alpha t} \\ u_{\beta t} \end{bmatrix} = \begin{bmatrix} R_t + pL_q & -\omega_e (L_d - L_q) \\ \omega_e (L_d - L_q) & R_t + pL_q \end{bmatrix} \begin{bmatrix} i_{\alpha m} \\ i_{\beta m} \end{bmatrix} + (L_d - L_q) p i_{dm} \begin{bmatrix} cos\theta_e \\ sin\theta_e \end{bmatrix} + \omega_e (L_d - L_q) i_{qm} \begin{bmatrix} cos\theta_e \\ sin\theta_e \end{bmatrix} + \omega_e \lambda_{PM} \begin{bmatrix} cos\theta_e \\ sin\theta_e \end{bmatrix} \tag{5.2}$$

Equation 5.3 is obtained in simplified form when the common factor of the separated part and the magnet EMF is taken into brackets.

$$\begin{bmatrix} u_{\alpha t} \\ u_{\beta t} \end{bmatrix} = \begin{bmatrix} R_t + pL_q & -\omega_e (L_d - L_q) \\ \omega_e (L_d - L_q) & R_t + pL_q \end{bmatrix} \begin{bmatrix} i_{\alpha m} \\ i_{\beta m} \end{bmatrix} + \left((L_d - L_q)(p i_{dm} + \omega_e i_{qm}) + \omega_e \lambda_{PM} \right) \begin{bmatrix} cos\theta_e \\ sin\theta_e \end{bmatrix} \tag{5.3}$$

The part that is separate from the current coefficient matrix is expressed as the extended EMF part. Then, the simplification process is taken one step further and the α&β components of the extended EMF are created as shown in equation 5.4.

$$e_{ext} = \begin{bmatrix} e_\alpha \\ e_\beta \end{bmatrix} = |e_{ext}| \begin{bmatrix} cos\theta_e \\ sin\theta_e \end{bmatrix} = \left((L_d - L_q)(pi_{dm} + \omega_e i_{qm}) + \omega_e \lambda_{PM} \right) \begin{bmatrix} cos\theta_e \\ sin\theta_e \end{bmatrix} \quad (5.4)$$

As a result, the mathematical model of the motor in the α&β-axis takes the form in equation 5.5.

$$\begin{bmatrix} u_{\alpha t} \\ u_{\beta t} \end{bmatrix} = \begin{bmatrix} R_t + pL_q & -\omega_e(L_d - L_q) \\ \omega_e(L_d - L_q) & R_t + pL_q \end{bmatrix} \begin{bmatrix} i_{\alpha m} \\ i_{\beta m} \end{bmatrix} + \begin{bmatrix} e_\alpha \\ e_\beta \end{bmatrix} \quad (5.5)$$

The extended EMF voltages could be used as state variables in the state space model to be created. Therefore, the expression that gives the derivatives of the extended EMF voltages is needed. The derivative expression of extended EMF voltages is given in equation 5.6 with some omissions. These omissions are already zero in steady-state which are the derivatives of the d&q-axis currents and the derivative of the speed.

$$p \begin{bmatrix} e_\alpha \\ e_\beta \end{bmatrix} = p \left((L_d - L_q)(pi_{dm} + \omega_e i_{qm}) + \omega_e \lambda_{PM} \begin{bmatrix} cos\theta_e \\ sin\theta_e \end{bmatrix} \right) = \omega_e |e_{ext}| \begin{bmatrix} -sin\theta_e \\ cos\theta_e \end{bmatrix} \quad (5.6)$$

Finally, the derivatives of extended EMF voltages are obtained as given in equation 5.7.

$$p \begin{bmatrix} e_\alpha \\ e_\beta \end{bmatrix} = \omega_e \begin{bmatrix} -e_\beta \\ e_\alpha \end{bmatrix} \quad (5.7)$$

5.2 PMaSynRM State Space Model Using Extended EMF Voltages

PMaSynRM state space model is created by choosing α&β-axis currents as state variables and EEMF voltages are separated. The state space model obtained from equations 5.5 and 5.7 is seen in equation 5.8.

$$p \begin{bmatrix} i_{\alpha m} \\ i_{\beta m} \end{bmatrix} = \begin{bmatrix} \frac{-R_t}{L_q} & \frac{\omega_e(L_d - L_q)}{L_q} \\ \frac{-\omega_e(L_d - L_q)}{L_q} & \frac{-R_t}{L_q} \end{bmatrix} \begin{bmatrix} i_{\alpha m} \\ i_{\beta m} \end{bmatrix} + \begin{bmatrix} \frac{1}{L_q} & 0 \\ 0 & \frac{1}{L_q} \end{bmatrix} \begin{bmatrix} u_{\alpha t} \\ u_{\beta t} \end{bmatrix} + \begin{bmatrix} -\frac{1}{L_q} & 0 \\ 0 & -\frac{1}{L_q} \end{bmatrix} \begin{bmatrix} e_\alpha \\ e_\beta \end{bmatrix} \quad (5.8)$$

Here, the EEMF components should be estimated with using an observer structure. The selected observer SMO is used for estimation stage. A sliding surface is created according to the error of stationary reference frame currents. The signum functions of these current errors with a designed sliding gain (K_{slide}) create the observer structure as shown in equation 5.9. Since the α&β-axis dynamic equations have the same form, the observer coefficients used are taken as equal.

$$\begin{bmatrix} \hat{e}_\alpha \\ \hat{e}_\beta \end{bmatrix} = K_{slide} \begin{bmatrix} sgn(i_{\alpha m} - \hat{\imath}_{\alpha m}) \\ sgn(i_{\beta m} - \hat{\imath}_{\beta m}) \end{bmatrix} \tag{5.9}$$

The estimated EEMF components in equation 5.9 should be passed from a low pass filter because the SMO has the chatter by its nature. Thus, a smoother estimation could be provided. The state space model including the estimated EEMF components and the SMO structure is given in equation 5.10. A circumflex has been added to the variables to express their estimation values.

$$p \begin{bmatrix} \hat{\imath}_{\alpha m} \\ \hat{\imath}_{\beta m} \end{bmatrix} = \begin{bmatrix} \frac{-R_t}{L_q} & \frac{\omega_e(L_d - L_q)}{L_q} \\ \frac{-\omega_e(L_d - L_q)}{L_q} & \frac{-R_t}{L_q} \end{bmatrix} \begin{bmatrix} \hat{\imath}_{\alpha m} \\ \hat{\imath}_{\beta m} \end{bmatrix} + \frac{1}{L_q} \begin{bmatrix} u_{\alpha t} \\ u_{\beta t} \end{bmatrix}$$
$$- \frac{K_{slide}}{L_q} \begin{bmatrix} sgn(i_{\alpha m} - \hat{\imath}_{\alpha m}) \\ sgn(i_{\beta m} - \hat{\imath}_{\beta m}) \end{bmatrix} \tag{5.10}$$

Observer coefficients are chosen so that the error between the estimated current and the actual current will reach zero. The observer coefficients are adjusted so that the estimated extended EMF voltages have a critically damped behaviour. Besides, high observer coefficients cause noise the extended EMF waveforms. The coefficients will lead the model to instability after a certain size. Because of these situations, a smooth position estimation could not be achieved or even an estimation cannot be made.

5.3 Position Estimation with Extended EMF Components

It is possible to estimate the position using the estimated extended EMF voltages. The ratio of the obtained extended EMF voltage components as in equation 5.11 gives us the tangent value of the electrical position. In this point, the electrical position can be obtained from the arctangent of the ratio of the voltages. Besides, the estimation could be achieved with using two-argument arctangent (atan2) for four-quadrant. An attention should be paid to the signs of the sine and cosine extended EMF components.

The signs of the components change when the motor rotates in the opposite direction due to the velocity component in the extended EMF voltage expression.

$$\frac{\hat{e}_{\beta}}{\hat{e}_{\alpha}} = \frac{|\hat{e}_{ext}| sin\hat{\theta}_e}{|\hat{e}_{ext}| cos\hat{\theta}_e} = tan\hat{\theta}_e \rightarrow \hat{\theta}_e = atan2(\hat{e}_{\beta}, \hat{e}_{\alpha}) \tag{5.11}$$

The high-frequency harmonic content of the estimated extended EMF voltages will also exist in the position estimation. Therefore, it would be appropriate to estimate the position after the EMFs are passed through a low-pass filter with as high cut-off frequency as possible. A low-pass filter with a low cut-off frequency will cause a delay in the EMFs as well as in the position estimation. As a result, the position estimation error will increase according to the delay value. Also, the delay in position will directly cause a deviation in the generated optimum d&q-axis currents. Finally, this situation will cause an increase in stator current amplitudes and therefore a decrease in the motor efficiency.

5.4 Speed Estimation with Using Estimated Position

The estimated position value is used for speed estimation [23]. The motor speed value is obtained by taking the derivative of the estimated position. The derivative value reaches extreme values at discontinuity points due to the sawtooth waveform of the output of the arctangent function. These discontinuous moments are determined and the previous derivative value is preserved instead of the current derivative value. The derivative value one step earlier is kept constant for this solution.

$$\hat{\omega}_e = \frac{d\hat{\theta}_e}{dt} \tag{5.12}$$

As in position estimation, a low-pass filter with as high cut-off frequency as possible should be used in speed estimation. Otherwise, the phase delay will have negative effects on the speed response of the motor. More damped responses and higher settling times are among these negative effects.

5.5 Simulation Results for EEMF Technique with Sliding Mode Observer

The PMaSynRM used in this study is a washing-machine motor. Both simulations and experiments are carried out by using this motor. The motor has ferrite magnets and its parameters are given in Table 5.1. Since sensorless operation could not be achieved with the extended EMF method at zero speed and low speeds, PMaSynRM is initially started with sensor. Then, the motor is passed to sensorless operation during steady-state. The voltage and current values used in the observer are passed through a low-pass filter with the same cut-off frequency in order to eliminate the switching harmonics. Applying the same low pass filter is important so that the delays that will occur are the same for current and voltages. The delays which are sourced by low-pass filters cause increment in position estimation error. A compensation position value is added to estimated position against this problem.

Table 5.1 : The parameters of the PMaSynRM.

Parameter	Value
Rated power[W]	377
Rated torque [Nm]	1.2
Rated speed [rpm]	3000
Number of pole pair	4
Rated current [A]	1.62

The sensorless control of the PMaSynRM with the EEMF technique is simulated in the MATLAB/Simulink platform. Besides, SVPWM and three-phase inverter models are integrated into the simulation for more realistic results. Because the motor stator voltages are in pulse-width modulation (PWM) waveforms same as in the experimental case. The simulation model parts are given in the following figures.

The motor model is shown in Figure 5.2. The mathematical model is created according to PMaSynRM dynamic equations.

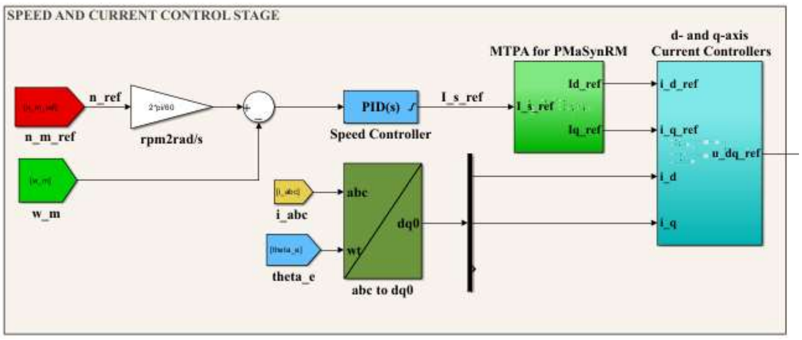

Figure 5.2 : The speed control stage of PMaSynRM.

The sensorless operation must be implemented at medium speed because the EMF voltages are directly related to the rotor speed. Thus, the sensorless operation is realized 800 ms after the starting. The d&q-axis current references are formed according to MTPA algorithm.

The actual, reference and estimated speed of the motor is shown in Figure 5.3 for the speed estimation performance. Firstly, the motor is started with 300 rpm speed reference and no-load operation. After 800ms from start, the motor passes to sensorless operation. Then, the motor is accelerated to rated speed of 3000 rpm. After that, the rated load is included in the system in the form of a 0.5 second ramp after 3 seconds. After loading, the motor is decelerated to 300 rpm again for the test of starting with rated load. Thus, the motor is brought to 3000 rpm with rated load. After all, it is seen that stable sensorless operation is achieved for different situations.

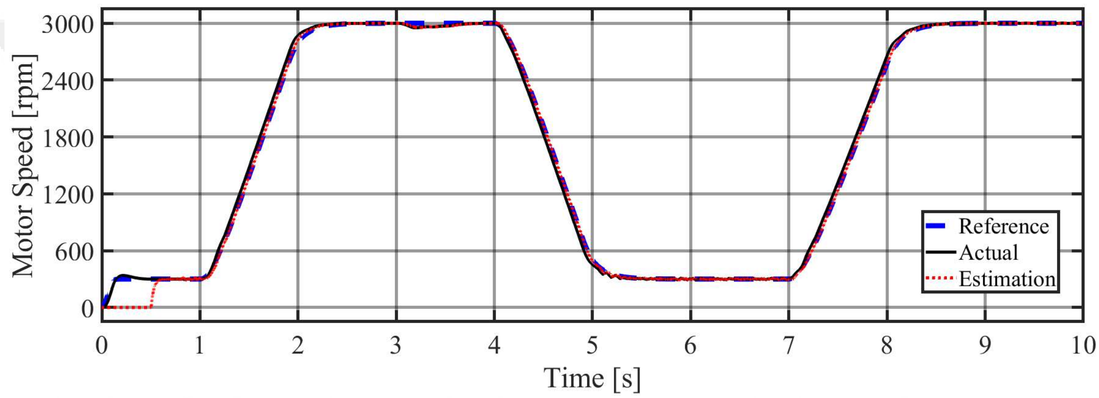

Figure 5.3 : The drive cycle of EEMF sensorless control.

In Figure 5.4, the actual position value obtained from the motor and the position value obtained by the observer is presented. Despite the different speed and load conditions, there is no loss of tracking in the position estimation. Although the actual position value is different from zero, the position estimation algorithm has caught the correct value.

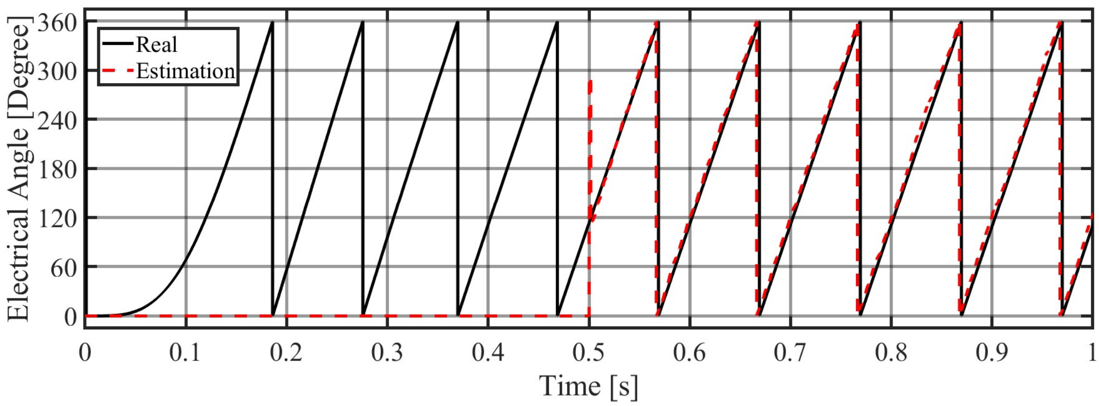

Figure 5.4 : The position estimation at 300 rpm.

Closer view of the position estimation tracking is given in Figure 5.5 for motor in rated values.

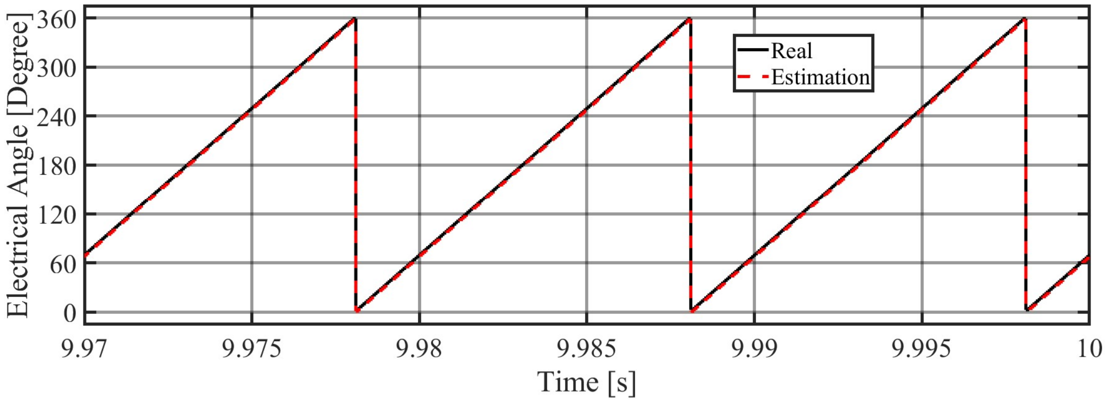

Figure 5.5 : The position estimation with the rated load at 3000 rpm.

The entire range of position estimation error is given in Figure 5.6. The compensation position value is chosen specially to compensate the error at motor in rated values where efficiency concern is higher. However, it should be considered that the error should not be increased too much at low speeds to avoid loss of speed control.

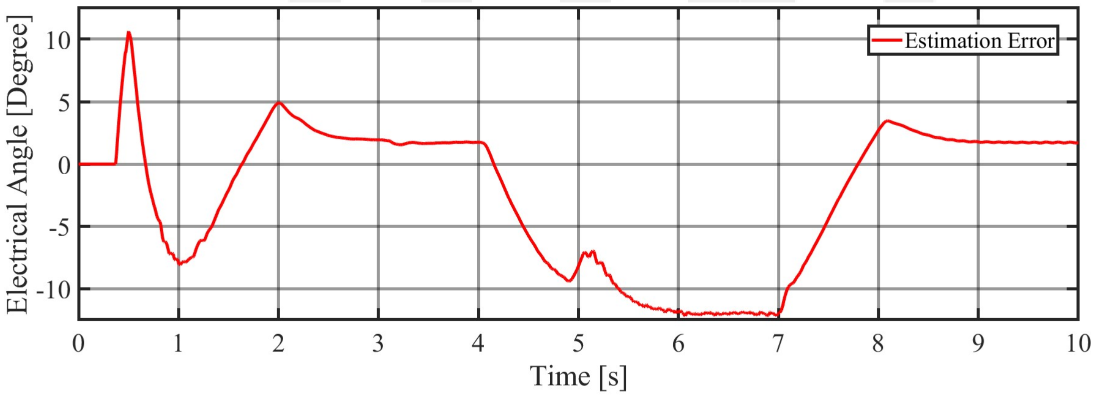

Figure 5.6 : The position estimation error by using the EEMF technique.

The estimated α&β-axis currents are given Figure 5.7 and 5.8. The estimation performance is directly related to the position estimation performance. Because, the success in the current estimation means the correct estimation of the EEMF values.

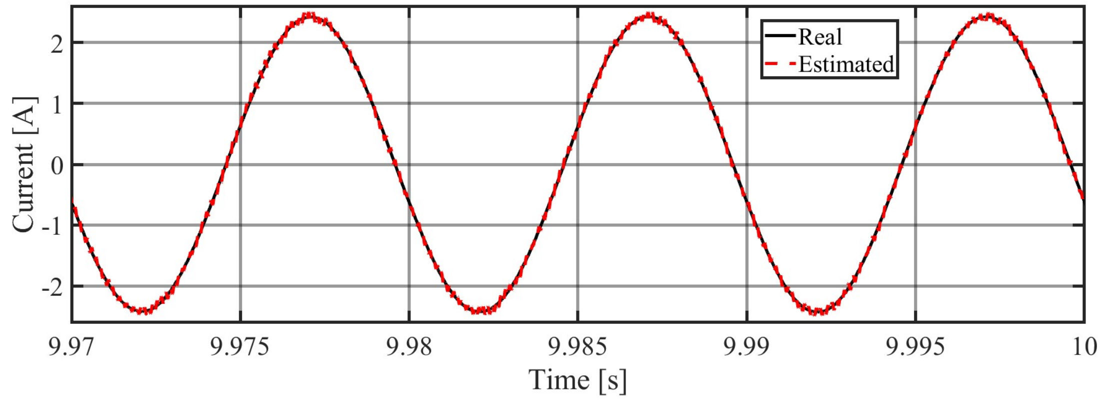

Figure 5.7 : The α component of stator current estimation.

Besides, the estimation should be as smooth as possible, in the same way the position estimation will be smooth.

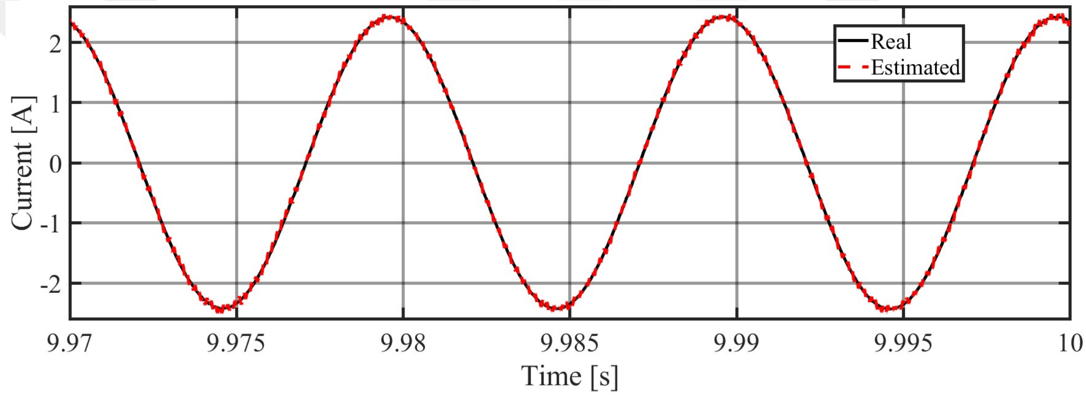

Figure 5.8 : The β component of the stator current estimation.

The estimated EEMF components which are used for position estimation are shown in Figure 5.9. The EEMF components are obtained as smoothly as possible.

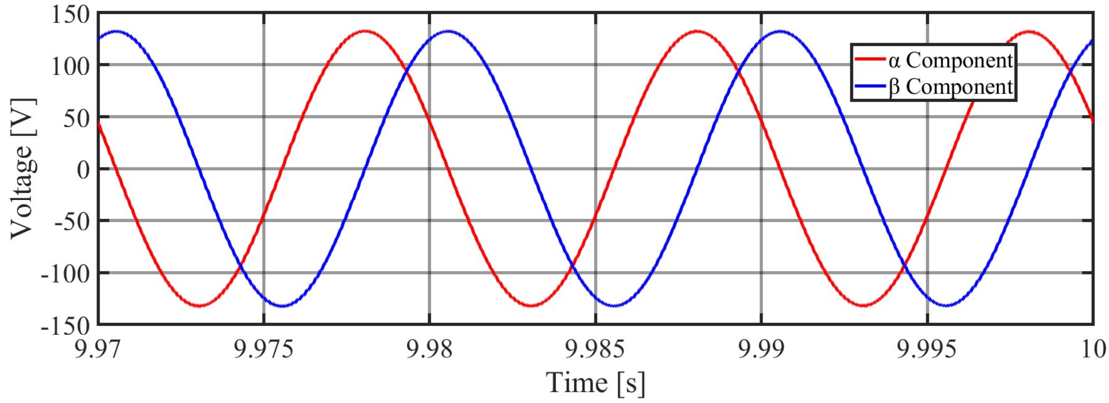

Figure 5.9 : The estimated EEMF α and β components.

5.5.1 Evaluation of simulation results

As a result of the simulations, a successful sensorless close-loop speed control is achieved with using EEMF model and SMO observer between medium and rated speed range. The position estimation error is ensured to be around 2° at the rated speed value, where the efficiency is high and critical.

6. SENSORLESS CONTROL WITH HIGH-FREQUENCY VOLTAGE INJECTION

The extended EMF components depend on the angular speed and the derivative of the d-axis current that is seen in equation 5.6. The derivative of the d-axis current can be assumed to be zero for steady state. The angular speed value causes the related components to be quite small at low motor speeds. This situation makes position estimation very difficult. Furthermore, initial position estimation cannot be performed when the motor is in standstill position. Because extended EMF components do not exist at zero speed when the motor is stopped [24, 84].

Against this problem, the HFI method is mostly used to perform low and zero speed position estimation. HFI method is an alternative method in which rotor position estimation is performed thanks to its anisotropic structure in the rotor of IPMSM and reluctance motors, as in the extended EMF method. If the method is to be summarized, high-frequency voltages or currents are superimposed from relevant stages in the motor control algorithm. Then, high-frequency signals are separated from the motor output currents and the position information is obtained by various methods applied to these signals [85].

6.1 Difference Between High-Frequency Current and High-Frequency Voltage Injection

Injected signals may be voltage or current signals. Therefore, the method is divided into HFVI and HFCI in this regard. The HFVI method is simpler method in the regard that it can be applied without modification to the FOC scheme prepared for the speed control with sensor. In HFVI method, high-frequency components of suitable magnitude and frequency are superimposed on the current controller outputs as shown in Figure 6.1. Then, the current response of the system to these superimposed components is analysed. Since the current response of anisotropic machines are be modulated by the rotor position, they contain rotor position information. Thus, the rotor position can be obtained with using these current signals. The high-frequency impedance of the machine ensures that the amplitude of the high-frequency currents is low and in this case the torque ripple based on HFI is also reduced. The fact that the HFVI method allows HFI becomes advantageous in this regard. In addition, the amplitudes of the injected voltages can be easily increased for estimation optimization, and this feature is not so easy to implement in HFCI method [24].

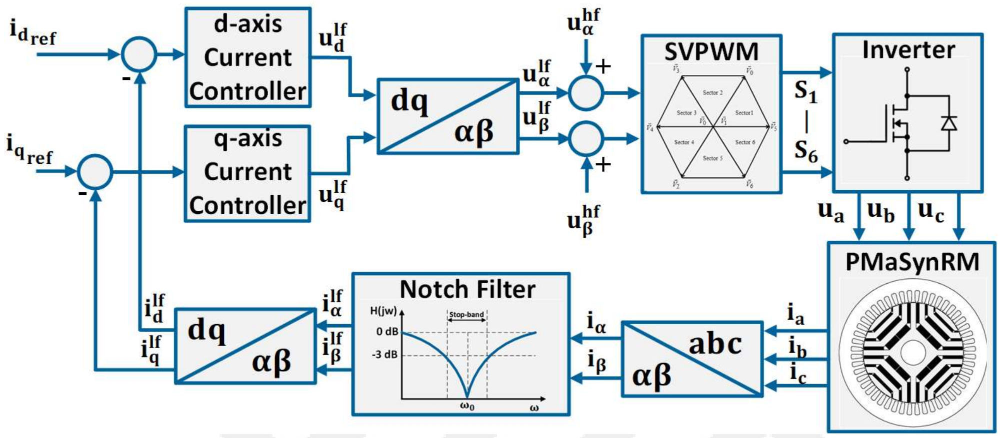

Figure 6.1 : High-frequency voltage injection in the motor current loop [3].

In the HFCI method, high-frequency current components superimposed to the current references are regulated with the current controllers. This technique may cause troubles in terms of bandwidth of the conventional FOC current controllers so that some adjustments for current controllers might be necessary such as increasing the bandwidth or using separate controllers for each component [24]. Generally, separation of the current components is necessary for better estimation of the rotor position. If the current controllers do not effectively regulate the fundamental and high-frequency components at the same time, there will be information loss, which will result in an unsuccessful estimation performance [24]. At the same time, good amplitude and frequency of HF signals selection should be made so that torque ripples are not a problem.

6.2 Difference Between Pulsating and Rotating High-Frequency Voltage Injection

In brief, HFVI is the popular method, considering its ease of implementation on the current hardware and software that is more suitable for a field-oriented control. Rotating voltage injection and pulsating voltage injection methods are generally preferred in HFVI techniques. For SynRM, PMaSynRM and IPMSM have large saliency, the rotating HFI method becomes more advantageous. In addition, the pulsating HFI method is more appropriate for the IPMSMs has small saliency [38].

In pulsating HFI method, the injection is carried out in the d&q rotating reference frame. Although the injected voltage signal is sinusoidal, it is in the form of pulsating in the stationary reference frame [38]. A pulsating voltage vector of distinctly higher frequency than the fundamental frequency is superimposed on the estimated axis of choice, either d-axis or q-axis [39]. This results in a complex part in the current response. With driving the complex part in the current response to zero, actual position can be estimated. Moreover, HF current can also be injected considering the stationary reference frame or the estimated frame [4, 16].

Besides, the rotating HFI method is also widely used for sensorless control of all AC machines. The HF signals are generally superimposed with two-phase stationary voltages and they are sinusoidal with constant amplitude. The decomposed HF currents from the motor phase currents contain the rotor position information and it can be obtained with various signal processing techniques [41].

The injection in the stationary reference frame becomes more advantageous because the knowledge of the position information is needed for injection in the rotating reference frame. In the injection methods carried out in the d&q-axis, the estimated rotating reference frame is used according to estimated position and these methods are directly related to the estimation success. Another disadvantage is that the pulsating HFI technique is dependence of motor parameters which is not for rotating HFI technique [41].

6.3 Selection of Frequency and Amplitude of High-Frequency Components

Injection methods, appropriate selection of the amplitude and frequency of the injected signal, are necessary to obtain a quality signal of position and velocity estimation [86]. With HFI, frequencies in the range of ten times the maximum fundamental frequency in the control range and one tenth of the inverter switching frequency are selected. The amplitude is chosen to be large enough to measure high-frequency currents and acceptably small against to the torque fluctuations [84, 87, 88].

$$10f_{hf} \leq f_{sw} \tag{6.1}$$

Selected amplitude and frequency of the injected voltage are decisive as it determines the amplitude of high-frequency current generated. Therefore, the amplitude and frequency of the injected voltage should be as high as possible to generate high-frequency currents that high signal-to-noise ratio and as low as possible so that the high-frequency currents do not cause high losses and also inducing acoustic noise.

6.4 Feedback Currents Filtering

Another issue in the HFI technique is the feedback currents. Even if the HF voltage is injected, the induced HF currents are also received by the current controller feedback loops. This situation causes distortion on the voltage references which are current controller outputs. Generally, the low-pass filters are used for this process. However, notch filters are preferred in this study because of some reasons. The first reason is that notch filter has better transient response according to the low-pass filters. The slow response causes deterioration and overshoots in the current controllers because of their large bandwidths and step loads. Second one is notch filters are better performance in filtering HF components for same effect at fundamental frequency. Due to these reasons, notch filters are used in this study. The bode plot of the designed notch filter is given in Figure 6.2.

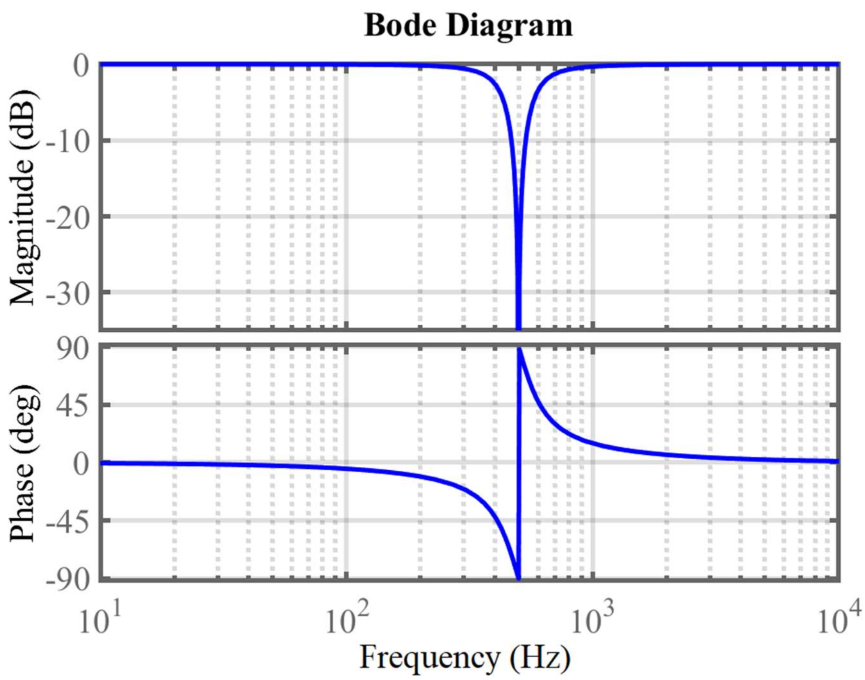

Figure 6.2 : Bode plot of Notch filter applied to feedback phase currents.

Basically, the notch filter center frequency should be same with the frequency of HFI voltage. Additionally, the bandwidth frequency of notch filter is designed considering the rotor speed. Thus, the negative component of HFI currents frequency decreases with rotor speed as will be mentioned later sections.

6.5 Obtaining High-Frequency Equivalent Circuit

Starting from the previously given d&q reference frame shown in equation 6.2, the motor equivalent circuit model is converted to a stationary reference frame [87, 88].

$$\begin{bmatrix} u_{dt} \\ u_{qt} \end{bmatrix} = \begin{bmatrix} R_t + pL_d & -\omega_e L_q \\ \omega_e L_d & R_t + pL_q \end{bmatrix} \begin{bmatrix} i_{dm} \\ i_{qm} \end{bmatrix} + \begin{bmatrix} \omega_e \lambda_{PM} \\ 0 \end{bmatrix} \tag{6.2}$$

The equivalent circuit model in this stationary reference frame is created as shown in equation 6.3.

$$\begin{aligned} \begin{bmatrix} u_{\alpha t} \\ u_{\beta t} \end{bmatrix} &= \begin{bmatrix} R_t - 2\omega_e L_1 \, sin(2\theta_e) & 2\omega_e L_1 \, cos(2\theta_e) \\ 2\omega_e L_1 \, cos(2\theta_e) & R_t + 2\omega_e L_1 \, sin(2\theta_e) \end{bmatrix} \begin{bmatrix} i_{\alpha m} \\ i_{\beta m} \end{bmatrix} \\ &+ \begin{bmatrix} (L_0 + L_1 \, cos(2\theta_e) & L_1 \, sin(2\theta_e) \\ L_1 \, sin(2\theta_e) & (L_0 - L_1 \, cos(2\theta_e) \end{bmatrix} \frac{d}{dt} \begin{bmatrix} i_{\alpha m} \\ i_{\beta m} \end{bmatrix} + \omega_e \lambda_{PM} \begin{bmatrix} cos(\theta_e) \\ sin(\theta_e) \end{bmatrix} \end{aligned} \tag{6.3}$$

The average inductance, L_0 and difference inductance, L_1 expressions here are given in equation 6.4.

$$L_0 = \frac{L_d + L_q}{2} \; ; \; L_1 = \frac{L_d - L_q}{2} \tag{6.4}$$

The part that should be emphasized in this model is the inductance matrix part shown in equation 6.5.

$$L(\theta_e) = \begin{bmatrix} L_0 + L_1 \, cos(2\theta_e) & L_1 \, sin(2\theta_e) \\ L_1 \, sin(2\theta_e) & L_0 - L_1 \, cos(2\theta_e) \end{bmatrix} \tag{6.5}$$

The stator voltages and currents in the stationary reference frame consist of high and low frequency components as in equations 6.6 and 6.7.

$$u_{\alpha\beta t} = (u^{hf}_{\alpha\beta m}) + (u^{lf}_{\alpha\beta m}) \tag{6.6}$$

$$i_{\alpha\beta t} = (i^{hf}_{\alpha\beta m}) + (i^{lf}_{\alpha\beta m}) \tag{6.7}$$

The equivalent circuit model in equation 6.3 takes the form in equation 6.8 when the electrical angular speed (ω_e) is assumed to be approximately zero, considering the low speed at which position estimation will be made. Here, I is the identity matrix.

$$(u_{\alpha\beta m}^{hf}) + (u_{\alpha\beta m}^{lf}) = (R_t I + L(\theta_e)p)\left((i_{\alpha\beta m}^{hf}) + (i_{\alpha\beta m}^{lf})\right) \tag{6.8}$$

In this state, the model is only decomposed into a circuit model that is in injected frequency. In this case, considering the high-frequency reactances and low amplitude currents, the stator resistances can be neglected. Thus, the model is reduced to equation 6.9.

$$u_{\alpha\beta m}^{hf} \approx L(\theta_e)\frac{d}{dt}\left(i_{\alpha\beta m}^{hf}\right) \tag{6.9}$$

The inductance matrix is inverted and thrown across the equation and the stator current derivatives are left alone.

$$\frac{d}{dt}\left(i_{\alpha\beta m}^{hf}\right) = \left(L(\theta_e)\right)^{-1} u_{\alpha\beta m}^{hf} \tag{6.10}$$

Finally, derivatives of the obtained stator currents are shown in equation 6.11 in its final form.

$$\frac{d}{dt}\begin{bmatrix} i_{\alpha m}^{hf} \\ i_{\beta m}^{hf} \end{bmatrix} = \frac{1}{L_d L_q}\begin{bmatrix} (L_0 - L_1 \cos(2\theta_e) & -L_1 \sin(2\theta_e) \\ -L_1 \sin(2\theta_e) & (L_0 + L_1 \cos(2\theta_e)) \end{bmatrix}\begin{bmatrix} u_{\alpha m}^{hf} \\ u_{\beta m}^{hf} \end{bmatrix} \tag{6.11}$$

6.6 High-Frequency Voltage Injection and High-Frequency Stator Currents

The expression of the high-frequency voltages to be injected is found in equation 6.12. In order for the high-frequency stator currents to be in the desired form, the voltage components are formed in this way [88].

$$\begin{bmatrix} u_{\alpha m}^{hf} \\ u_{\beta m}^{hf} \end{bmatrix} = V_{hf}\begin{bmatrix} -\sin(\omega_h t) \\ \cos(\omega_h t) \end{bmatrix} \tag{6.12}$$

When these voltages are substituted in equation 6.11, the model takes the form in equation 6.13.

$$\frac{d}{dt}\begin{bmatrix} i_{\alpha m}^{hf} \\ i_{\beta m}^{hf} \end{bmatrix} = \frac{V_{hf}}{L_d L_q}\begin{bmatrix} (L_0 - L_1 \cos(2\theta_e) & -L_1 \sin(2\theta_e) \\ -L_1 \sin(2\theta_e) & (L_0 + L_1 \cos(2\theta_e)) \end{bmatrix}\begin{bmatrix} -\sin(\omega_h t) \\ \cos(\omega_h t) \end{bmatrix} \tag{6.13}$$

When both sides are integrated, high-frequency stator currents are obtained as in equation 6.14. As it can be understood from here, these currents contain position information.

$$\begin{bmatrix} i_{\alpha m}^{hf} \\ i_{\beta m}^{hf} \end{bmatrix} = \begin{bmatrix} I_{i0}\cos(\omega_h t) - I_{i1}\cos(2\theta_e - \omega_h t) \\ I_{i0}\sin(\omega_h t) - I_{i1}\sin(2\theta_e - \omega_h t) \end{bmatrix} \tag{6.14}$$

The expressions I_{i0} and I_{i1} here are given in equation 6.15.

$$I_{i0} = \frac{V_{hf} L_0}{\omega_h L_d L_q} \; ; \; I_{i1} = \frac{V_{hf} L_1}{\omega_h L_d L_q} \tag{6.15}$$

6.7 Decomposition of Position Error from High-Frequency Currents and Position Estimation

The stator currents are subjected to several processes to obtain the position information which is in the negative sequence component ($-I_{i1}$) [88-90]. The block diagram of this procedure is shown in Figure 6.3. $i_{\alpha\beta1}^{hf}$, $i_{\alpha\beta2}^{hf}$ and $i_{\alpha\beta3}$ in Figure 6.3 represent the current outputs of the synchronous frame filter stages, respectively.

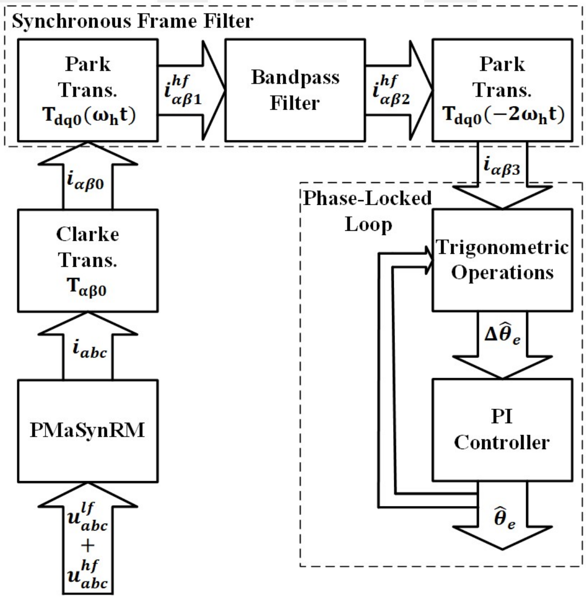

Figure 6.3 : Position information parsing block diagram [3].

Firstly, the phase currents transformed to two-phase stationary reference frame with Clarke transformation. After that Park transformation (αβ0-dq0) is applied to the currents at with the frequency of $\omega_h t$ in order to make negative sequence component separable.

$$i_{\alpha\beta}^{hf} = \begin{bmatrix} i_{\alpha1}^{hf} \\ i_{\beta1}^{hf} \end{bmatrix} = \begin{bmatrix} I_s\cos(\omega_e t - \omega_h t) \\ I_s\sin(\omega_e t - \omega_h t) \end{bmatrix} + \begin{bmatrix} I_{i0} - I_{i1}\cos(2\theta_e - 2\omega_h t) \\ I_{i0} - I_{i1}\sin(2\theta_e - 2\omega_h t) \end{bmatrix} \tag{6.16}$$

Then, the constant value (I_{i0}) and fundamental current part are eliminated utilizing a band-pass filter, and the remainder is the negative sequence component as shown in 6.17.

$$i_{\alpha\beta2}^{hf} = \begin{bmatrix} i_{\alpha2}^{hf} \\ i_{\beta2}^{hf} \end{bmatrix} = \begin{bmatrix} -I_{i1}cos(2\theta_e - 2\omega_h t) \\ -I_{i1}sin(2\theta_e - 2\omega_h t) \end{bmatrix} \tag{6.17}$$

The transfer function of the band-pass filter is given in equation 6.18 where f_g is the bandwidth frequency, and f_0 is the center frequency.

$$G_{BPF}(s) = \frac{2\pi f_g s}{s^2 + 2\pi f_g s + (2\pi f_0)^2} \tag{6.18}$$

The center frequency is selected according to the twice the HFI frequency. Figure 6.4 gives the bode plot of the band-pass filter.

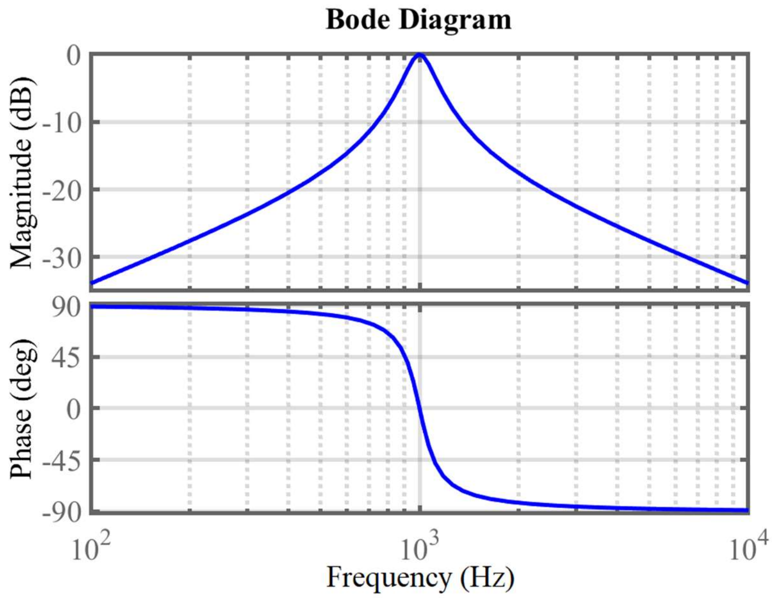

Figure 6.4 : Bode plot of the band-pass filter.

This time, Clarke to Park (αβ0-dq0) transformation is applied at the frequency of $-2\omega_h t$ to eliminate the high-frequency angle value and decompose the position information. As a result, the structure in equation 6.19 with position information, decoupled from high-frequency, is obtained.

$$i_{\alpha\beta3} = \begin{bmatrix} i_{\alpha3} \\ i_{\beta3} \end{bmatrix} = \begin{bmatrix} -I_{i1}cos(2\theta_e) \\ -I_{i1}sin(2\theta_e) \end{bmatrix} \tag{6.19}$$

6.8 Position and Speed Estimation with PLL

The position information may be obtained directly from the remaining currents using the arcsine or arccosine function. However, the phase-locked loop (PLL) method provides smoother estimation with filtering HF peaks [90]. The PLL block scheme is given in Figure 6.5.

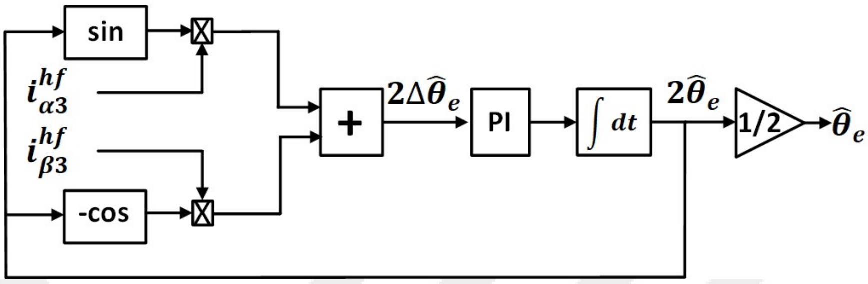

Figure 6.5 : The phase-locked loop scheme for position estimation [3].

In PLL method, a position estimation error is created with trigonometric operations. The position estimation is then performed by a controller, usually a PI controller, smoothly taking this error to zero.

Firstly, the current components of $i_{\alpha\beta 3}$ are multiplied by the sine and minus cosine of the position estimate value as in equation 6.20.

$$\varepsilon_{\theta\_sin} = [-I_{i1}\, cos(2\theta_e) \quad -I_{i1}\, sin(2\theta_e)] \begin{bmatrix} sin(2\hat{\theta}_e) \\ -cos(2\hat{\theta}_e) \end{bmatrix} \tag{6.20}$$

The structure takes the form as in equation 6.21 according to the trigonometric equations.

$$\varepsilon_{\theta\_sin} = -I_{i1}\, sin\left(2(\hat{\theta}_e - \theta_e)\right) \tag{6.21}$$

The equation takes its form as in equation 6.22 when trigonometric expression is left alone.

$$\varepsilon_{\theta\_sin} = -I_{i1}\, sin\left(2(\hat{\theta}_e - \theta_e)\right) \rightarrow \varepsilon_{\theta\_sin} = I_{i1}\, sin\left(2(\theta_e - \hat{\theta}_e)\right) = I_{i1}\, sin(2\Delta\hat{\theta}_e) \tag{6.22}$$

Considering that the error will go to zero here, the position estimation error can be taken equal to the trigonometric expression according to sine function.

$$\varepsilon_{\theta\_sin} = I_{i1}\, sin(2\Delta\hat{\theta}_e) \cong 2\Delta\hat{\theta}_e \quad , \Delta\hat{\theta}_e \rightarrow 0 \tag{6.23}$$

As a result, half of the output obtained with the PLL structure gives the electrical position. The electrical position is also divided by the number of pole pairs to obtain the mechanical position. Thus, it is possible to make the motor speed estimation using the derivative of obtained mechanical position estimation. While taking the derivative of the position estimation, on the other hand, this derivative value is examined and stable speed estimation is performed.

6.9 Initial Rotor Position Detection with Magnet Polarity Determination

The electrical position of the rotor, which is found by the HFI method, is estimated with an error of 180° if the permanent magnet polarity is incorrectly determined. Thus, the d&q-axis of the motor is placed incorrectly. Therefore, magnet polarity should be determined and the obtained axes should be verified [91].

The pilot voltage injection method will be used to accurately estimate the initial position of the rotor. The working principle of this method is based on injecting two pilot voltages of different signs but same amplitude and time interval along the estimated q-axis into the motor stator windings as illustrated in Figure 6.6. The correct position value is reached by comparing the peak values of the q-axis currents resulting from the injected voltages [92]. The advantages of this technique are its simplicity, ease of application, and short time required for polarity detection. However, the injection must be stopped and the current control disabled in the process [93]. SVPWM is used to generate a voltage pulse along the q-axis and vice versa in the space vector plane of the three-phase inverter shown in Figure 6.6 and does not require any extra hardware [94].

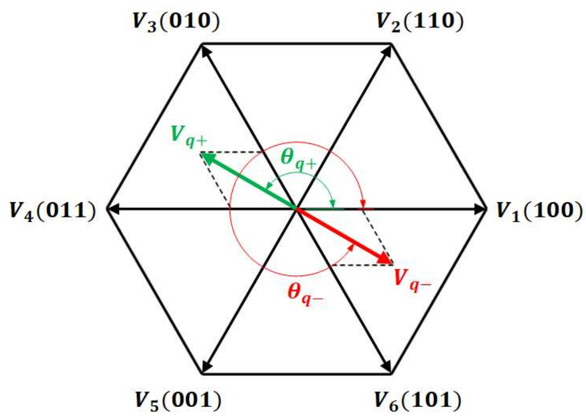

Figure 6.6 : Pilot voltages in the three-phase inverter space vector plane [94].

The reached peak values of the two q-axis currents will be different from each other due to the decreasing inductance with the effect of magnetic saturation [95]. It should be noted that the applied pilot voltage vectors must be large enough to cause magnetic saturation. Thus, the difference between the currents will be more distinct [94]. Since voltage is applied to the motor only in the q-axis direction, no torque is produced and the rotor does not move during the test procedure [93]. Both cases of between stator and magnet flux during this test are given in Figure 6.7.

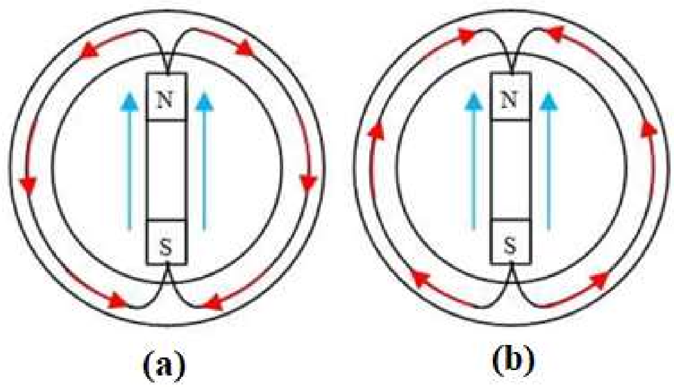

Figure 6.7 : Cases of fluxes created by pilot voltages with magnet flux [24].

Moreover, if the flux direction produced by the pilot voltage is the same as the permanent magnet flux, as in Figure 6.7(a), the q-axis of the motor enters saturation and the inductance decreases. In the opposite case in Figure 6.7(b), the inductance becomes higher because the total flux decreases. Thus, the peak value of the current flowing through the stator windings will be less than in the first case. The polarity of the rotor permanent magnet is easily determined with this significant difference in currents [24, 94]. Figure 6.8 shows the steps to find the initial rotor position of the motor as an example.

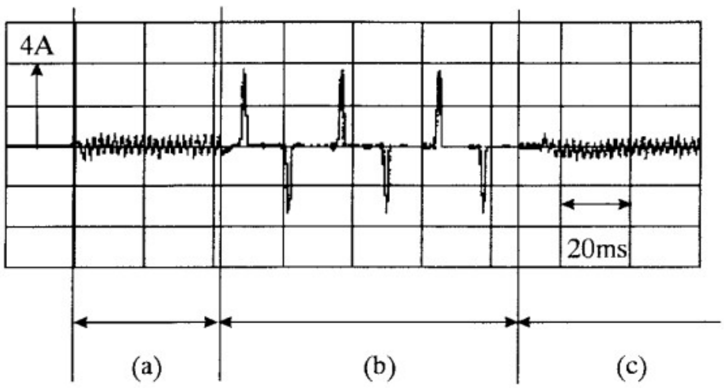

Figure 6.8 : Stages of motor starting rotor position determination [90].

The high-frequency voltages are first injected into the motor windings in the range indicated by (a) region in Figure 6.8. As a result, the rotor initial position is estimated with HFI technique. Then, in the range indicated by (b) region, the HFI is stopped and pilot voltages are applied in the direction of and opposite the rotor q-axis for magnet polarity determination. This process is repeated three times to increase the accuracy of the process. As a result of these processes, the correctness of the initial position of the motor is confirmed and it is ready for operation [90].

6.10 Simulation Results of HFVI Technique

The sensorless low speed control of the PMaSynRM with the HFVI method is simulated in the MATLAB/Simulink platform. The same PMaSynRM in EEMF technique simulations is used and its parameters are given in Table 5.1. Estimated speed and position values are used for the speed control model from start to end of simulation. The initial position of the rotor is selected as 40° electrical angle. It is devoted to settle the speed and position estimation. Besides, SVPWM and three-phase inverter models are integrated into the simulation. Therefore, motor stator voltages are in PWM waveforms. The bandwidths of the speed and current controllers are slightly narrowed so that the influence of estimation vibrations and high-frequency signals to control algorithm is reduced. The simulation model parts are given in following figures. The power stage is given in Figure 6.9. The created HF voltage signals are injected at α&β reference frame in before the entrance SVPWM block.

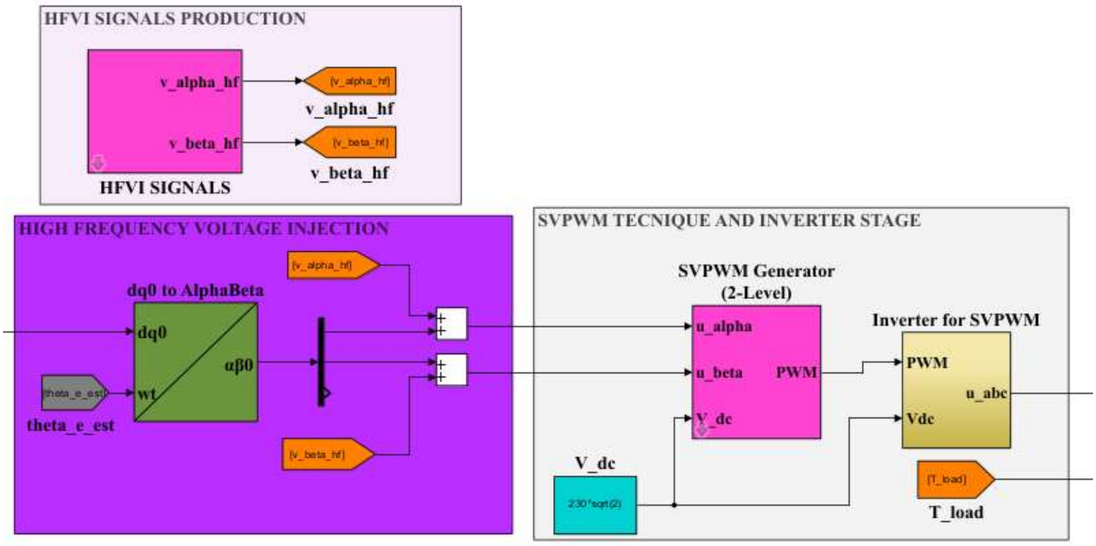

Figure 6.9 : The power stage and injection HF signals.

The speed control stage is given in Figure 6.10. MTPA algorithm is also applied for low speed.

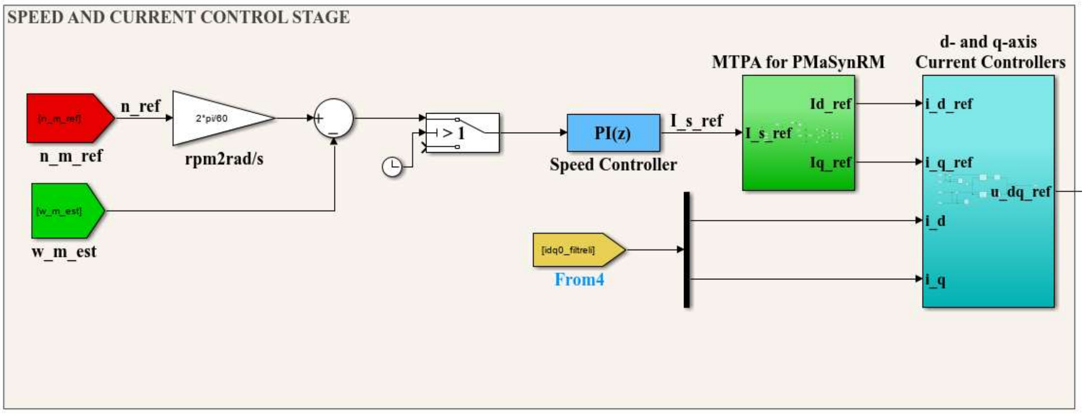

Figure 6.10 : The speed control stage of PMaSynRM.

The motor driven with rated load at two specific speed values, 50 rpm and 300 rpm, to demonstrate the sensorless control performance at low speeds. In addition, the drive cycle is set so that the motor starts with rated load. Besides, the motor start position is selected as non-zero to show that the position estimation is provided for the zero speed, in other words the motor is at still state.

6.10.1 Operating at 50 rpm

The speed estimation tracking and load torque curve are given in Figure 6.11. The motor makes successfully starting to 50 rpm at rated load in 1 seconds.

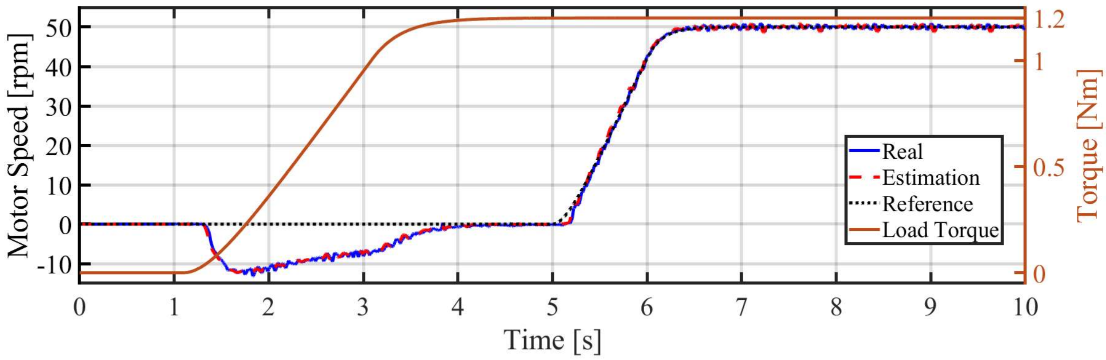

Figure 6.11 : The motor speed estimation starting at rated load to 50 rpm.

The zoomed view of speed tracking is given in Figure 6.12. As can be seen in the figure, the speed fluctuation is under the 2% and it is proper value where the inverter effect is also considered.

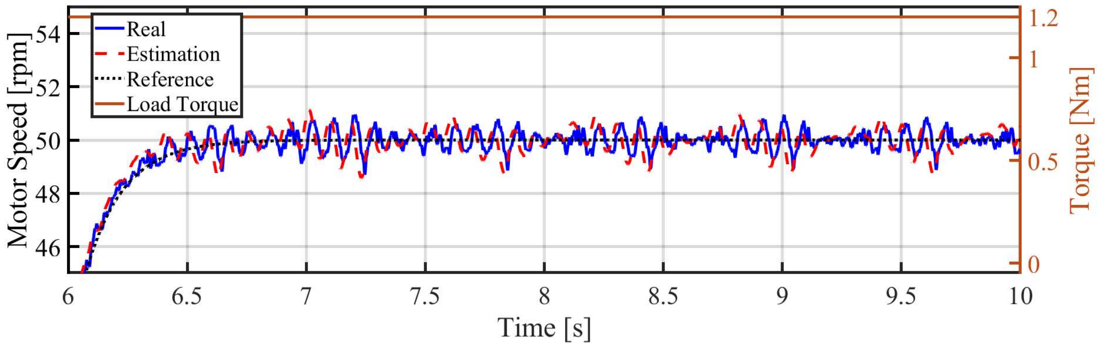

Figure 6.12 : The zoomed view of motor speed estimation at 50 rpm.

The rotor electrical position estimation tracking is given in Figure 6.13. The initial motor position is different from zero but this situation does not cause any error in estimation and the correct estimation is provided. It can be seen that the position estimation continues successfully, although the motor rotates in the opposite direction while loading.

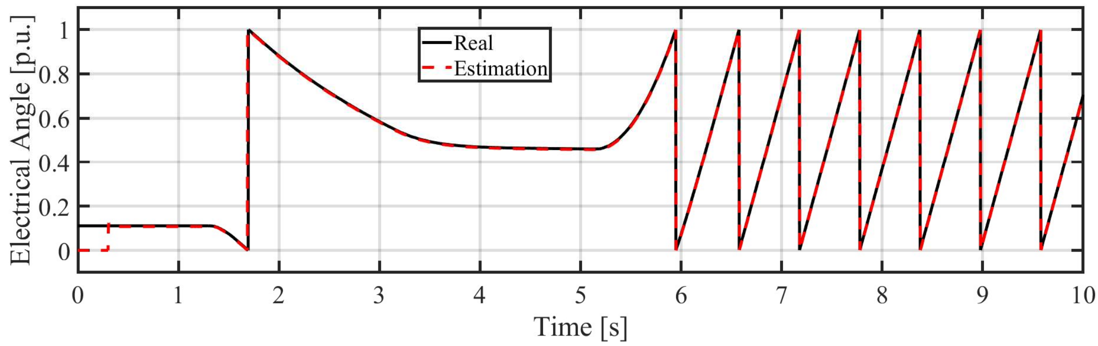

Figure 6.13 : The rotor position estimation tracking at 50 rpm.

The zoomed view of estimation tracking can be seen better in Figure 6.14.

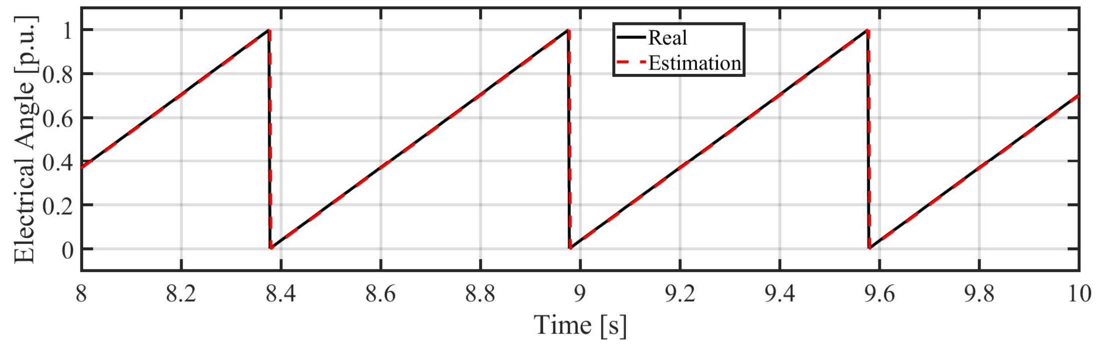

Figure 6.14 : The zoomed view of rotor position estimation tracking at 50 rpm.

The position estimation error is given in Figure 6.15. The average position estimation error is provided to be less than 1.5 electrical degrees.

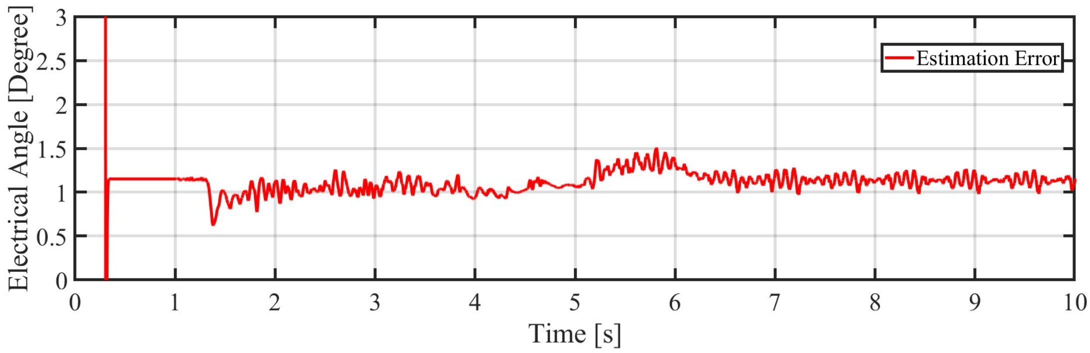

Figure 6.15 : Rotor position estimation error at 50 rpm.

6.10.2 Operating at 300 rpm

The second simulation results are for 300 rpm speed reference. The voltage value is higher according to 50 rpm so that the ripples in the real speed are much lower. The speed estimation tracking and load torque curve are given in Figure 6.16 for 300 rpm. The motor also accelerates to 300 rpm at rated load in 1 seconds successfully.

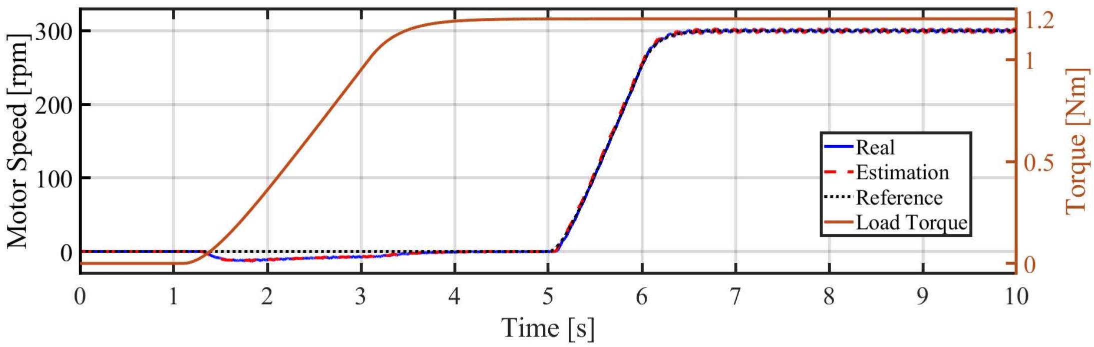

Figure 6.16 : The motor speed estimation starting at rated load to 300 rpm.

The zoomed view of speed tracking is given in Figure 6.17. This time, the speed fluctuation is under the 0.7% and it is better than 50 rpm situation.

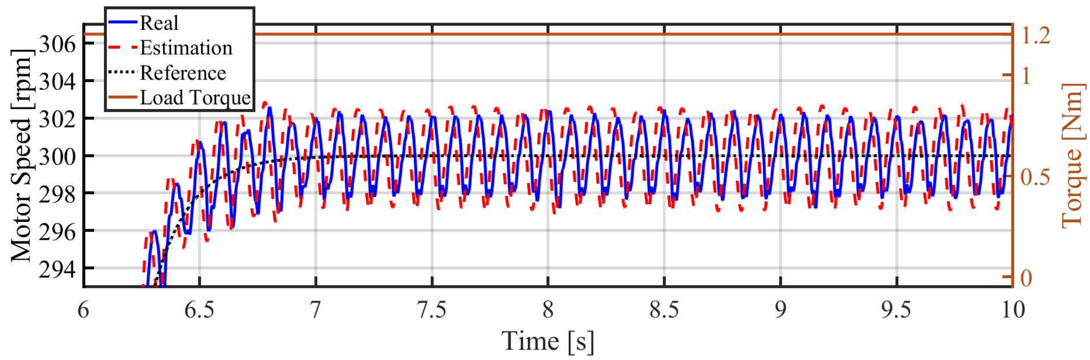

Figure 6.17 : The zoomed view of motor speed estimation at 300 rpm.

The rotor electrical position estimation tracking is given in Figure 6.18. A successful sensorless operation is also achieved at higher speeds.

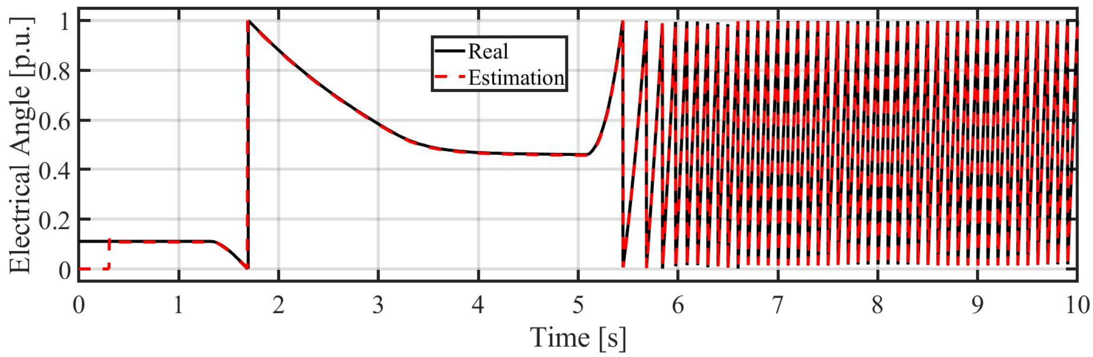

Figure 6.18 : The rotor position estimation tracking at 300 rpm.

A closer view of the motor position estimation tracking is given in Figure 6.19.

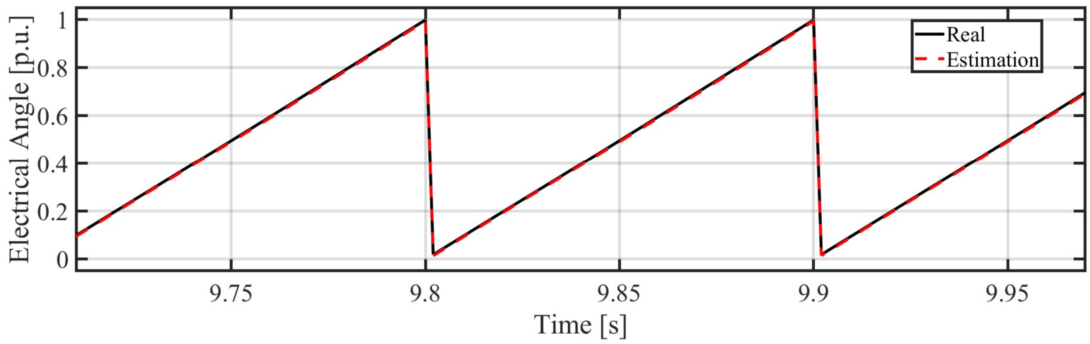

Figure 6.19 : The zoom view of rotor position estimation tracking at 300 rpm.

Although the motor speed increases, it is observed that the angle compensation has been achieved and the average electrical position estimation is lower than 2° as given in Figure 6.20.

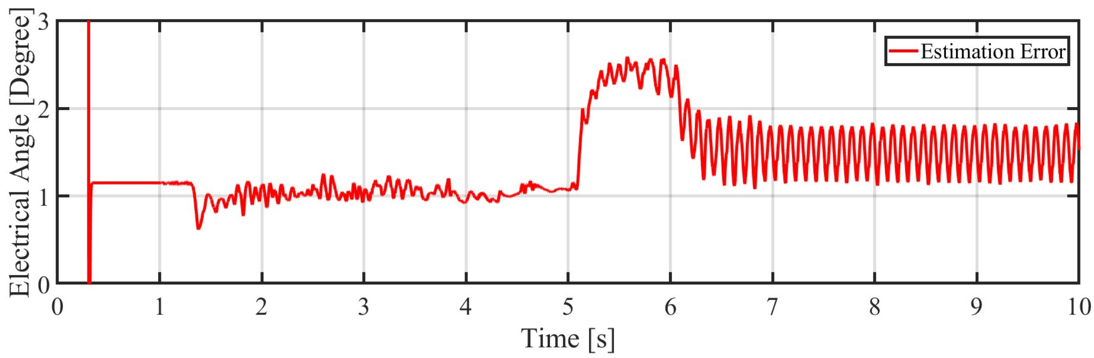

Figure 6.20 : Rotor position estimation error at 300 rpm.

6.10.3 Evaluation of simulation results

As a result of the simulations, the electrical position error remained lower than 2°. An error of 2° corresponds to 0.04% for 50 rpm and 0.56% for 300 rpm in terms of system efficiency and is at reasonable levels. A successful close-loop speed control has been achieved with reasonable changes of speed reference and load torque with using estimated motor speed and position values.

7. EXPERIMENTAL RESULTS

7.1 Test Setup

A test bed is set up for the experiments of project. In the experiments, the motor and load are controlled together to test the simulations. The mechanical side of setup consists of the PMaSynRM, hysteresis brake and torque sensor as shown in Figure 7.1 on the left side. The nameplate values of the PMaSynRM are given in Table 5.1. The MAGTROL AHB-5 hysteresis brake is used for loading and it allows the load torque value to be adjusted independently of the speed. The load torque value is measured on the motor shaft thanks to Kistler torque sensor and its evaluation instrument.

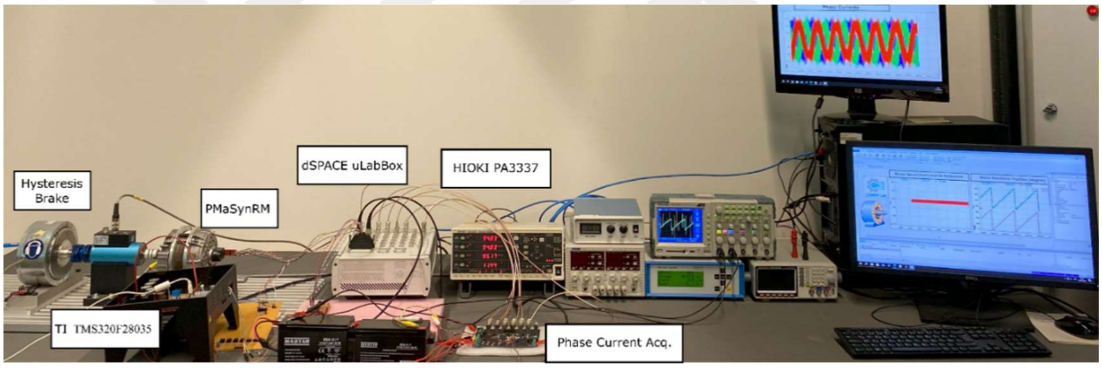

Figure 7.1 : Experiment setup of the study.

The motor driver and power analysers are given in Figure 7.1. The power stage of the setup consists of the TI C2000 motor driver kit which provides the motor control. The HIOKI power analyzer is connected between the driver and the motor. Thus, the three-phase power analysis of the motor is performed. The current regulated power supply located in the middle of the setup is responsible for the torque control of hysteresis brake. In this study, the dSPACE platform is used to the measuring instruments.

A circuit board is designed and manufactured in order to motor phase voltages and currents acquisition. Then, the measured motor phase voltages and currents are monitored. The aims of this setup are getting high resolution data and also phase voltage values which cannot be measured. The designed circuit is providing a galvanic isolation between the motor system and the dSPACE platform for protection. GO 10-

SME/SP3 current sensors based on Hall-effect principle are used to measure the phase currents of motor. The measurement of phase voltages is realized with ACPL-C870 optical isolated voltage sensors.

7.2 The Experimental Results of EEMF Sensorless Control Technique

The experimental test for EEMF technique is performed as sensorless control. The data obtained has noise because of using digital-analog converter (DAC) which is used for monitoring in dSPACE. The speed profile and estimation performance are given in Figure 7.2. The motor is accelerated to 2025 rpm from 300 rpm with ramp speed reference under rated load. It is seen that the estimated speed successfully follows the real speed.

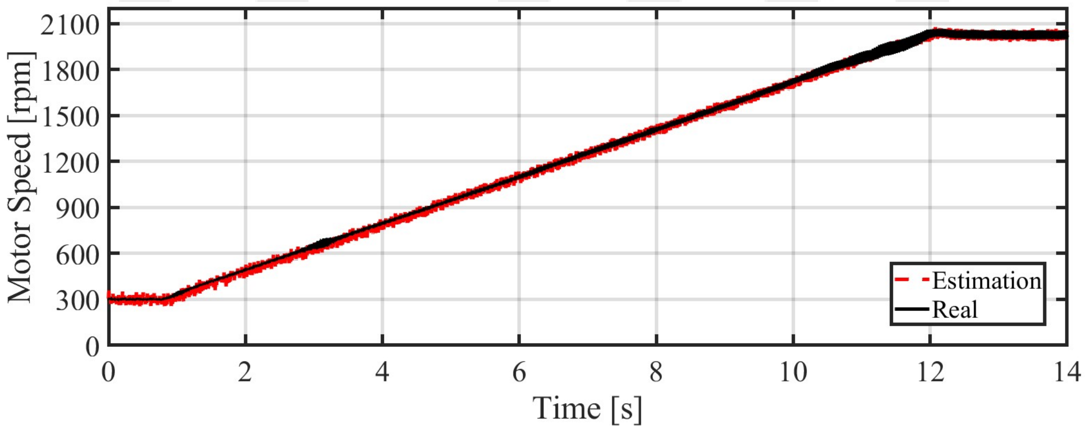

Figure 7.2 : The speed estimation tracking for EEMF technique.

The zoomed view of Figure 7.2 for 300 rpm and 2025 rpm is given in Figures 7.3 and 7.4 respectively. Relative fluctuation is more significant at 300 rpm because of lower EEMF values in lower motor speeds but the controller parameters are adjusted so that real motor speed is not affected by this situation.

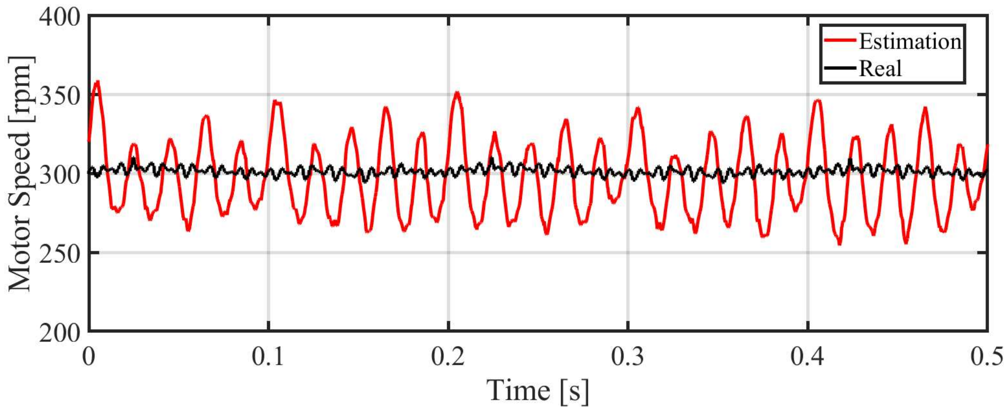

Figure 7.3 : The zoomed view of speed estimation at 300 rpm.

The EEMF technique performance increases with higher speed as seen in Figure 7.4. The estimation ripple is approximately same as the real motor speed.

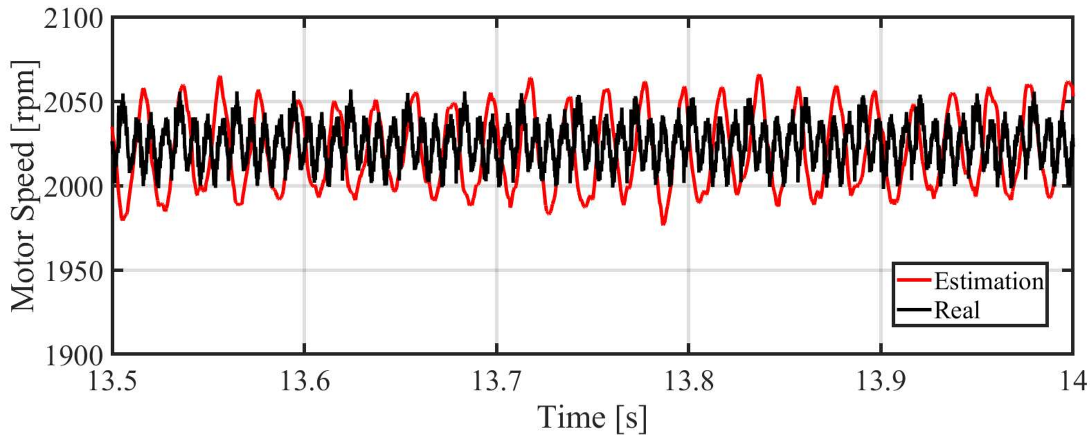

Figure 7.4 : The zoomed view of speed estimation at 2025 rpm.

The tracking performance of position estimation at 300 rpm is given in Figure 7.5. 300 rpm speed value is selected as minimum speed value for EEMF technique as mentioned before. The noise in the estimation is quite a lot as expected for low motor speeds. The position information is obtained with low error when viewed on average.

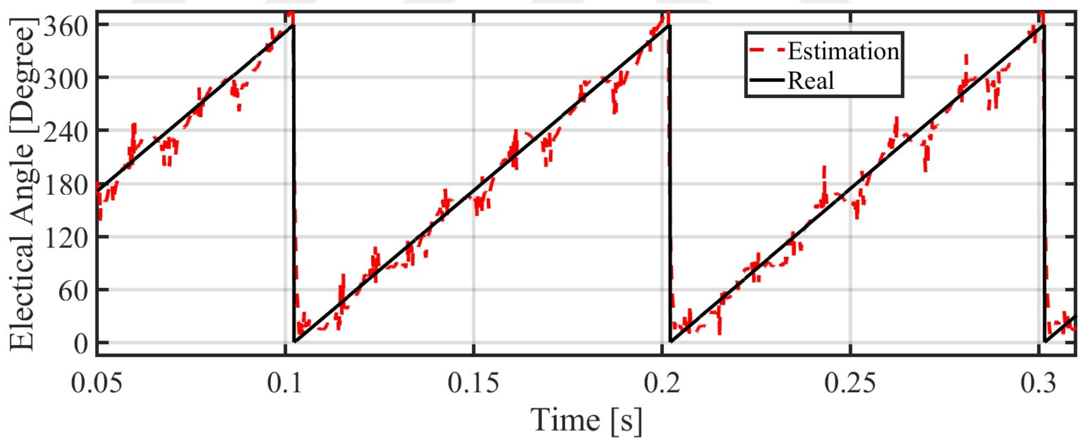

Figure 7.5 : The position tracking performance at 300 rpm.

The tracking performance of position estimation at 2025 rpm is given in Figure 7.6. The rotor position is also estimated successfully for 2025 rpm. Smoother position estimation is provided at higher speeds as described. The drop to zero value remains slow due to the DAC.

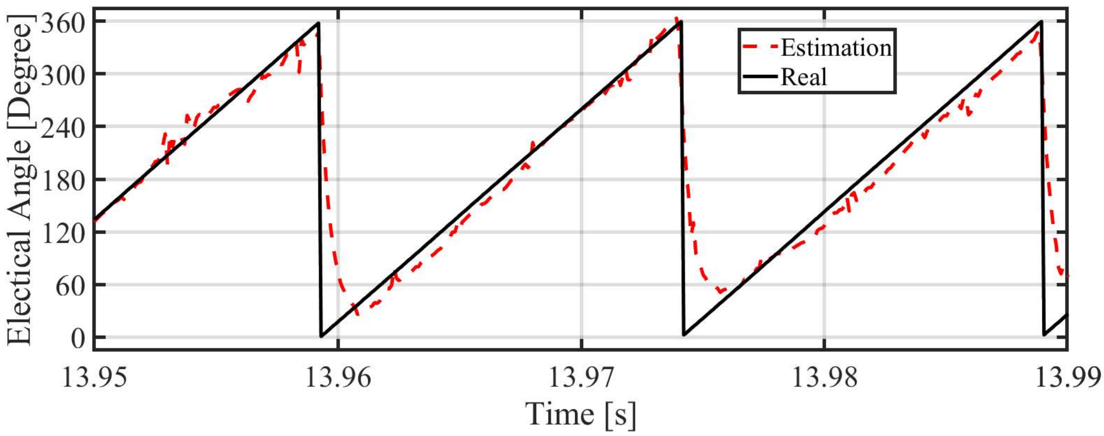

Figure 7.6 : The position tracking performance at 2025 rpm.

7.3 The Experimental Results of HFVI Sensorless Control Technique

The experimental tests are carried out from zero speed to 300 rpm for the situations of no-load and rated load. Electrical magnitudes of the injected signals and filter parameters of demodulation processes are given Table 7.1. The HFI voltage is adjusted to be as low as for minimum effect to present control operation. Besides, the HFI voltage should be as high as to proper measurement. Thus, the HFI voltage amplitude is selected as 16.1 V according to the tests performed. The HFI voltage frequency is determined 500 Hz as one-twentieth of the switching frequency for accurate position determination.

Table 7.1 : HFI experiment values.

Parameter	Value
HFI Voltage Amplitude [V]	16.1
HFI Voltage Frequency [Hz]	500
HF Current Amplitude [mA]	85
Filter passband width [Hz]	330
Notch filter stopband width [Hz]	400

In the first stage of the tests, the lowest speed that the motor can operate at full load is tested. The second test is 100 rpm step response of the motor for two rated load cases. The first one is for starting with dynamic load which has no stall torque. The second one is for starting with stall torque valued of 0.83 pu. The third test is reversing motor speed from -100 rpm to 100 rpm under no load.

As a result of first stage tests, the motor can rotate with the speed of 30 rpm at rated load as seen in Figure 7.7. The 30 rpm speed value corresponds to 1% of base speed. The hysteresis brake torque characteristic has disturbance due to slotting effect. This disturbance is about approximately 30% at low speeds so that the motor speed fluctuation is higher for 30 rpm. Besides, the low inertia of the system also increases the fluctuation. The position estimation is approximately one electrical degree because of the error compensation algorithm. The currents are also affected by the fluctuation.

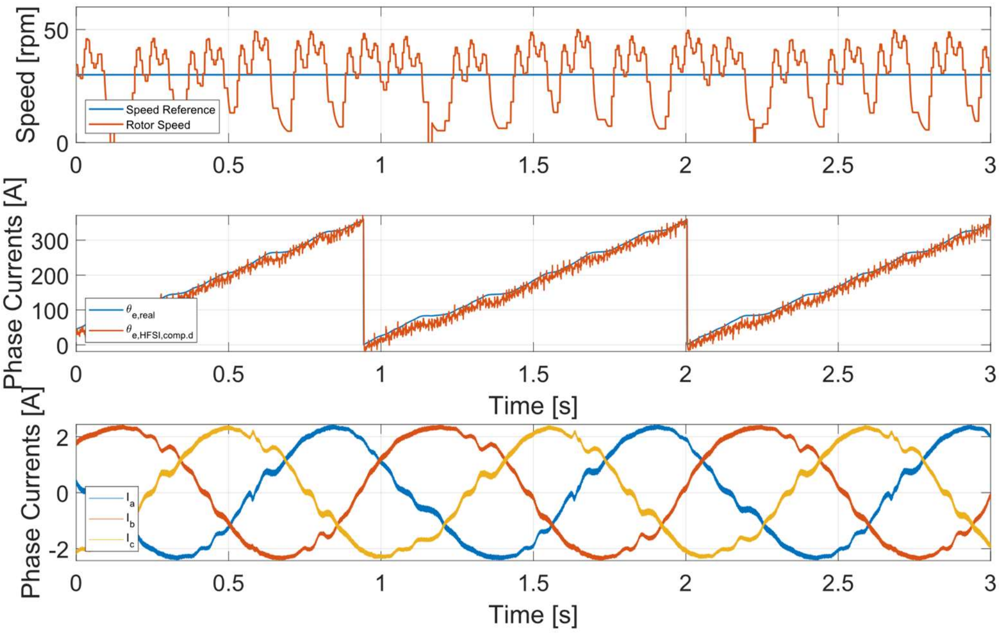

Figure 7.7 : The HFVI operation outputs of the motor at 30 rpm under rated load.

In the second stage of experiments, the step response of the motor is tested. The step response is useful for commenting on the speed control structure because it shows the robustness of the system designed. The step response is carried out under rated load from zero speed to 100 rpm. The first case is for dynamic load which has no stall torque at zero speed as shown in Figure 7.8. Therefore, some dead-time is occurred from step reference time. The motor speed reaches to reference speed about 1 second. The position tracking under speed and current transients are also given in Figure 7.8. The position estimation error is approximately two electrical degrees.

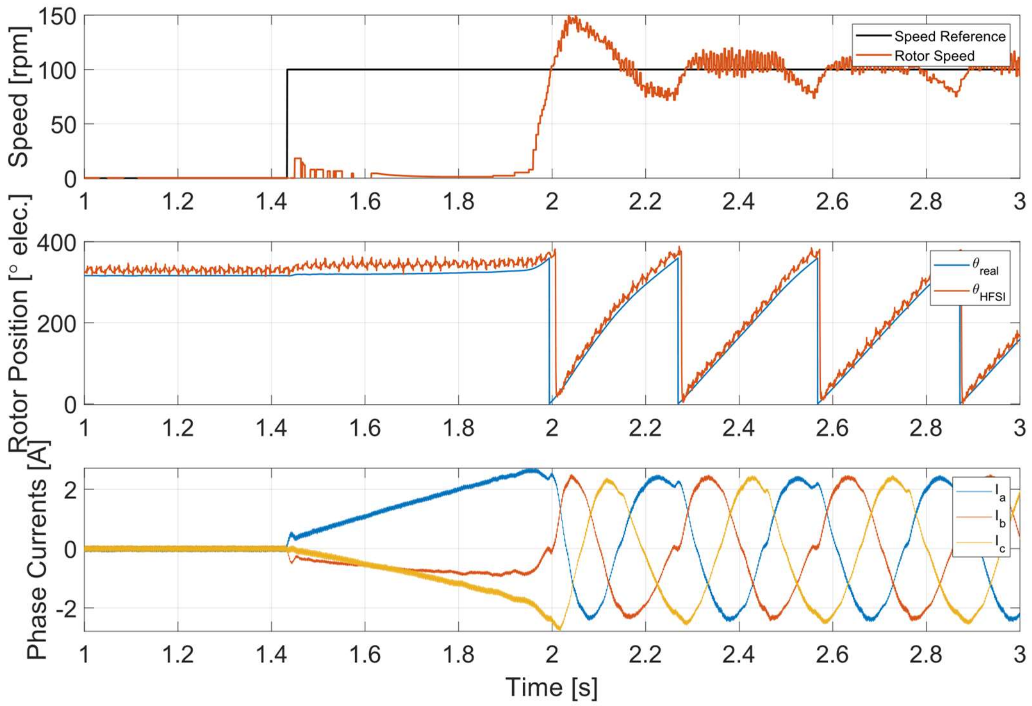

Figure 7.8 : Scenario of step speed reference for without stall torque.

The second case is for step response at starting stall torque situation as shown in Figure 7.9. The stall torque value is 0.83 pu at zero speed. The dead-time is much shorter in this situation.

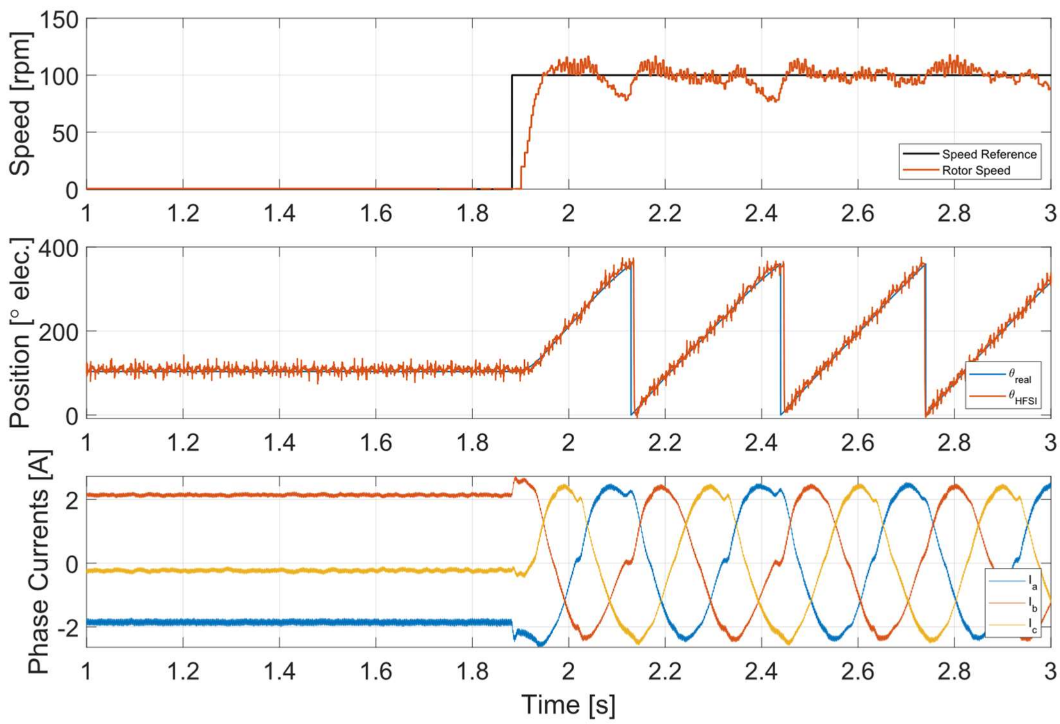

Figure 7.9 : Scenario of step speed reference for with stall torque.

The averaged electrical position error is also two electrical degrees. The steady state operation is better because of better transient state. The phase currents are closer to sinusoidal waveform because they are controlled according to rotor position value.

The HFI technique does not require any extra adjustments for reverse rotation of motor. Hereby, the PMaSynRM is tested to reverse rotation and is passed to straight direction with step speed reference under no-load as seen Figure 7.10. As a result, the motor is operated successfully in both directions without sensors. The position estimation tracking performance is also given in Figure 7.10. There is no tracking loss in position estimation, even instantaneously. The HF currents are better observable because the fundamental stator phase currents are lower under no-load situation.

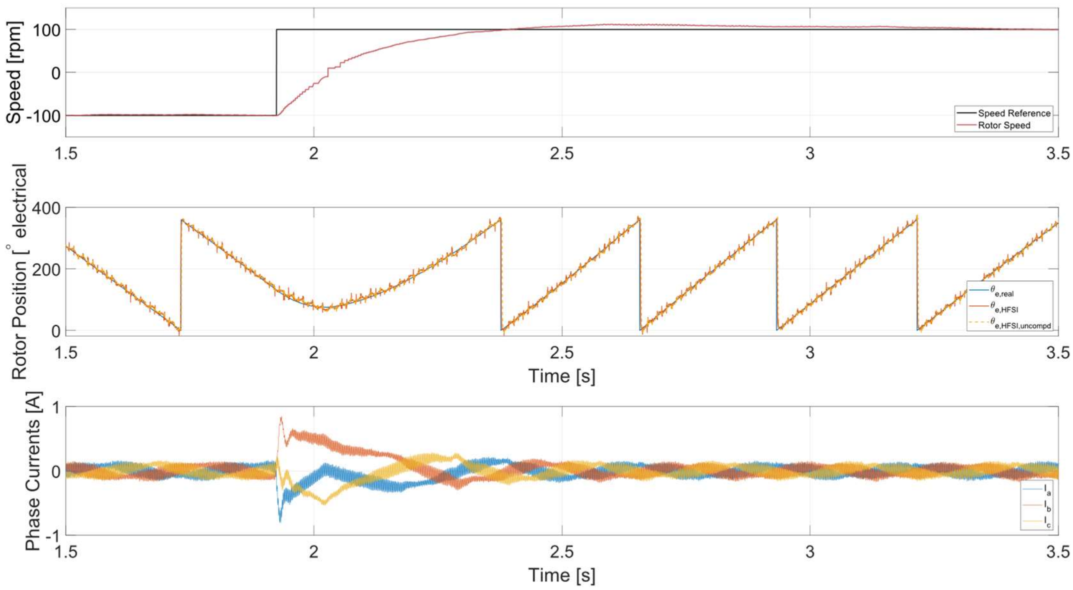

Figure 7.10 : Scenario of reverse rotation -100 rpm to 100 rpm.

The final stage of experiment is passing HFI sensorless operation to EEMF sensorless operation. As mentioned earlier, the passing speed between the sensorless technique is determined as 300 rpm. The switchover operation is given in Figure 7.11. Moreover, it can be seen the EEMF position estimation has more fluctuation than HFI technique. Besides, this fluctuation is much higher at speeds lower than 300 rpm so that the 300 rpm is determined as switchover speed. When the phase currents given in Figure 7.11 are examined, it is seen that the high frequency injection is stopped after the switchover.

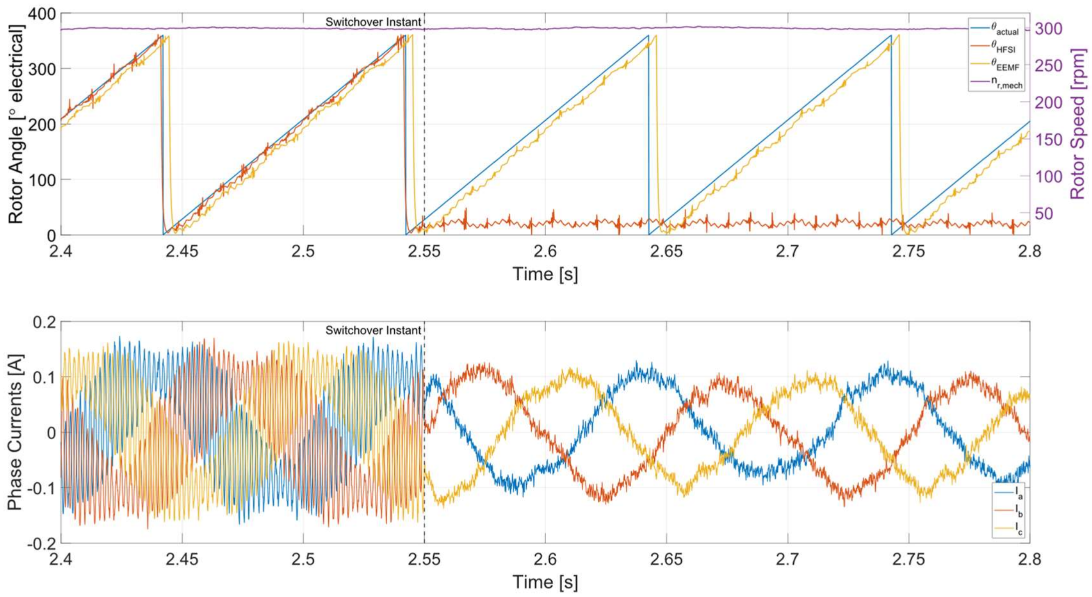

Figure 7.21 : Scenario of passing HFI sensorless operation to EEMF sensorless operation.

7.4 Experimental Results Evaluation

The tests of the sensorless control of PMaSynRM in the simulation environment are carried out in the experimental environment. Thus, the PMaSynRM is successfully driven over entire area of constant torque region. The motor is driven from zero speed to 300 rpm with using HFVI sensorless technique. After the 300 rpm speed value, EEMF technique with SMO is applied to the motor up to rated speed. The electrical position error values are given in Table 7.2 both EEMF and HFVI techniques.

Table 7.2: Averaged electrical position estimation errors for different speeds.

Speed Value [rpm]	**Electrical Position Error [Degree°]**
30 (HFVI)	1.81°
100 (HFVI)	0.99°
300 (HFVI)	1.89°
300 (EEMF)	1.97°
2025 (EEMF)	1.56°

As seen in Table 7.2, staying under 2° position estimation error is also achieved in the experimental environment. Thus, it is ensured that the estimation errors remained at a level that would not be far from the results of the operation with sensor.

8. CONCLUSION AND RECOMMENDATIONS

In this thesis, the history of PMaSynRM is mentioned, its construction and iron resistive equivalent circuits are given. The amplitude and angle of the stator current are controlled together by using FOC in motor control. Thus, the desired motor output can be maximized which is output torque there. The MTPA control, which provides the possible maximum torque at any current value, is shown and information about the SVPWM and inverter structure for the power stage is given. Then the sensorless control of PMaSynRM was discussed. Presented EEMF technique with sliding mode observer, designed for medium to rated speed range. For zero and low speeds, the high-frequency voltage injection technique with PLL structure is explained.

In the first stage, the sensorless control of PMaSynRM is carried out in simulation environment before experimental tests. Firstly, the EEMF model as state-space model is obtained for PMaSynRM in $\alpha\&\beta$ reference frame. The EEMF components which contain position information should be estimated. For this reason, an observer should be used for the estimation. In this study, the Sliding Mode Observer structure is used for its benefits which are quick response, robust structure, and easy implementation. Then, the speed control and EEMF technique are modelled in simulation environment. After all, the sensorless speed control of PMaSynRM is achieved 300 rpm to rated speed of 3000 rpm and also for the rated load. For the rated speed where the efficiency is high and critical, the electrical position estimation error is around 2° and this value is acceptable.

Secondly, the HFI technique is applied for PMaSynRM for sensorless control at zero and low speeds. The rotating voltage injection technique is preferred in this study. Besides, a PLL structure was integrated into the model for improvement in estimations. The HFVI method simulation model also created for PMaSynRM. The PMaSynRM sensorless speed control is actualized from zero speed to 300 rpm which is passing speed value to EEMF technique. The sensorless speed control is also achieved for rated load situations. As a result, the electrical position error is lower than 2° for all speed ranges. 2° error corresponds to 0.04% for 50 rpm and 0.56% for 300 rpm in terms of efficiency and these values are at reasonable levels.

In the next stage, the test system is set up for experiments of sensorless control of PMaSynRM. As a start, the EEMF technique with SMO is tested. Both rotor position and speed are successfully estimated and the motor is driven from 300 rpm to rated speed without sensor. As expected, the noise in estimations increased at low speeds because of lower values of EEMF components. After that, the HFVI technique is tested for low speeds. The motor is driven under rated load at 30 rpm which is 1% of base speed. Then, the 100 rpm step response of motor tested under rated load for with and without stall torque. The tests are successfully carried out without estimation tracking loss. Finally, the motor is tested to be rotated in the opposite direction. As a result, the motor speed is passed in both directions without any adjustments.

The aim of maximum 2° electrical estimation error is achieved both EEMF and HFVI techniques also in experiment environment. Thus, a PMaSynRM designed for washing-machine appliances is successfully driven over entire area of constant torque region without sensor.

For future work, it is suggested to optimize the EEMF technique model by working on different observer techniques such as Luenberger observer. The adaptive observer structure should also tested especially for constant power region. In addition, improvements to be made on the control side will also contribute directly. In HFI technique, obtaining more smoother estimations with different filter techniques of decomposition processes and higher switching frequencies can be applied. It is also suggested to carry out a comprehensive study on pulsating voltage injection for detailed comparison.

REFERENCES

[1] **Tap, A., Xheladini, L., Yilmaz, M., Imeryuz, M., Asan, T., & Ergene, L. T.** (2018). Comprehensive design and analysis of a PMaSynRM for washing machine applications. *IET Electric Power Applications, 12(9)*, 1311–1319.

[2] **Ribeiro, L. A. S., Degner, M. W., Briz, F., & Lorenz, R. D.** (1998). Comparison of carrier signal voltage and current injection for the estimation of flux angle or rotor position. *Conference Record of 1998 IEEE Industry Applications Conference. Thirty-Third IAS Annual Meeting (Cat. No.98CH36242)*, 452–459.

[3] **Akgul, K., Tap, A., Ergenc, A. F., Yilmaz, M., & Ergene, L. T.** (2022). Sensorless Control of PMaSynRM with HFI Method using Modified PLL for Low Speeds. *2022 International Conference on Electrical Machines (ICEM),* 1457–1463.

[4] **Piippo, A., & Luomi, J.** (2005). Adaptive observer combined with HF signal injection for sensorless control of PMSM drives. *IEEE International Conference on Electric Machines and Drives*, 674–681.

[5] **Lagerquist R., Boldea I. & Miller T. J. E.** (1994). Sensorless control of the synchronous reluctance motor. *IEEE Transactions on Industry Applications*, *30*(3), 673–682.

[6] **Consoli A., Cavallaro C., Scarcella G. & Testa A.** (2000). Sensorless torque control of SyncRel motor drives. *IEEE Transactions on Power Electronics*, *15*(1), 28–35.

[7] **Senjyu T., Shingaki T. & Uezato K.** (2001). Sensorless vector control of synchronous reluctance motors with disturbance torque observer. *IEEE Transactions on Industrial Electronics*, *48*(2), 402–407.

[8] **Shinnaka S.** (2002). Mirror-phase characteristics of synchronous reluctance motor and salient-pole orientation methods for sensorless vector controls. *Electrical Engineering in Japan*, *139*(2), 210–218.

[9] **Capecchi E., Guglielmi P., Pastorelli M. & Vagati A.** (2001). Position-sensorless control of the transverse-laminated synchronous reluctance motor. *IEEE Transactions on Industry Applications*, *37*(8), 1768–1776.

[10] **Schroedl M. & Weinmeier P.** (1994). Sensorless control of reluctance machines at arbitrary operating conditions including standstill. *IEEE Transactions on Power Electronics*, *9*(2), 225–231.

[11] **Matsuo T. & Lipo T. A.** (1995). Rotor position detection scheme for synchronous reluctance motor based on current measurements. *IEEE Transactions on Industry Applications*, *31*(4), 860–868.

[12] **Jovanovic M., Betz R. E. & Platt D.** (1998). Sensorless vector controller for a synchronous reluctance motor. *IEEE Transactions on Industry Applications*, *34*(2), 346–354.

[13] **Lin M. T. & Liu T. H.** (2000). Sensorless synchronous reluctance drive with standstill starting. *IEEE Transactions on Aerospace and Electronic Systems*, *36*(4), 1232–1241.

[14] **Jansen P. L. & Lorenz R. D.** (1995). Transducerless position and velocity estimation in induction and salient AC machines. *IEEE Transactions on Industry Applications*, *31*(2), 240–247.

[15] **Ha J., Kang S. J. & Sul S. K.** (1999). Position-controlled synchronous reluctance motor without rotational transducer. *IEEE Transactions on Industry Applications*, *35*(6), 1393–1398.

[16] **Kang, S.-J., Kim, J.-M., & Sui, S.-K.** (1997). Position Sensorless Control of Synchronous Reluctance Motor Using High Frequency Current Injection, *1997 IEEE International Electric Machines and Drives Conference Record*, TB1/3.1-TB1/3.3.

[17] **Consoli A., Russo F., Scarcella G. & Testa A.** (1999). Low- and zero-speed sensorless control of synchronous reluctance motors. *IEEE Transactions on Industry Applications*, *35*(5), 1050–1057.

[18] **Arefeen M. S., Ehsani M. & Lipo T. A.** (1994). Sensorless position measurement in synchronous reluctance motor. *IEEE Transactions on Power Electronics*, *9*(6), 624–630.

[19] **Kreindler L., Testa A. & Lipo T. A.** (1993). Position sensorless synchronous reluctance motor drive using the stator phase voltage third harmonic. *Conference Record of the 1993 IEEE Industry Applications Conference Twenty-Eighth IAS Annual Meeting*, *1*, 679–686.

[20] **Wang, G., Yu, Y., Zhang, G., Wang, B., Yang, M., & Xu, D.** (2018). Sensorless control of motor drives. *Control of Power Electronic Converters and Systems*, 331–369.

[21] **Zhiqian Chen, Tomita, M., Doki, S., & Okuma, S.** (2003). An extended electromotive force model for sensorless control of interior permanent-magnet synchronous motors. *IEEE Transactions on Industrial Electronics*, *50*(2), 288–295.

[22] **Hasegawa, M., & Matsui, K.** (2008). IPMSM Position Sensorless Drives Using Robust Adaptive Observer on Stationary Reference Frame. *IEEJ Transactions on Electrical and Electronic Engineering*, *3*(1), 120–127.

[23] **Atsushi Shinke, Hasegawa, M., & Matsui, K.** (2009). Torque estimation for synchronous reluctance motors using robust flux observer to magnetic saturation. *2009 IEEE International Symposium on Industrial Electronics*, 1569–1574.

[24] **Zhang, Z., & Zhou, L.** (2016). Sensorless Control of a Ferrite PM Assisted-Synchronous Reluctance Machines by Using Sliding Mode Observer and High Frequency Signal Injection. *Elektronika Ir Elektrotechnika*, *22*(4).

[25] **Jingbo Liu, Nondahl, T. A., Schmidt, P. B., Royak, S., & Harbaugh, M.** (2011). Rotor Position Estimation for Synchronous Machines Based on Equivalent EMF. *IEEE Transactions on Industry Applications*, *47*(3), 1310–1318.

[26] **Scalcon, F. P., Volpato, C. J., Lazzari, T., Gabbi, T. S., Vieira, R. P., & Grundling, H. A.** (2019). Sensorless Control of a SynRM Drive Based on a Luenberger Observer with an Extended EMF Model. *IECON 2019 - 45th Annual Conference of the IEEE Industrial Electronics Society*, 1333–1338.

[27] **Ichikawa, S., Tomita, M., Doki, S., & Okuma, S.** (2007). Sensorless control of synchronous reluctance motors based on extended electromotive force model and inductance measurement. *Electrical Engineering in Japan*, *160*(4), 70–80.

[28] **Cernat, M., Comnac, V., Cotorogea, M., Korondi, P., Ryvkin, S., & Cernat, R.-M.** (2000). Sliding mode control of interior permanent magnet synchronous motors. *7th IEEE International Power Electronics Congress. Technical Proceedings. CIEP 2000,* 48–53.

[29] **Utkin, V. I., Guldner, J., & Shi, J.** (1999). *Sliding mode control in Electro-Mechanical Systems.* New York: CRC Press.

[30] **Zhang Yan, & Utkin, V. I.** (2002). Sliding mode observers for electric machines-an overview. *IEEE 2002 28th Annual Conference of the Industrial Electronics Society IECON 02*, *3*, 1842–1847.

[31] **Foo, G., & Rahman, M. F.** (2010). Sensorless sliding-mode MTPA control of an IPM synchronous motor drive using a sliding-mode observer and HF Signal Injection. *IEEE Transactions on Industrial Electronics*, *57*(4), 1270–1278.

[32] **Foo, G., & Rahman, M. F.** (2010). Direct torque control of an IPM-synchronous motor drive at very low speed using a sliding-mode stator flux observer. *IEEE Transactions on Power Electronics*, *25*(4), 933–942.

[33] **Zhuang Xu, & Rahman, M. F.** (2007). An adaptive sliding stator flux observer for a direct-torque-controlled IPM Synchronous Motor Drive. *IEEE Transactions on Industrial Electronics*, *54*(5), 2398–2406.

[34] **Zhuang Xu, & Rahman, M. F.** (2007). Direct torque and flux regulation of an IPM synchronous motor drive using variable structure control approach. *IEEE Transactions on Power Electronics*, *22*(6), 2487–2498.

[35] **Pippo, A., Hinkkanen, M. & Luomi, J.** (2008). Analysis of adaptive observer for sensorless control of IPMSM. *31st Annual Conference of IEEE Industrial Electronics Society, IECON 2005, 55*(2), 570–576.

[36] **Wang, Y., Wu, J., Guo, Z., Xie, C., Liu, J., & Jin, X.** (2022). Flux-weakening fuzzy adaptive ST-SMO sensorless control algorithm for PMSM in EV. *The Journal of Supercomputing*, *78*(8), 10930–10949.

[37] **Tian-Hua Liu, & Ming-Tsan Lin.** (2000). Sensorless synchronous reluctance drive with standstill starting. *IEEE Transactions on Aerospace and Electronic Systems*, *36*(4), 1232–1241.

[38] **Zhang, Z., Hu, C., Zhang, Y., & Shen, W.** (2019). Research on High Frequency Voltage Injection Method for PMSM. *2019 14th IEEE Conference on Industrial Electronics and Applications (ICIEA)*, 266–269.

[39] **De Kock, H. W., Kamper, M. J., & Kennel, R. M.** (2009). Anisotropy Comparison of Reluctance and PM Synchronous Machines for Position Sensorless Control Using HF Carrier Injection. *IEEE Transactions on Power Electronics*, *24*(8), 1905–1913.

[40] **Ji-Hoon Jang, Sul, S.-K., Jung-Ik Ha, Ide, K., & Sawamura, M.** (2003). Sensorless drive of surface-mounted permanent-magnet motor by high-frequency signal injection based on magnetic saliency. *IEEE Transactions on Industry Applications*, *39*(4), 1031–1039.

[41] **Messali, A.** (2019). Contribution to Rotor Position and Speed Estimation for Synchronous Machine Drive Using High Frequency Voltage Injection : Application to EV/HEV Powertrains.

[42] **Raca, D., Garcia, P., Reigosa, D. Dí., Briz, F., & Lorenz, R. D.** (2010). Carrier-Signal Selection for Sensorless Control of PM Synchronous Machines at Zero and Very Low Speeds. *IEEE Transactions on Industry Applications*, *46*(1), 167–178.

[43] **Toliyat, H. A. & Kliman, G. B.** (2004). *Handbook of Electric Motors*. Marcel Dekker.

[44] **Blondel, A.** (1913). Synchronous Motors and Converters; Theory and Methods of Calculation and Testing.

[45] **Boucherot, P.** (n.d.) Moteur a courant alternatif simple synchrone sans excitation continue. *L'Industrie Electrique*, *10*, 541–542

[46] **Kostko, J. K.** (1923). Polyphase reaction synchronous motors. *Journal of the American Institute of Electrical Engineers*, *42*(11), 1162–1168.

[47] **Doherty, R. E., Nickle, C. A., & Associate, A. I. E. E.** (1926). Synchronous Machines I-An Extension of Blondel's Two-Reaction Theory. *Transactions of the American Institute of Electrical Engineers, 45,* 912–947.

[48] **Honsinger, V. B.** (1971). The Inductances Ld and Lq of Reluctance Machines. *IEEE Transactions on Power Apparatus and Systems, 1,* 298–304.

[49] **Pellegrino, G., Bianchi, N., Cupertino, F., Jahns, T. M., & Soong, W.** (2016). *The rediscovery of synchronous reluctance and ferrite permanent magnet motors tutorial course notes.* Cham: Springer International Publishing.

[50] **Douglas, J. F. H.** (1956). The Theory of Anisotropic Field Structures in Synchronous Machines [includes discussion], *Transactions of the American Institute of Electrical Engineers. Part III: Power Apparatus and Systems*, *75*(3), 84–86.

[51] **Cruickshank, A. J. O., Eng, C., Anderson, A. F., & Menzies, R. W.** (1971). Theory and performance of reluctance motors with axially laminated anisotropic rotors. *Proceedings of the Institution of Electrical Engineers*, *1*(7), 887–894.

[52] **Lawrenson, P. J. and Gupta, S. K.** (1967). Developments in the performance and theory of segmental-rotor reluctance motors. *IEE Proceedings*, *114*, 645–653.

[53] **Miller, T. J. E., Hutton, A., Cossar, C., & Staton, D. A.** (1991). Design of a Synchronous Reluctance Motor Drive. In *IEEE Transactions On Industry Applications, 27*(4).

[54] **Moghaddam, R. R.** (2011). *Synchronous reluctance machine (SynRM) in variable speed drives (VSD) applications.* (Doctoral thesis). KTH Royal Institute of Technology, Electrical Engineering, STOCKHOLM.

[55] **Kumar, D.** (2016). *Review of Synchronous Reluctance Motors*.

[56] **Fratta, A., & Vagati, A.** (1992). A reluctance motor drive for high dynamic performance application. *IEEE Transactions on Industry Applications*, *28*(4), 873–879.

[57] **Xu, L., Xu, X., Lipo, T. A., & Novotny, D. W.** (1991). Vector Control of a Synchronous Reluctance Motor Including Saturation and Iron Loss. *IEEE transactions on industry applications, 21*(5).

[58] **Url-1** <*https://library.e.abb.com/public/5dda0668955440c0a4483de90c7cdf7a/ ABB_fact_file_DOLynRM_LOWRES.pdf*>; date retrieved 29.06.2021.

[59] **Ozcelik, N. G., Dogru, U. E., Imeryuz, M. & Ergene, L. T.** (2019). Synchronous Reluctance Motor vs. Induction Motor at Low-Power Industrial Applications: Design and Comparison. *Energies*, *12*, 2190.

[60] **Kazakbaev, V. M., Prakht, V. A., & Dmitrievskii, V. A.** (2017). A comparative performance analysis of induction and synchronous reluctant motors in an adjustable-speed electric drive. *Russian Electrical Engineering*, *88*(4), 233–238.

[61] **Url-2** <*https://www.coursehero.com/file/68970577/Infineon-motorcontrol-handbook-AdditionalTechnicalInformation-v01-00-ENpdf* >; date retrieved 21.07.2021.

[62] **Degano, M., Paolo Colombo, C., Profssa Luisa Rossetto, C., Alberto Tessarolo, C., & Nicola Bianchi, C.** (2015). Analysis, Design and Optimization of Innovative Electrical Machines Using Analytical and Finite Element Analysis Methods.

[63] **Heidari, H., Rassõlkin, A., Kallaste, A., Vaimann, T., Andriushchenko, E., Belahcen, A., & Lukichev, D. V.** (2021). A review of synchronous reluctance motor-drive advancements. *Sustainability, 13*(2), 1–37.

[64] **Sriprang, S., Nahid-Mobarakeh, B., Takorabet, N., Pierfederici, S., Kumam, P., Bizon, N., Taghavi, N., Vahedi, A., Mungporn, P., & Thounthong, P.** (2020). Design and control of permanent magnet assisted synchronous reluctance motor with copper loss minimization using MTPA. *Journal of Electrical Engineering*, *71*(1), 11–19.

[65] **De Pancorbo, S. M., Ugalde, G., Poza, J., & Egea, A.** (2015). Comparative study between induction motor and Synchronous Reluctance Motor for electrical railway traction applications. *2015 5th International Electric Drives Production Conference (EDPC)*, 1–5.

[66] **Vartanian, R. & Toliyat, H. A.** (2009). Design and comparison of an optimized permanent magnet-assisted synchronous reluctance motor (PMa-SynRM) with an induction motor with identical NEMA Frame stators. *2009 IEEE Electric Ship Technologies Symposium.*

[67] **Lucian, B. I. T.** (2020). *Reluctance electric machines: Design and control.* Boca Raton: CRC Press.

[68] **Babitsky, D. Y., Toporkov, D. M., & Banshchikov, N. A.** (2018). Synchronous reluctance motor for electric mine locomotive. *IOP Conference Series: Earth and Environmental Science*, *194*(5).

[69] **Estima, J. & Cardoso, A. J. M.** (2018). Super Premium Synchronous Reluctance Motor Evaluation. *8th International Conference on Energy Efficiency in Motor Driven Systems*.

[70] **Moghaddam, R. R.** (2011). *Synchronous Reluctance Machine (SynRM) Design.* (Master thesis). KTH Royal Institute of Technology, Electrical Engineering, STOCKHOLM.

[71] **Pyrhönen, J., Hrabovcová, V., & Semken, R. S.** (2016). *Electrical machine drives control: An introduction.* John Wiley & Sons, Inc.

[72] **Oliveira, A., Cavaleiro, D., Branco, R., Hadla, H., & Cruz, S.** (2015). An encoderless high-performance synchronous reluctance motor drive. *2015 IEEE International Conference on Industrial Technology (ICIT).*

[73] **Chiang, H.-K., Chen, C.-A., Lin, B.-R., & Hsu, K.-S.** (2006). Current sensorless integral variable structure controller of synchronous reluctance motor. *2006 CES/IEEE 5th International Power Electronics and Motion Control Conference,* 1–5.

[74] **Briggner, V., Skolan, K., Elektroteknik, F., & Datavetenskap, O.** (2018). *Design and comparison of PMaSynRM versus PMSM for pumping applications*. (Master thesis). KTH Royal Institute of Technology, Electrical Engineering, STOCKHOLM.

[75] **Yesilbag, E., & Ergene, L. T.** (2014). Field oriented control of permanent magnet synchronous motors used in washers. *2014 16th International Power Electronics and Motion Control Conference and Exposition*, 1259–1264.

[76] **Vartanian, R.** (2014). *Permanent Magnet Assisted Synchronous Reluctance Machine (PMa-SynRM) Design and Performance Analysis for Fan and Pump Applications*. (Doctoral thesis). Texas A&M University, Electrical Engineering, COLLEGE STATION.

[77] **Uçak, O., & Yilmaz, S.** (2015). Implementation of Space Vector PWM In FOC of a Servo Motor Drive. *ELECO 2015 9th International Conference on Electrical and Electronics Engineering.*

[78] **Akgul, K., Ergenc, A. F., Yılmaz M. & Ergene, L. T.** (2022). Dead-Time Analysis in Three-Phase Two-Level Inverters using the SVPWM Technique. *2022 4th Global Power, Energy and Communication Conference (GPECOM),* 210–215.

[79] **Bin Ibrahim, Z., Liton Hossain, M., Bin Bugis, I., Munaji Nik Mahadi, N., Shukri Abu Hasim, A., & Professor, A.** (2014). Simulation Investigation of SPWM, THIPWM and SVPWM Techniques for Three Phase Voltage Source Inverter. *International Journal of Power Electronics and Drive System (IJPEDS)*, *4*(2), 223–232.

[80] **Bin Ibrahim, Z., Hossain, Md. L., Bin Bugis, I., Nik Mahadi, N. M., & Abu Hasim, A. S.** (2014). Simulation investigation of SPWM, THIPWM and SVPWM techniques for three phase voltage source inverter. *International Journal of Power Electronics and Drive Systems (IJPEDS),* 4(2).

[81] **Sevilmis, F., & Karaca, H.** (2015). Simulation and analysis of SVPWM based VSI for wind energy systems. *Proceedings of the 2014 6th International Conference on Electronics, Computers and Artificial Intelligence, ECAI 2014*, 73–78.

[82] **Faleh Alskran B, by A., & Professor Behrooz Mirafzal, M.** (2011). *Dynamic Modeling and analysis of the three-phase voltage source inverter under stand-alone and grid-tied modes.* (thesis), Electrical Engineering, Kansas State University, Manhattan, Kan.

[83] **Tap, A., Akgul, K., Ergenc, A. F., Yilmaz, M., & Ergene, L. T.** (2021). A Comparison of Sensorless MTPA and Quasi-MPF Control for VSD-PMaSynRM. *IECON 2021 – 47th Annual Conference of the IEEE Industrial Electronics Society*, 1–6.

[84] **Kondo, S., Tomita, M., Hasegawa, M., Doki, S., & Kato, S.** (2015). Position Sensorless Control of SynRM at Low Speeds by Estimating High-Frequency Extended EMF Using Disturbance Observer. *2015 IEEE 2nd International Future Energy Electronics Conference (IFEEC),* 1–5.

[85] **Yi, B., Vukosavić, S. N., Ortega, R., Stanković, A. M., & Zhang, W.** (2020). A new signal injection-based method for estimation of position in interior permanent magnet synchronous motors. *IET Power Electronics, 13*(9), 1865–1874.

[86] **Brandstetter, P., & Krecek, T.** (2013). Sensorless control of permanent magnet synchronous motor using voltage signal injection. *Electronics and Electrical Engineering, 19*(6).

[87] **Agrawal, J., & Bodkhe, S.** (2015). Low speed sensorless control of PMSM drive using high frequency signal injection. *2015 Annual IEEE India Conference (INDICON).*

[88] **Medjmadj, S., Diallo, D., Mostefai, M., Delpha, C., & Arias, A.** (2015). PMSM drive position estimation: Contribution to the high-frequency injection voltage selection issue. *IEEE Transactions on Energy Conversion*, *30*(1), 349–358.

[89] **Chen, Y., Wang, L., & Kong, L.** (2008). Research of Position Sensorless Control of PMSM Based on High Frequency Signal Injection. *2008 International Conference on Electrical Machines and Systems,* 3973–3977.

[90] **Aihara, T., Toba, A., Yanase, T., Mashimo, A., & Endo, K.** (1999). Sensorless Torque Control of Salient-Pole Synchronous Motor at Zero-Speed Operation. In *IEEE Transactions on Power Electronics, 14*(1), 202–208.

[91] **Holtz, J.** (2008). Acquisition of position error and magnet polarity for sensorless control of PM synchronous machines. *IEEE Transactions on Industry Applications*, *44*(4), 1172–1180.

[92] **Trancho, E., Ibarra, E., Arias, A., Kortabarria, I., & Prieto, P.** (2017). A practical approach to HFI based Sensorless Control of PM-assisted Synchronous Reluctance Machines applied to EVs and HEVs, *IECON 2017 - 43rd Annual Conference of the IEEE Industrial Electronics Society,* 1735–1740.

[93] **Manzolini, V., Morandin, M., & Bolognani, S.** (2016). D-axis polarity detection for IPM synchronous motor drives by high frequency voltage injection. *IECON 2016 - 42nd Annual Conference of the IEEE Industrial Electronics Society,* 4325–4330.

[94] **Hu, J., Liu, J., & Xu, L.** (2008). Eddy current effects on rotor position estimation and magnetic pole identification of PMSM at zero and low speeds. *IEEE Transactions on Power Electronics*, *23*(5), 2565–2575.

[95] **Wu, X., Wang, H., Huang, S., Huang, K., & Wang, L.** (2015). Sensorless speed control with initial rotor position estimation for surface mounted permanent magnet synchronous motor drive in electric vehicles. *Energies*, *8*(10), 11030–11046.

CURRICULUM VITAE

Name Surname : Kadir Akgül

EDUCATION :

- **B.Sc.** : 2020, Istanbul Technical University, Faculty of Electrical and Electronic, Electrical Engineering.
- **B.Sc.** : 2020, Istanbul Technical University, Faculty of Electrical and Electronic, Control and Automation Engineering.

PROFESSIONAL EXPERIENCE AND REWARDS:

- 2021 – present, Research Assistant at Istanbul Technical University

PUBLICATIONS, PRESENTATIONS AND PATENTS ON THE THESIS:

- Tap, A., **Akgul, K.,** Ergenc, A. F., Yilmaz, M., & Ergene, L. T. (2021). A Comparison of Sensorless MTPA and Quasi-MPF Control for VSD-PMaSynRM. *IECON 2021 – 47th Annual Conference of the IEEE Industrial Electronics Society*, 1–6.
- **Akgul, K.,** Ergenc, A. F., Yılmaz M. & Ergene, L. T. (2022). Dead-Time Analysis in Three-Phase Two-Level Inverters using the SVPWM Technique. *2022 4th Global Power, Energy and Communication Conference (GPECOM)*, 210–215.
- **Akgul, K.,** Tap, A., Ergenc, A. F., Yilmaz, M., & Ergene, L. T. (2022). Sensorless Control of PMaSynRM with HFI Method using Modified PLL for Low Speeds. *2022 International Conference on Electrical Machines (ICEM)*, 1457–1463.